

TECHNISCHE UNIVERSITÄT MÜNCHEN

Lehrstuhl für Biologische Bildgebung

**Accurate quantification and detailed bio-distribution with planar multispectral
fluorescence imaging**

Athanasios Sarantopoulos

Vollständiger Abdruck der von der Fakultät für Elektrotechnik und Informationstechnik der Technischen Universität München zur Erlangung des akademischen Grades eines

Doktor-Ingenieurs

genehmigten Dissertation.

Vorsitzender: Univ.-Prof. Dr.-Ing. habil., Dr.h.c. A. W. Koch

Prüfer der Dissertation:

1. Univ.-Prof. V. Ntziachristos, Ph.D.
2. Univ.-Prof. Dr. rer. nat. G. Multhoff

Die Dissertation wurde am 04.10.2011 bei der Technischen Universität München eingereicht und durch die Fakultät für Elektrotechnik und Informationstechnik am 17.04.2012 angenommen.

**Accurate quantification and detailed bio-distribution
with planar multispectral fluorescence imaging**

Athanasios Sarantopoulos

2011

Accurate quantification and detailed bio-distribution with planar multispectral fluorescence imaging

Athanasios Sarantopoulos

2011

A dissertation for the degree of the Doctor of Engineering (Dr-Ing).

Presented to the Faculty of Electrical Engineering of the Technical
University of Munich

Prof. Vasilis Ntziachristos

Supervisor of dissertation

ABSTRACT

Multispectral optical imaging promises to become the next widespread imaging modality in medical diagnostics. The main advantages of this technology are its non invasive and non harmful nature, its excellent correlation with the human visual perception, the very high resolution and magnification and the high diagnostic accuracy provided when used in combination with disease-specific molecular fluorescent markers.

Planar fluorescence imaging is probably the most straightforward way to perform molecular imaging; however it is not the easiest. Several issues arise in cases where accurate quantification and detailed bio-distribution are important. It is critical to point out these limitations and suggest ways to make planar fluorescence imaging more precise and accurate, especially since last years have seen a revitalized interest of its use, both in preclinical animal research and, more importantly, in image-guided surgery of humans in combination with tumor-targeted fluorophores.

In this work, we identified the limited ability of planar fluorescence imaging to capture and quantify detailed depth information, when used to study the bio-distribution of fluorescent probes in excised organs or tissue samples of small animals. The absence of truly volumetric data throughout the organs imaged, the loss of accurate information as to the organs surrounding tissues, and the possible omission of unknown areas of fluorochrome accumulation are the most major problems of the technology. In response, we developed a novel implementation and supporting algorithms and software for the *ex-vivo* three-dimensional investigation of fluorescence bio-distribution in small animals. The scope of this work ranged from understanding the fundamental physical principles and modeling the light-matter interaction to engineering optical systems and evaluating them for studies of mouse disease models. Using multimodal approaches consisting of multiple standard molecular, chemical and analytical techniques (histology, MRI, PET, CT, optical and optoacoustic tomography), we tested the performance of the implementation and

illustrated its abilities on preclinical research. Our multispectral imaging approach not only provided novel insights in aspects of tumor development, disease staging and metastasis that were until now impossible to visualize, it also presented a multispectral high-resolution 3D systematic framework for the development, in-depth study and visualization of the bio-distribution of novel fluorescent agents in healthy and diseased organisms.

Furthermore, we identified, studied thoroughly and present herein a detailed insight in the primary reason for quantification errors in planar fluorescence imaging: the effect of underlying tissue optical properties (absorption and scattering). Experiments ranging from phantoms, animal studies *ex-vivo* and *in-vivo* as well as human clinical data allowed us to underline the major limitations of the technology and propose an image-processing method (FASSED) that retrieves in real-time the quantification ability of planar fluorescence systems by successfully decomposing the effects of the two tissue constituents.

Finally, we developed a clinical-grade multispectral fluorescence imaging system and carried out a series of first-ever human clinical trials that demonstrated the advantages of fluorescence intra-operative imaging for the identification of sentinel lymph nodes and lymphatic mapping and revealed the aptness and potential of optical molecular intra-operative cancer detection. We proved that the combination of planar multispectral imaging with tumor-specific fluorophores can shift the paradigm of surgical oncologic practice, offering the unique and unprecedented opportunity to intra-operatively detect and quantify tumor growth and spread and ultimately guide the surgeon to achieve a curative resection.

ABSTRACT IN GERMAN

In dieser Arbeit wird eine neuartige Methode beschrieben, welche die Modellierung von Licht- Gewebe Interaktionen mit adaequate Hardware Implementierung (optisches System) kombiniert. Diese hochauflösende, dreidimensionale ex-vivo Bildgebungsmethode erlaubt die Untersuchung der Biodistribution von molekularen Proben an Kleintieren.

Weiterhin wurde eine neuartiges planares multispektrales Bildgebungssystem eingefuehrt, welches durch die Korrektur von optischen Gewebshomogenitaeten eine akkurate Quantifizierung von fluoreszierenden Substanzen in Echtzeit ermoeeglicht. Dieser Ansatz wurde fuer praeklinische und klinische in vivo Studien benutzt. Das System wurde zudem erstmals an Menschen in einer klinische Studien angewendet und zeigt eindrucksvoll die Vorteile auf, die optische molekulare Bildgebung im Hinblick auf Lymphknotenidentifizierung und Krebszellendetektion aufweist.

ACKNOWLEDGEMENTS

First and most of all, I would like to thank the supervisor of my work, Prof. Vasilis Ntziachristos, or as he usually prefers Vasilis. I am grateful and respectful to him not only for the amount of knowledge and experience in the biomedical field he shared with me, the helpful and fruitful conversations and comments throughout my work, the scientific curiosity he developed in me, but more importantly for giving me the chance to work in such a scientifically stimulating environment, believing in me, supporting me and for being there for me, whenever I needed him. Vasilis always managed to approach correctly even the most rigorous problems with clarity and precision and to guide me away from 'scientific' pitfalls. His judgement in choosing the right questions and his genuine curiosity in pursuing them has been a constant driving force in my research. Therefore, during this period, I hope to have 'absorbed' some of his virtues and qualities apart from the common 'tricks of trade'.

I also benefited greatly from my interactions with all the members of the IBMI research institute and all the external collaborators. I need to specially mention Dr. George Themelis for the countless discussions on optics, fluorescence and multispectral imaging. His shared knowledge helped me broaden my scientific horizons and experiences to parts also outside of my research objects. I am also grateful to Dr. Nikolaos Deliolanis for providing me his massive scientific background and experience in optics whenever I needed. Also I would like to express my gratitude to my colleagues Claudi, Saskia, Adrian and Angeliqne who experienced with me the everyday ups and downs of research, have tolerated me throughout this long time and engaged with me into all kinds of scientific discussions. Of course, my gratitude goes without saying also for the 'unknown heros' of scientific research, the technical personnel of all kinds, for their unconditioned assistance, help and continuous support.

I am fortunate to have worked with many great collaborators, but among them all I wish to specially thank Prof. Go van Dam, Dr. Wendy Kelder, Niels Harlaar and all the team in UMCG, Groningen for taking care of my 'introduction' to the clinical environment and for all their efforts in our common projects.

Finally I would like to thank my friends and parents for their love and support throughout this long journey.

Table of contents:

- 1 Introduction**
- 2 Development of a novel multispectral cryoslicing modality for the ex vivo imaging of fluorescent probes bio-distribution.**
 - 2.1 Introduction
 - 2.2 Literature Review
 - 2.3 Development of a novel multispectral cryoslicing imaging modality
 - 2.4 Studies
 - 2.4.1 Bio-distribution in healthy mice
 - 2.4.2 Bio-distribution in a xenograft mouse model
 - 2.4.3 Bio-distribution in genetically engineered pancreatic cancer models
 - 2.4.4 Bio-distribution using spectral fitting
 - 2.5 Validation of other tomographic modalities
- 3 Development of an experimental clinical-grade real-time intra-operative imaging system for surgical guidance**
 - 3.1 Introduction
 - 3.2 Development of a clinical-grade real-time intra-operative multispectral imaging system for surgical guidance
 - 3.3 Animal Studies
 - 3.3.1 Tumor margins identification
 - 3.3.2 Clinical imaging setup evaluation
 - 3.4 Clinical Imaging Protocols
 - 3.5 Clinical Studies

	3.5.1	Intra-operative imaging for sentinel lymph node (SLN) detection (breast, cervix and vulva cancer)
	3.5.2	2 Intra-operative imaging for tumor detection in ovarian cancer
	3.6	Discussion and Conclusion
4		Theoretical background of photon propagation
5		Monte Carlo simulation method for ex-vivo fluorescence imaging
	5.1	Problem
	5.2	Method description
6		Fluorescence absorption and scattering enhanced decomposition
	6.1	Problem
	6.2	Literature Review
	6.3	Method description
7		Application of developed algorithms in ex-vivo fluorescence images
	7.1	Application examples of Monte Carlo based out-of-plane fluorescence correction
	7.2	Application examples of the FASED fluorescence correction algorithm in ex-vivo images
8		Application of developed algorithms in in-vivo fluorescence images
9		Conclusion and future outlook
		References

List of figures and tables:

Figure 2-1: Bio-distribution in excised organs with planar fluorescence imaging.

Figure 2-2: Schematic of the cryoslicing imaging setup.

Figure 2-3: The User Interface of the cryoslicing modality

Figure 2-4: Mouse sample embedded in OCT-India ink mixture.

Figure 2-5: Cross-sections at the mouth level of a healthy mouse.

Figure 2-6: Cross-sections at the nasal cavity level of a healthy mouse.

Figure 2-7: Cross-sections at the lung level of a healthy mouse.

Figure 2-8: Cross-sections at the kidneys level of a healthy mouse.

Figure 2-9: A sagittal section reconstructed from the original data.

Figure 2-10: Whole mouse body reconstruction and 3D fluorescence bio-distribution of a probe-injected healthy mouse.

Figure 2-11: Whole mouse body reconstruction and 3D fluorescence bio-distribution of a PBS-injected healthy mouse.

Figure 2-12: Volumetrically analyzed bio-distribution of accumulated fluorophores in individual organs per voxel.

Figure 2-13: Automatic mouse body and internal structure segmentations.

Figure 2-14: Cross-sections at two different levels of the thorax of a tumor bearing xenograft mouse.

Figure 2-15: 3D maximum intensity projections showing the bio-distribution of IntegriSense and AngioSense in a tumor bearing xenograft mouse.

Figure 2-16: Western Blot and immunohistochemical analysis in the multiple endogenous mouse models.

Figure 2-17: Representative planar whole body color, normalized fluorescence and original fluorescence images of wildtype, CK and CKP animal models.

Figure 2-18. Relative fluorescence tumor to background (TBR) ratios for CK and CKP animals.

Figure 2-19. Representative cross-sectional cryoslicer images: color, original fluorescence, normalized fluorescence and corresponding T2w-MRI images for CK and CKP animals.

Figure 2-20. Volumetric rendering of the three-dimensional fluorescence distributions for CK and CKP animals.

Figure 2-21: EGFP excitation and emission spectra.

Figure 2-22: Cross-sectional cryoslicer images at the kidneys, spleen and intestine level.

Figure 2-23: Cross-sectional cryoslicer image at the mouse brain and eyes level.

Figure 2-24. 3D reconstructions of the abdominal area using fluorescence and spectrally unmixed data.

Figure 2-25: Cryoslicing images used for the fluorescence molecular tomography (FMT/XCT) validation.

Figure 2-26: Cryoslicing images provide anatomical validation for multispectral optoacoustic tomography (MSOT).

Figure 3-1: Schematic and photograph of the developed intra-operative imaging setup.

Figure 3-2: Picture of the developed multispectral intra-operative system during measurements inside the operating room.

Figure 3-3: In-vivo and ex-vivo intra-operative fluorescence and bioluminescence imaging in a xenograft breast cancer mouse model.

Figure 3-4: H&E staining and planar fluorescence image of a cryosection of residual breast tumor.

Figure 3-5: Different frames during the tumor resection surgery in a tumor bearing xenograft mouse model.

Figure 3-6: Different frames during the tumor resection surgery in an ovarian cancer mouse model.

Figure 3-7: The sentinel lymph node (SLN) theory.

Figure 3-8: Color, fluorescence and overlay images during the SLN detection in breast, cervix and vulva cancer patients.

Figure 3-9: Lymph drainage schematic of the cervix uteri.

Figure 3-10: In-vivo detection of ovarian cancer with a targeted fluorescent probe.

Figure 3-11: Ex-vivo fluorescence imaging of excised tumor spot from the peritoneal surface.

Figure 3-12: In-vivo detection of ovarian cancer deposits with a targeted fluorescent probe.

Figure 3-13: Fluorescence microscopy and histology from three different ovarian tumor samples.

Figure 5-1: Monte Carlo simulation of a travelled photon path.

Figure 5-2: Schematic of the out-of-plane fluorescence contribution.

Figure 5-3: Flowchart of the Monte Carlo correction algorithm.

Figure 6-1: Schematic/flowchart of the FASED image processing algorithm.

Figure 7-1: Out-of-plane fluorescence correction example on a mouse thorax cross-section.

Figure 7-2: An intensity plot through the corrected area.

Figure 7-3: Monte Carlo correction example in a reconstructed sagittal slice of a xenograft mouse.

Figure 7-4: Phantom A AngioSense fluorescence intensities before and after the FASED correction.

Figure 7-5: Phantom B AngioSense fluorescence intensities before and after the FASED correction.

Figure 7-6: Phantom A FITC fluorescence intensities before and after the FASED correction.

Figure 7-7: Phantom B FITC fluorescence intensities before and after the FASED correction.

Figure 7-8: Color and fluorescence images of tissue-mimicking phantoms of variable blood and scatterer concentrations.

Figure 7-9: Color, fluorescence intensity and FASED images at a cross-section of a mouse bearing different xenograft tumors (4T1 and CT26).

Figure 7-10: Color, fluorescence intensity and FASED images at two different cross-section of a mouse bearing different xenograft tumors (4T1 and CT26).

Figure 8-1: In-vivo color, fluorescence intensity and FASED images of a colon cancer bearing xenograft mouse.

Figure 8-2: In-vivo color, fluorescence intensity and FASED images of a colon cancer bearing xenograft mouse.

Figure 8-3: In-vivo color, fluorescence intensity and FASED images of a mouse implanted with two different xenograft tumors on the mammary fat pad.

Figure 8-4: Clinical application of the FASED algorithm.

Table 7-1: Compositional properties of tissue-mimicking phantoms and average fluorescence intensity of each sample.

Chapter 1: Introduction

The most common medical examination worldwide is the visual inspection of tissue. Medical practitioners derive diagnostic information using their vision based only on the patient's color appearance and the existence of local discolorations.

However, scientists were always investigating methods to enhance human vision in order to provide a more accurate diagnosis of disease. The first applications of fluorescence imaging in clinical practice date back to the 1940s with the use of porphyrins (Auler and Banzer 1942) and fluorescein (Moore 1947) for tumor identification, while auto-fluorescence has been considered already since the 1920s for its diagnostic value (Policard 1924). The term 'fluorescence' refers to the property of certain molecules to absorb light of a certain wavelength and subsequently emit it at a longer wavelength. The last 30 years, especially since the emergence of molecular imaging, have seen a considerable development of fluorescent agents for *in-vivo* labeling of cellular and sub-cellular structures and functions. As a result, antibodies, peptides, peptidomimetics and nanoparticles have

been introduced and widely disseminated in preclinical biomedical research as targeting moieties for various diseases. These novel targeting strategies are increasingly employed to understand (among others) the complexity, diversity and *in-vivo* behavior of many diseases like cancer, cardiovascular disease and neurodegeneration.

In parallel, the increasing availability in preclinical research of small animals that serve as models of human-like disease offered increasing insights into the various functional characteristics of the human body and presented new possibilities for early disease diagnosis and therapy monitoring. A particular reason for that are the late advances in genomics and the advent of genetically modified animal species for laboratory purpose. The ability to use adequate animal models in combination with fluorescent probes that tag molecular events for *in-vivo* imaging provided biologists with a multitude of new insights in the development, functional characteristics of living organisms and the interrogation of complex biological processes.

The introduction of novel targeting moieties and the more detailed understanding of various diseases have, lately, revitalized the interest in clinical fluorescence imaging for improving various optical-based clinical procedures such as surgery and endoscopy. Planar fluorescence is considered probably 'the' molecular imaging modality that can be most easily translated into clinical practice thanks to its attractive characteristics: the use of non-ionizing radiation, the real-time video rate operation, the portability and the fact that it relates directly to human vision. It is a promising and straightforward technique that could assist health practitioners with everyday treatment and provide diagnostic information when used in combination with disease-specific fluorescent agents. Planar multispectral fluorescence imaging systems consist of a spatially distributed excitation source that illuminates the tissue of interest, whereas an optical setup with a charge coupled device (CCD camera) obtains two-dimensional reflectance and/or fluorescence images of the excited surface. Novel studies using fluorescent contrast agents are presented herein and showcase the technology's performance and potential for *in-vivo* applications. Application-specific multispectral fluorescence imaging systems could substantially improve oncological

surgical procedures by accurately defining tumor margins, by mapping sentinel lymph nodes, or by defining anatomical features invisible to the human eye during the surgical intervention.

Although planar fluorescence in-vivo imaging is an easy to use and straightforward imaging technique, at the same time, it has several limitations that need to be underlined. In this work we study two of the most major limitations of planar fluorescence imaging: the inability to provide detailed depth information when used for *ex-vivo* animal imaging applications and the limited quantification in *in-vivo* applications due to the spatial variations of tissue optical properties. In such tissues with inhomogeneous optical properties, the recorded fluorescence intensity does not exhibit a linear dependence on fluorophore concentration; it rather reflects a distorted relation between the fluorophore concentration and the local absorbers and scatterers concentration. Thus, variations of tissue optical properties can modify the captured fluorescence image, even if the fluorochrome concentration remains unaltered. For this purpose we developed and present herein a novel modality for *ex-vivo* three-dimensional multispectral fluorescence imaging that could substitute planar *ex-vivo* imaging in small animal research. Furthermore, we introduce a novel processing method for real-time fluorescence correction that retrieves the true fluorophore concentration in tissues regardless of the underlying optical properties.

This work is structured as follows. Chapter 2 presents the details of the developed multispectral cryoslicing imaging system that captures *ex-vivo* high resolution 3D fluorescence bio-distribution volumes in small animals. We review the related literature on invasive *ex-vivo* imaging modalities and present a set of studies showcasing the imaging performance of this novel implementation and its potential applications. Healthy, tumor xenograft and genetically engineered mouse models are studied for the fluorescence bio-distribution of multiple fluorescent agents. Chapter 3 focuses on the development of a clinical-grade real-time multispectral imaging system for intra-operative use. The novel studies of clinical fluorescence imaging presented include the real-time mapping of the

lymphatic system and the identification of the sentinel lymph nodes in breast and gynecologic cancer patients. Furthermore, we introduce the first-in-human study of fluorescence imaging coupled with a tumor-specific contrast agent in ovarian cancer patients to showcase the ability of our modality and of the combined approach to accurately identify tumor borders in image-guided surgery. Chapter 4 provides a short theoretical background on analytical descriptions and modeling of photon propagation in tissue. Chapter 5 describes a novel algorithm to correct for out-of-plane fluorescence signals in block face imaging modalities based on Monte Carlo simulations of photon propagation. Chapter 6 introduces a novel method that decomposes the effect of tissue absorption and scattering in planar fluorescence images and retrieves accurate information of fluorescent agents' bio-distribution in tissues. Chapters 7 and 8 present the results of the aforementioned algorithms in *ex-vivo* and *in-vivo* imaging applications ranging from tissue mimicking phantoms to clinical images. Finally, Chapter 9 summarizes the work presented herein and discusses future improvements for the developed technology and methods.

Chapter 2: Development of a novel multispectral cryoslicing modality for the *ex vivo* imaging of fluorescent probes bio-distribution.

2.1 Introduction

Fluorescent molecules with the ability to tag molecular processes in tissues *in-vivo* have emerged in the past decade (Weissleder and Ntziachristos 2003; Eisenberg, Adusumilli et al. 2006; Weissleder and Pittet 2008; Shu, Royant et al. 2009; Olson, Jiang et al. 2010) to facilitate the understanding of various biological processes and diseases. Various classes of probes are currently employed to study carcinogenesis, cardiovascular diseases, inflammation, or neuro-degeneration, to name a few indications (Weissleder and Ntziachristos 2003; Ntziachristos, Ripoll et al. 2005; Zong, Espinosa et al. 2005; Deguchi, Aikawa et al. 2006; Jaffer, Libby et al. 2007). In response, several approaches have been developed for *in-vivo* imaging of fluorescent agents, including epi-illumination planar imaging (Weissleder, Tung et al. 1999; Yang, Baranov et al. 2000; Gao, Cui et al. 2004; Ntziachristos, Turner et al. 2005; Bogaards, Sterenborg et al. 2007; Hillman and Moore

2007), fluorescence tomography (Ntziachristos, Tung et al. 2002; Sharpe, Ahlgren et al. 2002 ; Hillman and Burgess 2009), or multispectral optoacoustic tomography (Razansky, Vinegoni et al. 2007; Li, Oh et al. 2008; Razansky, Distel et al. 2009). These novel imaging methods attain strong potential for the dynamic investigation of fluorochrome function in tissues and are increasingly employed in biomedical research. Typically, the confirmation of *in-vivo* fluorescence imaging findings and overall the study of fluorochrome bio-distribution inside living organisms is based on fluorescence imaging of either an exposed surgical cavity (*in situ* imaging) or alternatively of excised organs, typically placed under a fluorescence camera (Deguchi, Aikawa et al. 2006; Tanaka, Choi et al. 2006) (Fig. 2-1). This approach comes with several limitations, most notably the absence of truly volumetric data throughout the

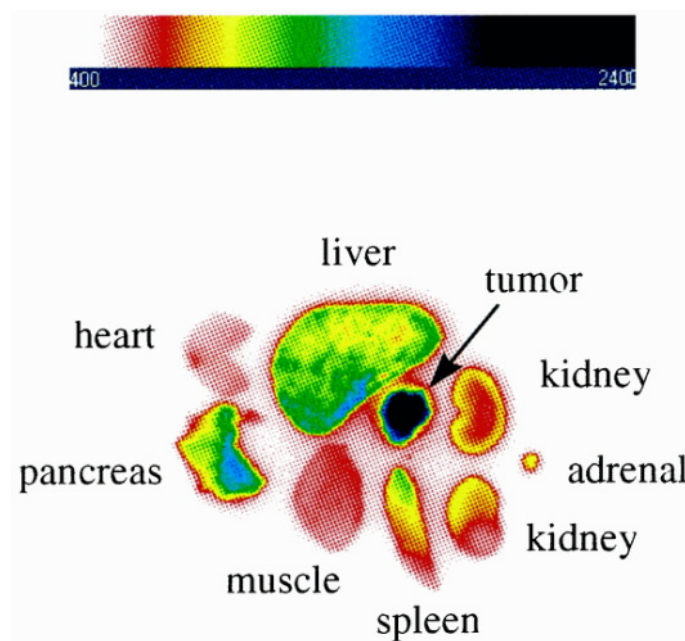


Figure 2-1: Typically the study of the fluorescent agents bio-distribution in small animals is based on planar fluorescence imaging of excised organs and tissues. Image taken from (Bugaj, Achilefu et al. 2001).

organs imaged, the loss of accurate information as to the organs normal position inside the animal and its surrounding tissues, and as a result also to the possible omission of unknown areas of fluorochrome accumulation. A particular limitation is the inability of epi-

illumination fluorescence imaging to image deep inside tissues (more than a few millimeters below the tissue surface depending on the fluorophore's excitation and emission wavelengths and the optical properties of the tissue) since the excitation and emission light undergo strong attenuation as they propagate through tissue, due to absorption and scattering. Therefore, epi-illumination imaging of excised tissues only reveals the fluorochrome's bio-distribution at the tissue surface and fails to probe deeper within animals or whole organs placed under the camera. In addition, tomographic methods developed for three-dimensional imaging of whole animals may still lack the resolution or the sensitivity of superficial planar techniques. As a result, little is known as to the exact whole-body bio-distribution of many fluorescently labeled agents used for exploratory purposes.

For this reason, we developed and present herein a novel multispectral imaging system to study the bio-distribution of fluorescent probes for *ex-vivo* small animal imaging. The system is based on a cryomicrotome unit retrofitted with a multiple-wavelength capturing camera and in contrast to previous approaches (Ewald, McBride et al. 2002; Weninger and Mohun 2002; Rosenthal, Mangal et al. 2004; Wilson, Roy et al. 2008; Steyer, Roy et al. 2009), it can resolve multiple fluorochromes in the same measurement for comparison studies. Using spectral differentiation, we are able not only to identify the particulars of bio-distribution but also the relative accumulation of multiple fluorescent bio-markers. In its current implementation, the multispectral cryoslicing platform developed can image up to five different probes simultaneously. Using a Monte Carlo method to simulate photon pathways (light distribution) inside tissue (described in detail in Chapter 4), out-of-focus light contributions are also improved.

The remainder of the Chapter is structured as follows. In section 2.2 we review the literature around *ex-vivo* 3D block face imaging modalities for small animal imaging and in section 2.3 we describe in detail our implementation. Subsequently three animal studies of fluorescence bio-distribution are presented to showcase the performance of the implementation and reveal its most prominent fields of application. Section 2.4.1

investigates how different fluorescent contrast agents distribute inside healthy animals. In parallel, the auto-fluorescence present inside the mouse body is also measured and reported in relation to the signals obtained from the fluorescent probes. Section 2.4.2 studies the different patterns of fluorophore targeting and bio-distribution in a xenograft mouse model using two near-infrared probes, whereas section 2.4.3 presents a multi-modal study of the avb3-integrin expression and its targeting characteristics in various stages of pancreatic cancer development in endogenous mouse models. Section 2.4.4 presents preliminary results that showcase the ability of spectral unmixing techniques to decompose low fluorescence signals based on their spectral signature. Finally section 2.5 discusses the use of multispectral cryoslicing technology for the validation of other non-invasive tomographic modalities and shortly presents a few examples. It should be noted that all images shown in this chapter are post-processed with the Monte Carlo simulation method described in Chapter 4.

2.2 Literature Review

The first systematic approaches in *ex-vivo* high-resolution three-dimensional epillumination (photographic) imaging of small animals started at least in the late 1990s (Cannestra, Santori et al. 1997), mainly facilitated by the advent of digital photography. The most prominent implementations of the time were developed in order to populate digital animal atlases with color or monochrome reflectance images and/or to create the first multi-modality atlases of animal functional and anatomical characteristics. Therein three-dimensional information from non-invasive tomographic modalities such as magnetic resonance imaging (MRI), x-ray computed tomography (CT) or positron emission tomography (PET)) was merged with series of reflectance block images and (more rarely) immunohistochemical analysis. Among them, a unique approach was proposed by Dogdas (Dogdas, Stout et al. 2007), where a multimodal mouse atlas was created from PET, CT and color reflectance images. Apart from the evident educational purpose, the scientists went

one step further and segmented all inner organs of the animal, appointed different optical properties at each organ and utilized the mouse atlas as a simulation framework for bioluminescence tomography.

In the 2000s, the boost of developmental biology and the wide dissemination of transgenic animal models further advanced the field, with groups being primarily interested in describing in detail and categorizing transgenic animals (mainly embryos) based on their anatomical morphology and specific gene expressions. Like their predecessors these novel imaging systems were developed around optical microscopes and the animal blocks fixated with paraffin, resins or other polymers.

Of all the above technologies, probably the most prominent shortcoming is the limited spectral range of the developed optical systems and the time needed for a full animal scanning. In most of the cases only one image was captured for every cross-section, usually only tissue auto-fluorescence, while color reflectance images, otherwise a valuable descriptive tool, are usually omitted. In their attempt to achieve very detailed images many groups capture multiple images in a mosaic pattern rather than single images for every block section. While this approach makes a more effective use of the hardware it nevertheless has a considerable consequence on the imaging procedure which becomes lengthy and has the effect of a limited animal throughput.

Our approach is unique as its aim was to create a modality that images *ex-vivo* whole small animal (predominantly mouse) three dimensional volumes with high spatial and spectral resolution in a quick and efficient way using low cost components. Built around a commercially available cryomicrotome, our modular experimental imaging setup can be easily integrated in common laboratory practice as it can be coupled to virtually any microtome device and achieve high dissemination in biomedical research, changing thus the paradigm of studying the performance of multiple fluorescently labeled molecules simultaneously and with great detail.

2.3 Development of a novel multispectral cryoslicing imaging modality

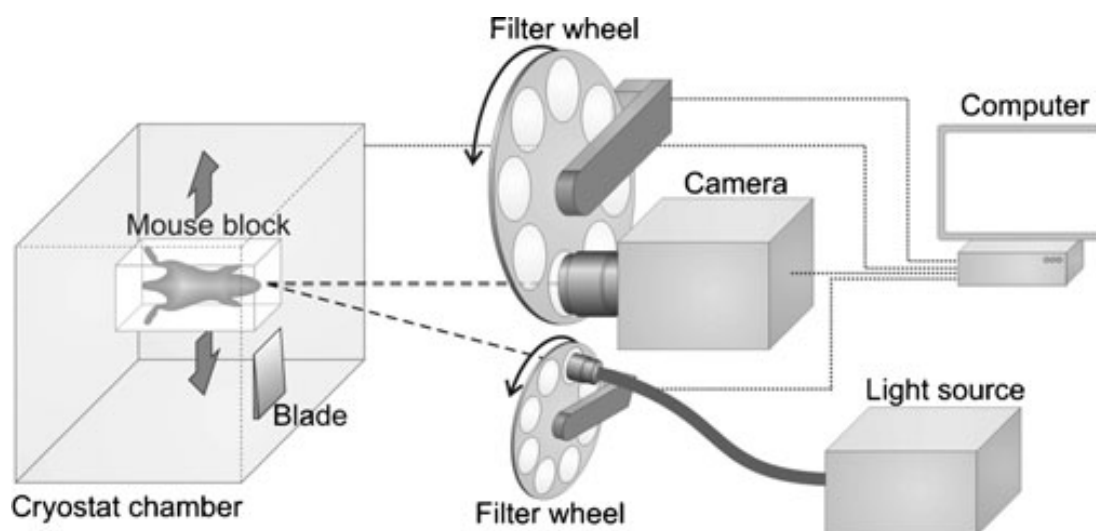


Figure 2-2: Schematic of the custom made imaging set-up using scanning filter wheels both the excitation and the emission. During the sectioning procedure, the mouse block is moving with respect to the blade and therefore the image plane remains constantly at the same distance from the camera.

Imaging system description

The multispectral cryoslicing imaging system (Fig. 2-2) developed consists of a 250 W halogen lamp white light source (KL2500 LCD, Carl Zeiss AG, Oberkochen, Germany) coupled via a flexible fiber optic bundle to a 6-position filter wheel (FW102B, Thorlabs, Newton, NJ, USA), which controls the selection of the excitation filters. A sensitive, high-resolution electron multiplying CCD camera (Luca-R, Andor Technology, Belfast, UK), a zoom objective lens (Nikkor 24–85 mm, Tokyo, Japan), and a custom 10-position filter wheel (Cairn Research Ltd., Kent, UK) capture reflectance and fluorescence images at multiple spectral bands. The field of view of the system ranges from 63.6×46.8 to 18×13.2 mm. As the camera used is monochrome, with emphasis on extended sensitivity range to the near-infrared area of the spectrum, the color information of the sample is obtained

with red, green, and blue filters from which a composite color image is produced. The camera system is mounted onto a rotary cryomicrotome (CM 1950, Leica Microsystems GmbH, Wetzlar, Germany) by a custom made construction. Specially designed software and algorithms developed using the Matlab (Mathworks, Natick, MA, USA) and LabView (National Instruments, Austin, TX, USA) software platforms control the sectioning procedure of the cryotome and the image acquisition of the optical system.

Standard interchangeable blades are utilized in the cryotome and are capable of slicing small animals or organs in both the axial and the lateral direction. The typical range of slice thicknesses that was experimentally achieved for adult mice is 5–40 μm . The maximum specimen size is physically restricted by the dimensions of the cryotome chamber and currently measures 50×70×80 mm (width × height × depth), which is generally sufficient for small animal imaging. The sectioning action is automated using an external stepper motor (Sanyo Denki, Japan) and a motion controller (Velmex, Bloomfield, New York) which is computer-operated via LabView. The procedural steps followed during an imaging session for one sample face include: (a) consequent sectioning of the desired, computer-controlled, number of slices and corresponding section removal using the cryotome's built-in vacuum suction unit, (b) acquisition of red, green, and blue images using cross-polarized white light, and (c) imaging at both the excitation (reflectance) and emission (fluorescence) wavelength of the exposed sample block for each studied fluorophore. Alternatively multispectral imaging of a single fluorophore throughout its fluorescence emission spectrum, i.e depending on the selection of filters employed, is also possible. Computer automation not only allows accurate positioning but it also provides the possibility of altering various imaging parameters such as the slice thickness imaged for coarser or thinner imaging and the number of wavelength measurements utilized in each imaging session depending on the particular fluorochromes used in the study. In addition, due to unavoidable minor movement (at the micron range) of the camera system relative to the tissue imaged, there may be shifts observed between slices. For this purpose, carbon

rods are used as reference points and an automatic identification algorithm aids in shifting the images so that accurate alignment is ensured for the entire volumetric series of images.

Moreover, the custom set-up construction has been developed in such a way that by pausing the imaging procedure, the cryotome can still be used for collecting samples for histopathology as none of the essential cryotome equipment has been modified. This feature is of great importance, as it provides the possibility to directly compare histological analysis and staining results with anatomical features and fluorescent distribution of multiple fluorophores on the same sample.

User Interface

Fig. 2-3 displays a typical version of the main software interface designed for imaging of two fluorophores. The interface is designed in LabView and features separate “windows” for the display of every captured image (red, green, blue, intrinsic and fluorescence for every fluorophore). After every channel acquires an image, it is automatically saved as tiff file with an appropriate name. The exposure times for the Red, Green, Blue and intrinsic channels are calculated in the beginning of the experiment and are kept constant throughout its duration. In contrast, before the acquisition of all fluorescence images a custom auto-exposure algorithm calculates the appropriate exposure time to ensure that the dynamic range of the image remains unchanged under alternating fluorescence signal intensities. The exposure times of all fluorescence images are separately stored in Matlab files for post-processing (normalization). Finally, several additional user-oriented “services” are integrated at the interface. The number of saturated pixels for every image is constantly calculated and informs the user for over-exposure. Correspondingly, the minimum and maximum pixel counts are also displayed to notify in case of under-exposure. A vivid “imaging button” is used to make users aware that the imaging system is active and therefore access in the cryotome chamber (for instance to collect tissue samples) is therefore not advisable.

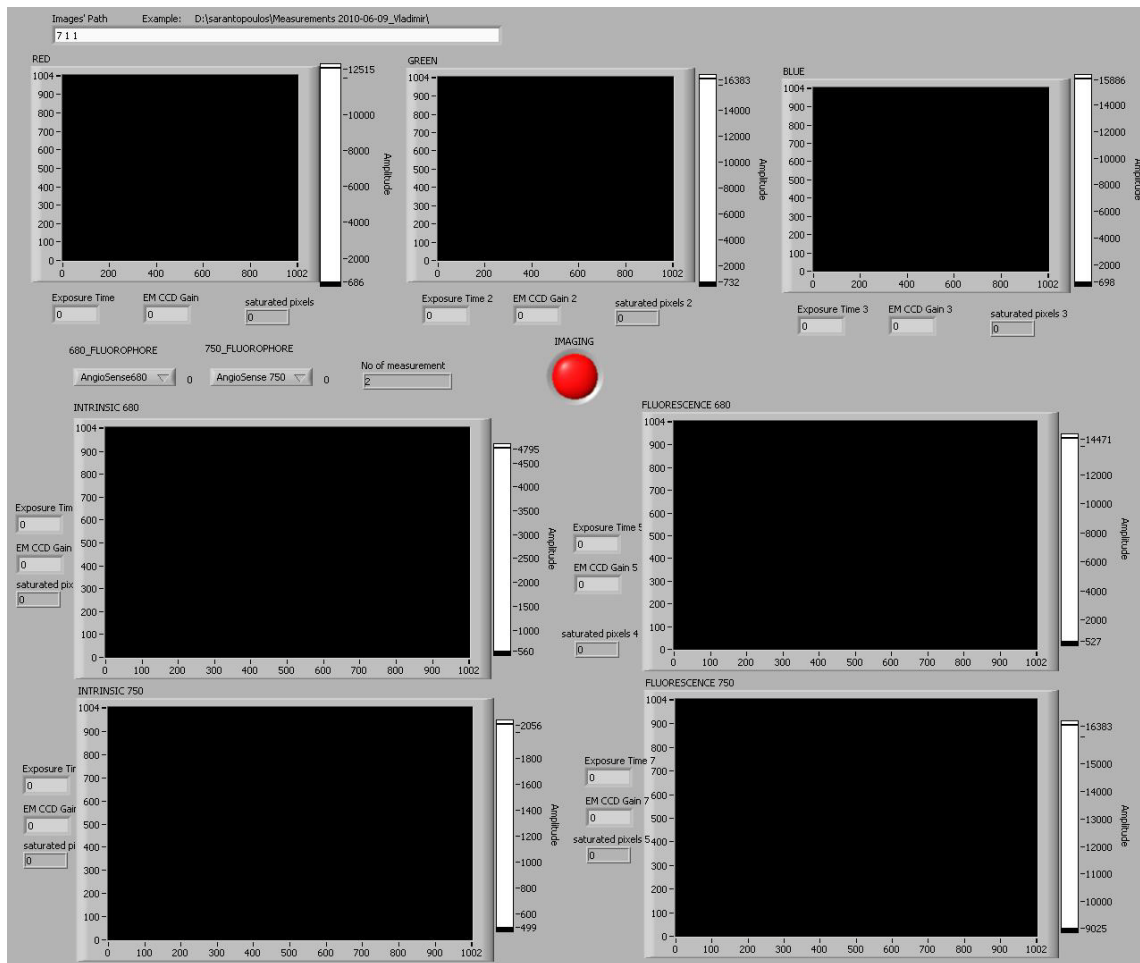


Figure 2-3: The User Interface of the cryoslicing modality. During the sectioning procedure, the mouse block is moving with respect to the blade and therefore the image plane remains constantly at the same distance from the camera.

Sample Preparation

Euthanized animals are fast frozen in an -80°C freezer (New Brunswick Scientific, Edison, NJ, USA) or alternatively in liquid nitrogen. Using a tube as a mold, frozen samples are then embedded in a 25:1 mixture of Optimal cutting temperature (OCT, Sakura) medium and India ink. OCT is widely used as a medium to embed tissue samples before the cryosectioning procedure and histopathological analysis. Since excitation of sub-surface tissue layers is by definition unavoidable (more on that in Chapter 4), the ink is added to the

embedding medium so as to absorb scattered photons that originate from underlying tissue surfaces and propagate towards the sample surface.

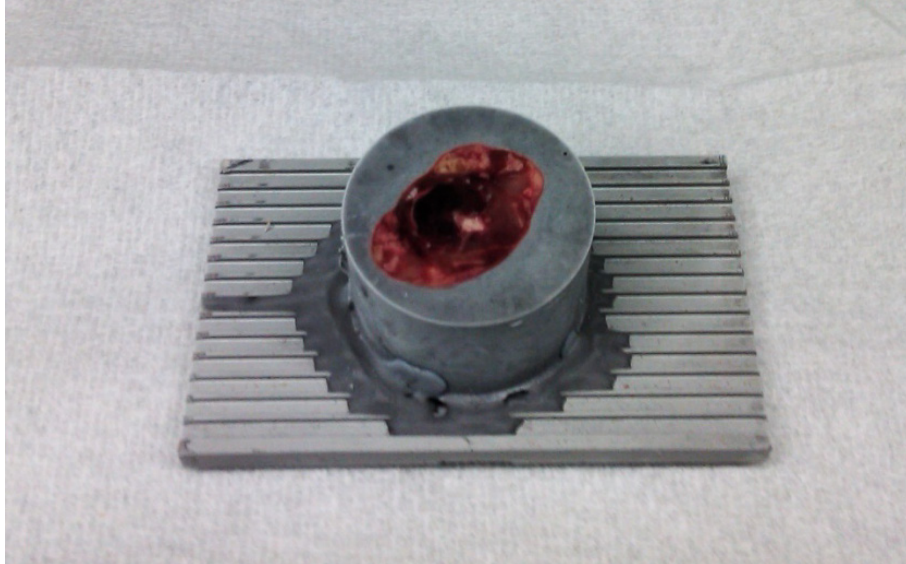


Figure 2-4. A mouse sample embedded in the OCT-India ink mixture. The photograph was taken during the sectioning procedure after the sample was removed from the cryoslicer.

Thus, the ink addition eliminates the formation of “halos” that can be observed in the fluorescence images due to strong scattering nature of the frozen OCT medium. Additionally, two carbon rods (with a diameter of 0.7 mm) are also immersed in the embedding medium prior to freezing. The rods serve as fiducials (reference points) for the post-processing registration of the images in order to track any translation, rotation, or scaling during the image acquisition. Once the sample is frozen, a thin layer of OCT-India ink mixture is positioned between the mouse block and the cryotome stage and the final sample is placed again shortly inside the freezer. In this case, the embedding medium acts as a bonding agent between the two surfaces and fixes the sample on the cryotome stage. Optimal imaging results are achieved when the temperature of the cryotome during the sectioning procedure is maintained to around -23°C . The samples are typically sectioned axially although other slicing orientations are possible, because in this way, cranial bones that frequently damage the cryotome blades are present in fewer sections. In this cutting

direction, mice are typically imaged in two halves due to space restrictions, i.e. the head is imaged separately than the body after dissection at the neck.

2.4 Studies

2.4.1 Bio-distribution in healthy mice

Introduction

Fluorescent molecular probes due to their chemical compositions and targeting characteristics are expected to distribute differently in diseased organisms. However, not much is still known about their spreading patterns in healthy animals. We constructed, thus, an animal study with the hypothesis that fluorescent biomarkers should also distribute with distinct patterns under normal circumstances.

Studied animals

Three healthy nude mice (Crl:NU/NU:Foxn1nu, Charles River Research Laboratories, Margate, UK) were administered with two different near-infrared fluorescent probes (2 nmol each) via a bolus intravenous injection in the tail vein. The fluorescent probes utilized were IntegriSense™ 750 (VisEn Medical Woburn MA, USA), targeting the $\alpha\beta3$ -integrin receptor and AngioSense™ 680 (VisEn Medical Woburn MA, USA), a non-specific fluorescent agent used to image vasculature and vessel leakage. Corresponding to their name, IntegriSense750 has its absorption and emission maxima at 755 and 775 nm, whereby AngioSense680 at 680 and 700 nm, respectively. The blood half-life of AngioSense is approximately 6 h (Montet, Figueiredo et al. 2007), while the pharmacokinetics of

IntegriSense in plasma fit into a two compartmental model showing rapid distribution ($t_{1(1/2)}=6$ min) and a long terminal half-life ($t_{2(1/2)}= 200$ min) (Kossodo, Pickarski et al. 2010). For control measurements, we employed a mouse injected only with PBS (phosphate-buffered saline). Six hours after the administration of the fluorescent probes, all animals were euthanized with an intraperitoneal injection of xylazine (250 mg/kg, Rompun, Bayer) and ketamine (800 mg/kg, Ketalar, Parke-Davis).

Imaging procedure

Every mouse was sectioned in the axial direction and imaged every 125 μ m. Color reflectance and fluorescence images for the 680nm-channel (excitation: 665nm center wavelength with 40nm bandwidth, emission: 715nm center wavelength with 40nm bandwidth) and for the 750nm-channel (excitation: 740nm center wavelength with 40nm bandwidth, emission: 785nm long pass filter) were captured after every section. The 6-h post-injection time point was chosen as a compromise between the suggested short post-injection imaging time lapse of AngioSense and the prolonged one of IntegriSense. Taking into account that the mice were healthy, we were interested in discriminating the prominent accumulation sites of the probes and not their actual disease targeting potential. In this way, the two fluorophores were allowed to circulate, bind, and distribute inside the mouse before they were cleared by tissue (typically after 24 h).

Results

Figures 2-3, 2-4, 2-5, and 2-6 demonstrate the distribution patterns of the probes studied using different cross-sections from experimental and control mice at different imaging planes inside the mice body, namely the mouth (Fig. 2-3), nasal cavity (Fig. 2-4), lung (Fig. 2-5), and kidneys (Fig. 2-6). For each section, there is a color image from an experimental and a control mouse depicting the anatomy. As different mice were used for

the auto-fluorescence measurements attention was taken so that the cross-sections come from equivalent geometry or depict the same organs and structures in all images. In addition, there are fluorescent images that show the distribution for each probe and the auto-fluorescence measured. The auto-fluorescence images are displayed at two color scales; one using the same grayscale used in the probe bio-distribution images for direct comparison and a second that scales the auto-fluorescence images to achieve better contrast. The scaling factor is written below every image. Due to the different chemical structure of the two probes used, significant bio-distribution changes are observed. AngioSense shows accumulation preference to the lung and the mouth region (especially the tongue), but otherwise distributes evenly in the mouse body, while IntegriSense is mostly concentrated in the kidneys, the skeletal system (spinal cord, rib cage, and limbs), and to a lesser extent, in muscle tissue. In the lung volume especially the two fluorescent probes appear to distribute in a totally opposite way with AngioSense accumulating inside the lung and IntegriSense in the surrounding muscle tissue. A strong signal observed in the gastrointestinal system (stomach, intestine, and colon) is also present in the control measurements, and it is therefore attributed to the mouse diet, as the animals did not

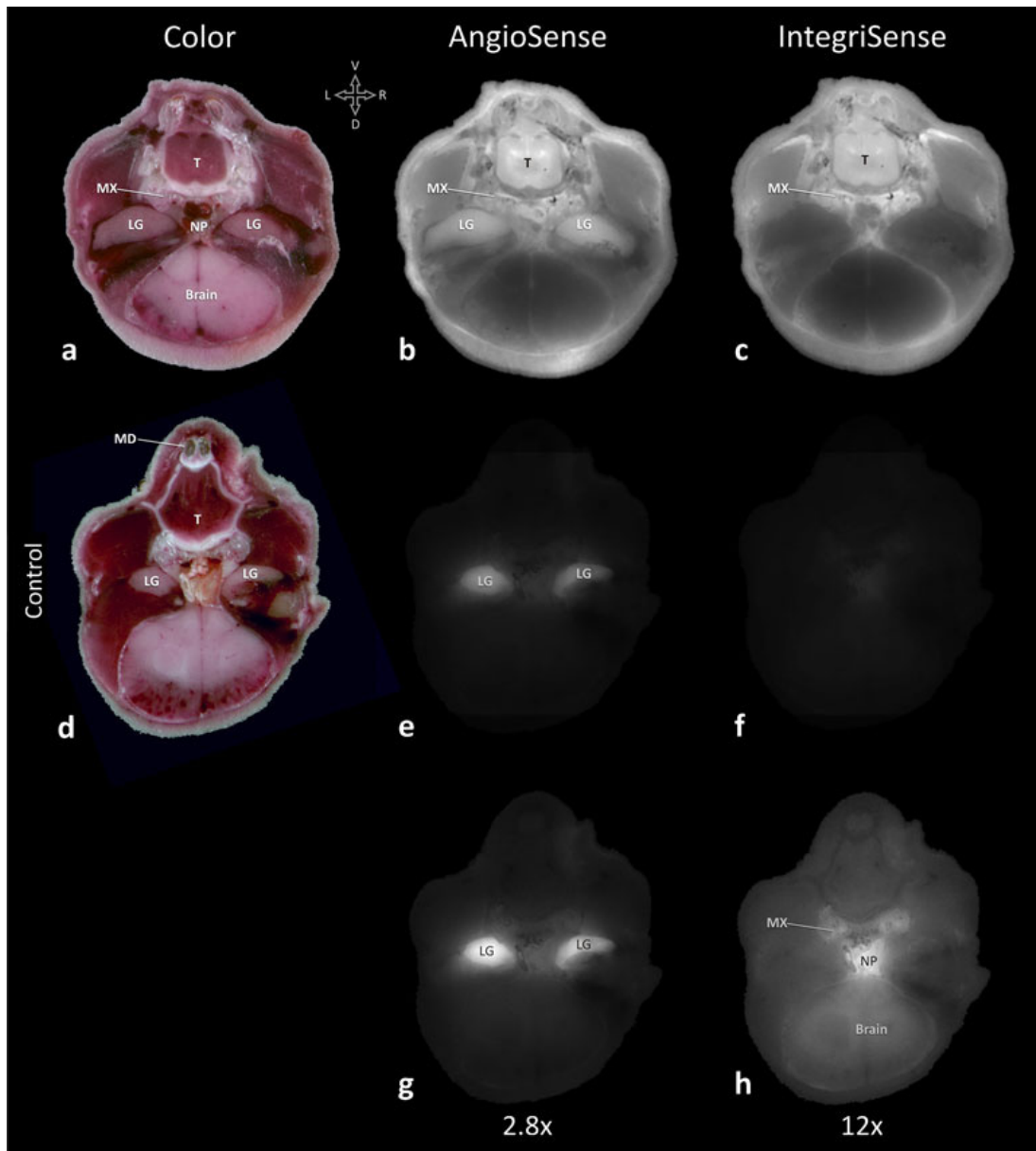


Figure 2-5. Cross-sections at the mouth level showing the anatomy in the probe-injected (a) and control mouse (d) and the distributions of AngioSense (b) and IntegriSense (c) and auto-fluorescence (e, f, g, h). g and h have been scaled with the factor at the bottom of every image for visualization purpose. Note the strong auto-fluorescence signal from the lacrimal gland. L left, R right, D dorsal, V ventral, T tongue, LG lacrimal gland, MX maxilla, NP nasopharynx, MD mandible.

receive special non-fluorescent food. Overall however, tissue auto-fluorescence was found to be at least one order of magnitude weaker than the signal of the probe-injected animals

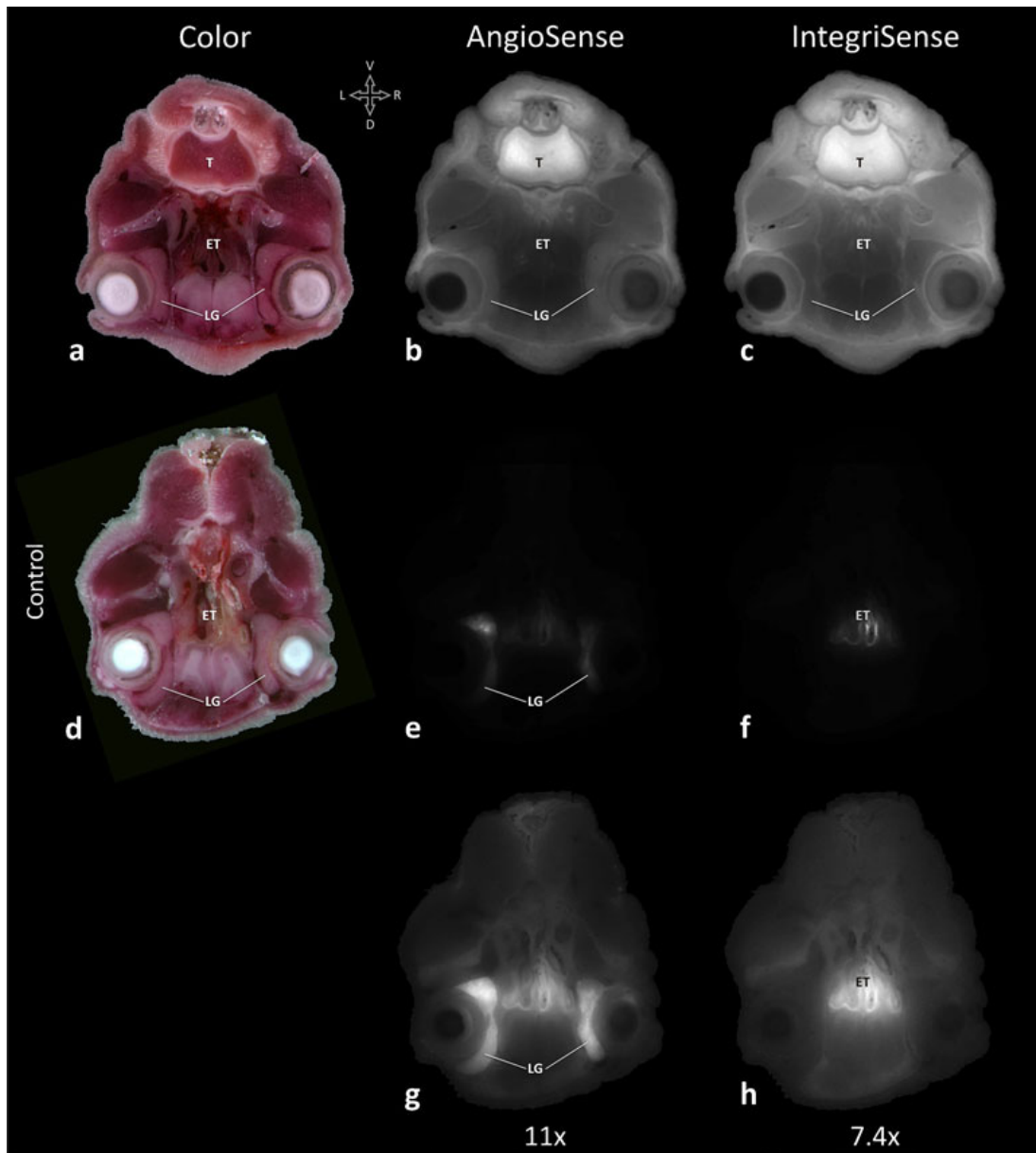


Figure 2-6. Cross-sections at the nasal cavity level showing the anatomy in the probe-injected (a) and control mouse (d) and the distributions of AngioSense (b) and IntegriSense (c) and auto-fluorescence (e, f, g, h). g and h have been scaled with the factor at the bottom of every image for visualization purpose. L left, R right, D dorsal, V ventral, T tongue, LG lacrimal gland, ET endoturbinates.

in the structures shown, with the exception of the lachrymal gland (Fig. 2-3) and the spleen (Fig. 2-6).

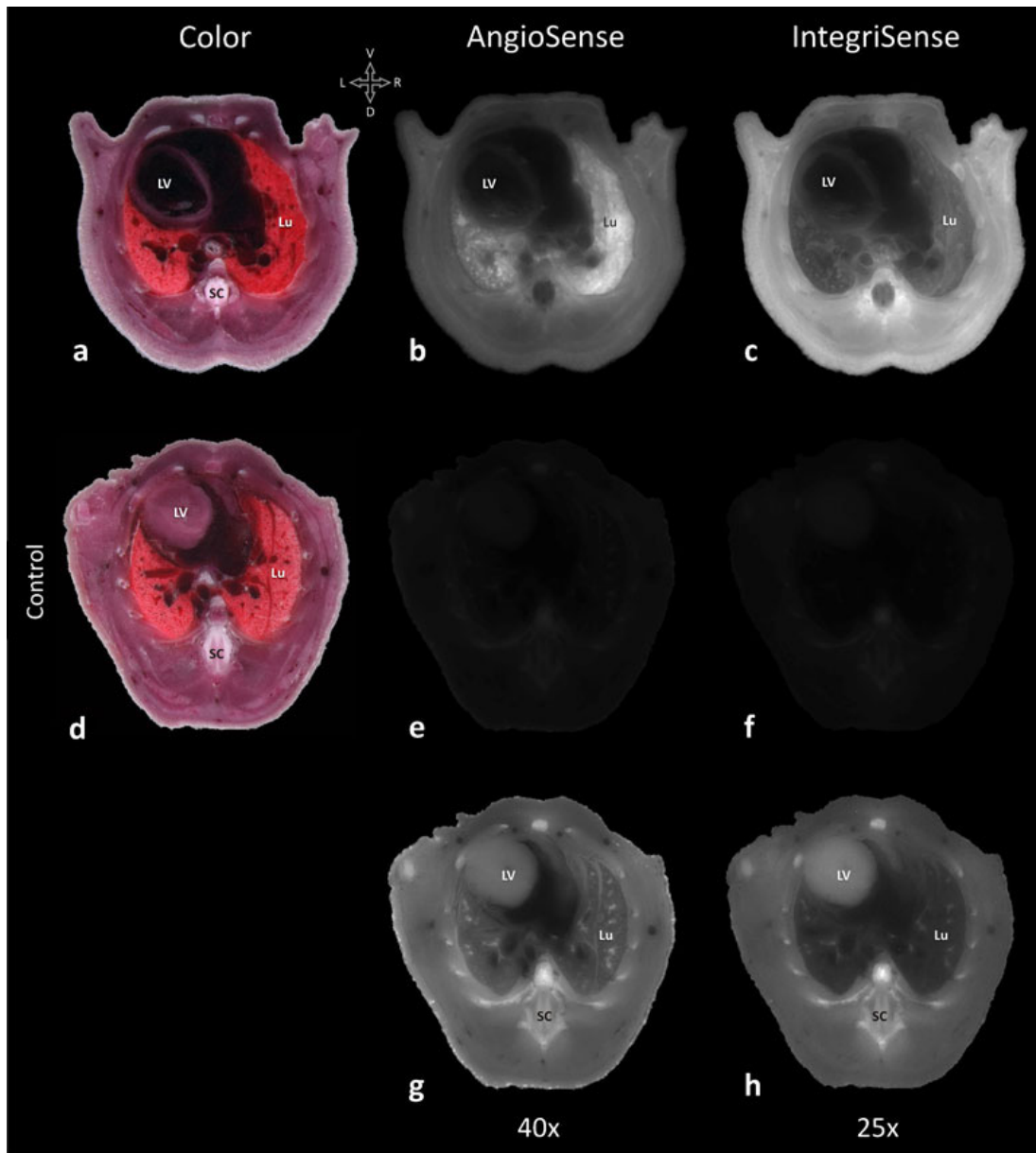


Figure 2-7. Cross-sections at the lung level showing the anatomy in the probe-injected (a) and control mouse (d) and the distributions of AngioSense (b) and IntegriSense (c) and auto-fluorescence (e, f, g, h). g and h have been scaled with the factor at the bottom of every image for visualization purpose. L left, R right, D dorsal, V ventral, SC spinal cord, Lu lung, LV left ventricle of the heart.

Based on the series of axial images collected and after the alignment procedure, sagittal images could also be reconstructed, as shown in Fig. 2-7. The imaging plane shown passes through the center of the mouse and depicts most of the major organs and

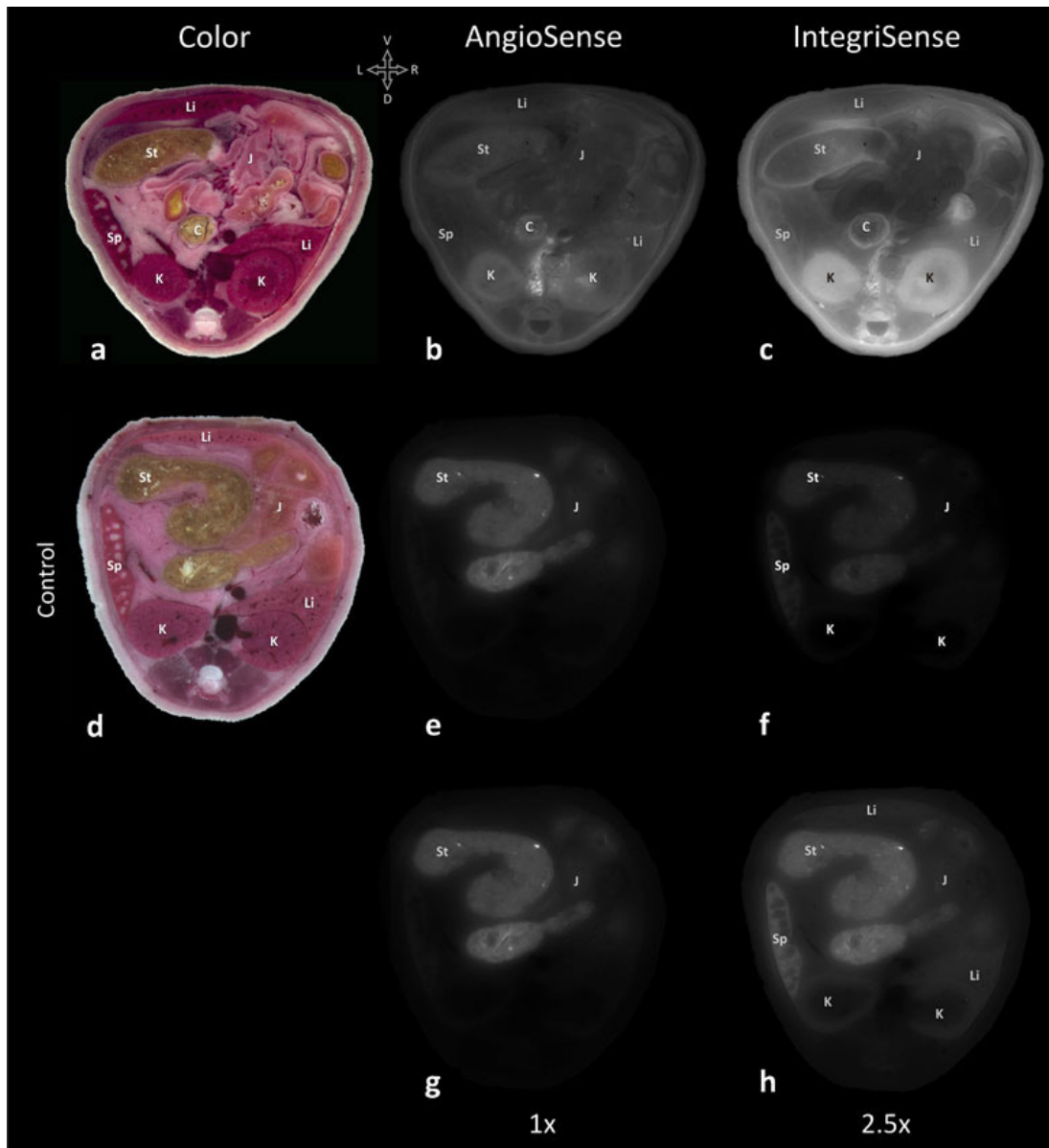


Figure 2-8. Cross-sections at the kidneys level showing the anatomy in the probe-injected (a) and control mouse (d) and the distributions of AngioSense (b) and IntegriSense (c) and auto-fluorescence (e, f, g, h). g and h have been scaled with the factor at the bottom of every image for visualization purpose. L left, R right, D dorsal, V ventral, K kidney, Li liver, Sp spleen, St stomach, C colon, J jejunum.

structures. Such visualizations can be produced from the registered image series also for oblique cutting planes and generally for imaging of random geometry. These views allow comparisons of bio-distribution along different organs and internal structures.

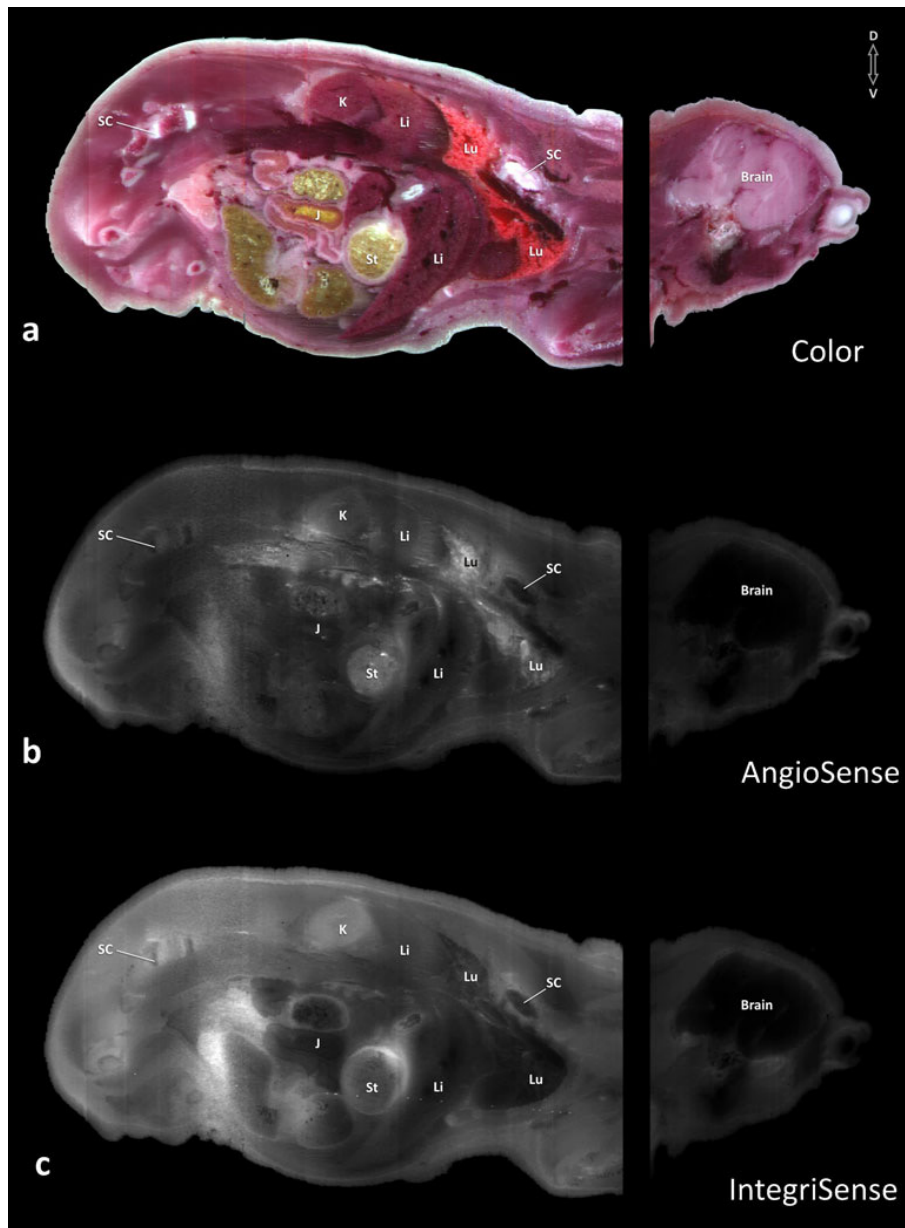


Figure 2-9. A sagittal section reconstructed from the original data. Color image (a) and fluorescent signal representing the distribution of AngioSense (b) and IntegriSense (c). D dorsal, V ventral, K kidney, St stomach, J jejunum, Lu lung, Li liver, SC spinal cord.

An alternative visualization method of fluorochrome bio-distribution is shown in Fig. 2-8. The method appends to each voxel a different opacity depending of its fluorescent signal intensity and it is implemented in Amira (Visage Imaging GmbH, Berlin, Germany)

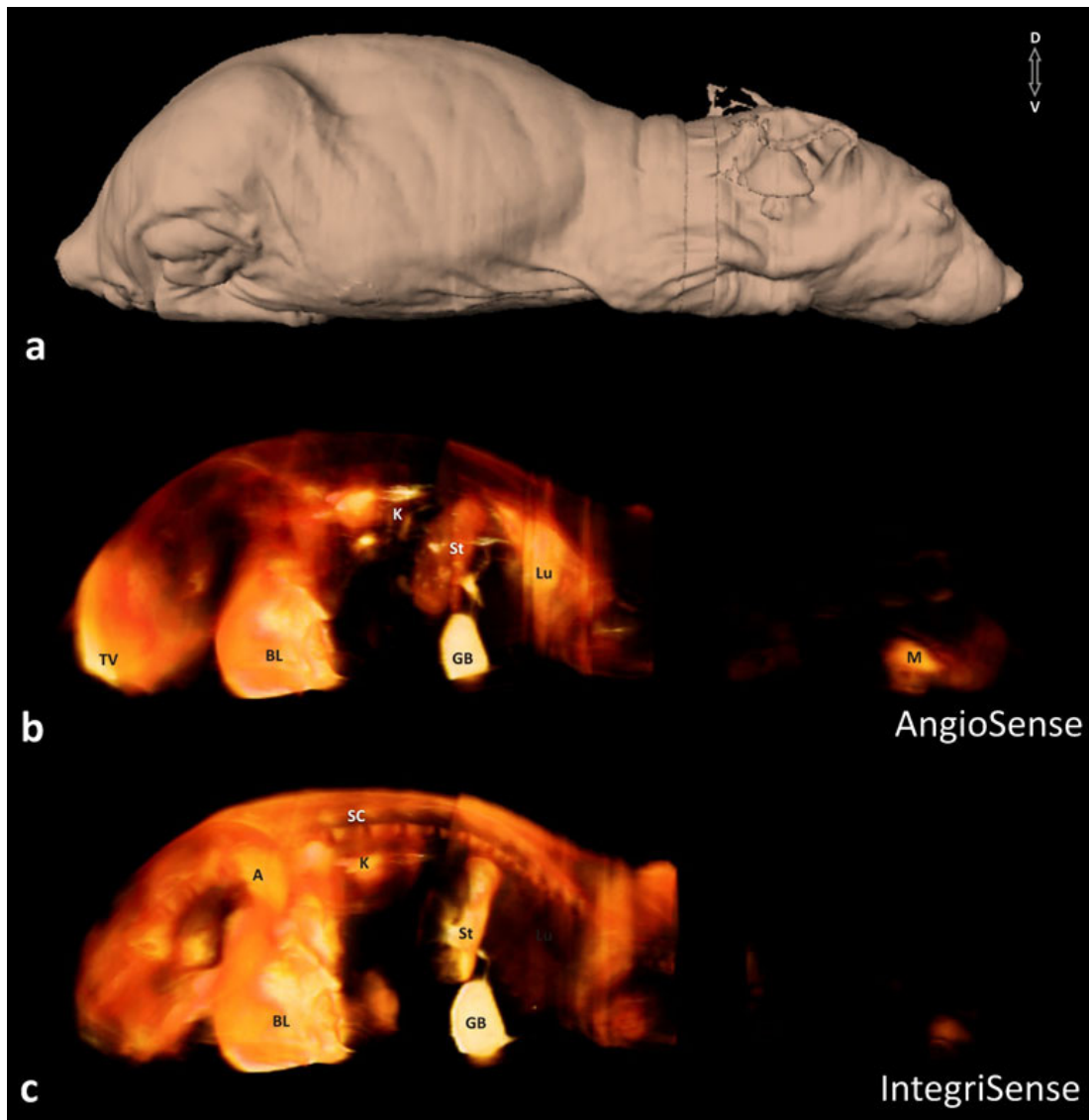


Figure 2-10. Whole mouse body reconstruction(a) and 3D bio-distribution of the two injected contrast agents, i.e., AngioSense (b) and IntegriSense(c). Note how AngioSense spreads primarily at the center of the mouse body and especially in the lung, while IntegriSense is distributed in the abdominal area and around the spinal column. One can also notice the leakage near the tail vein (Fig. 2-8b). D dorsal, V ventral, K kidney, Lu lung, St stomach, BL bladder, GB gall bladder, A abdomen, TV tail vein.

through the built-in maximum intensity projection (MIP) algorithm. Thus, the voxels with a strong fluorescent signal are opaque and with a color ranging from dark red (low intensity) to white (high intensity) while those with a weaker signal are transparent. It is evident on Fig. 2-8 that the strongest signal of all probe-injected mice comes from the urinary system

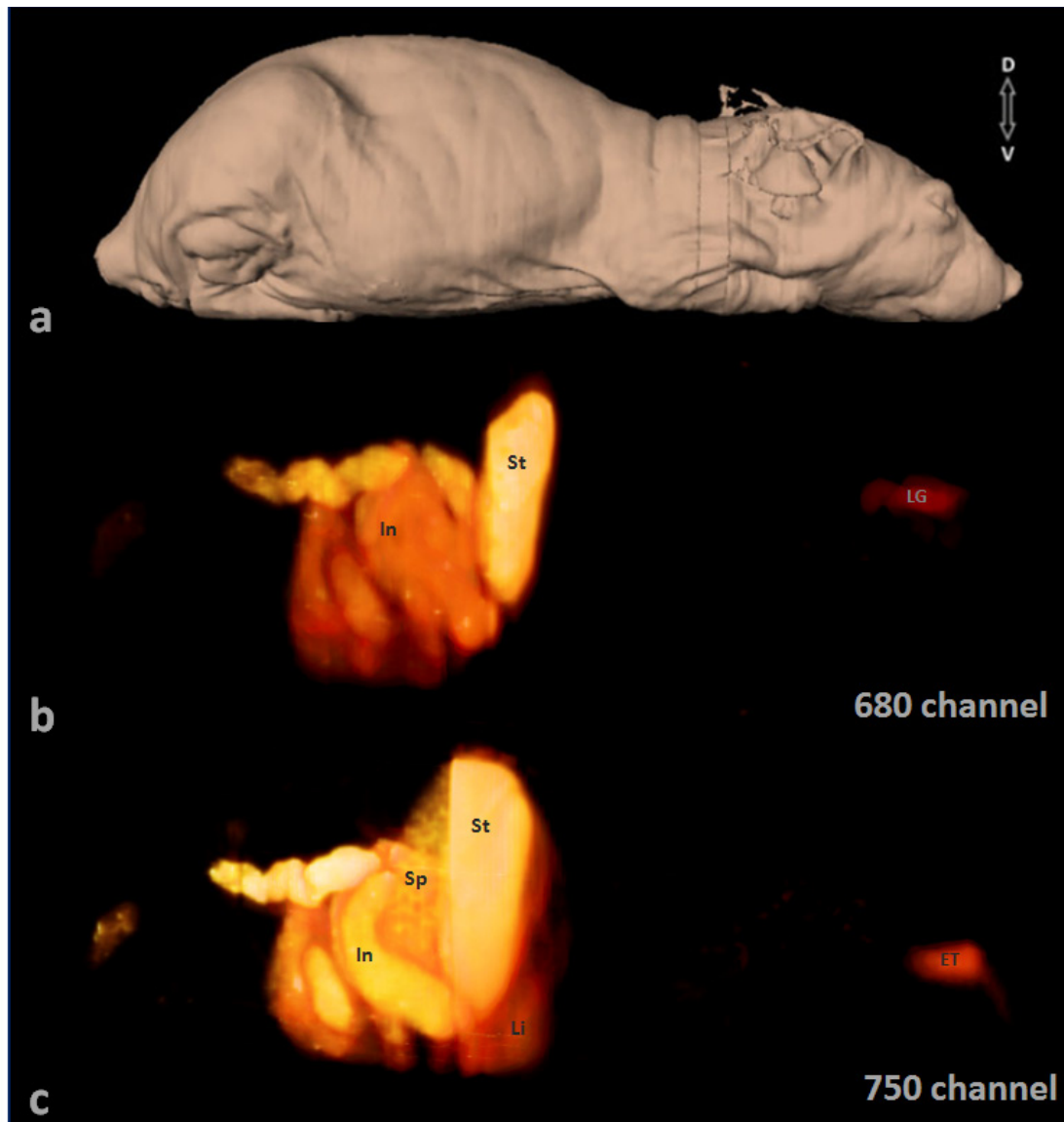


Figure 2-11. Whole mouse body orientation (a) and 3D bio-distribution of the PBS-injected mouse. Auto-fluorescence m.i.p. for the 680nm channel (b) and for the 750nm channel (c). Note that both channels are primarily affected from high fluorescence levels in the intestinal tract due to the chemical structure of the standard mouse diet. Tissue auto-fluorescence is generated only from very specific structures, namely the lachrymal gland for the 680nm-channel and the spleen and endoturbinates for the 750nm-channel. D dorsal, V ventral, , Lu lung, St stomach, Sp spleen, Li liver, In intestine, LG lachrymal gland, ET endoturbinates.

(bladder, gall bladder, etc.), which is consistent with the bio-distribution expected 6-h post-injection. This approach allows us to directly compare and visualize the signal strength of

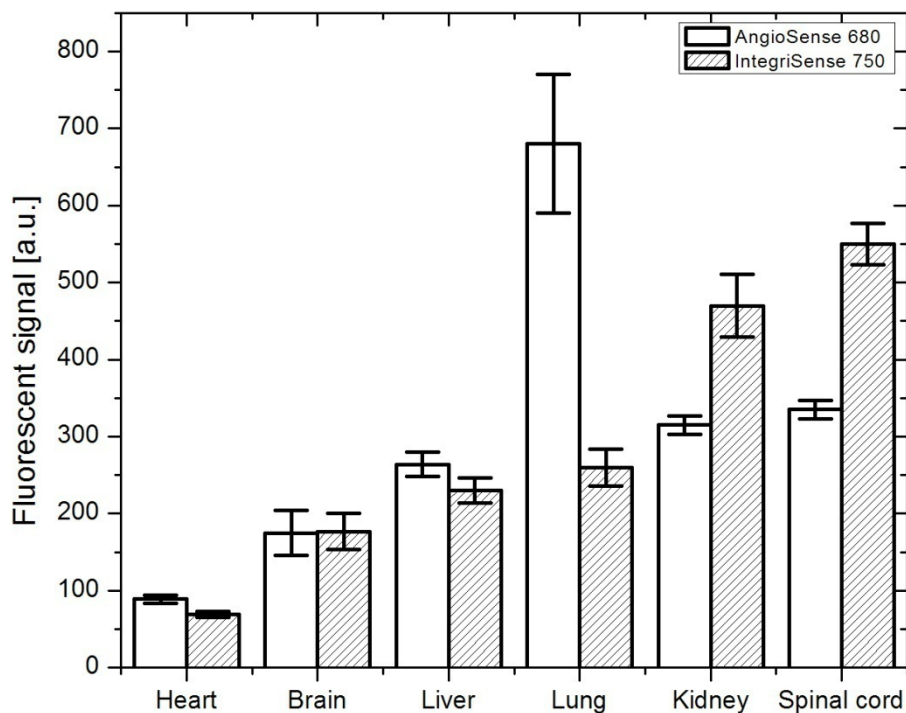


Figure 2-12. Volumetrically analyzed bio-distribution (mean intensity and standard deviation) of accumulated fluorophores in individual organs per voxel.

different organs and structures inside the whole mouse body and recognize the significant build-up of AngioSense in the lung and the mouth and of IntegriSense around the spinal cord.

Additionally, in Fig. 2-8b, an intense signal coming from the tail area is observed, attributed in this case to possible leakage at that area during the injection of the probes. In Fig 2-9 the 3D bio-distribution of the auto-fluorescence at both imaging channels is displayed. Especially in the 680nm-channel it is evident that almost all the signal (with the exception of the lachrymal gland) is situated in the intestinal system in general and predominantly in the stomach, caused by the animal's diet ingredients (most commonly chlorophyll). In the 750nm-channel the auto-fluorescence is similarly distributed in the abdominal area, while the contribution other organs like the spleen and the liver is hardly noticeable. It is interesting however to note that despite the use of usual food diet, the

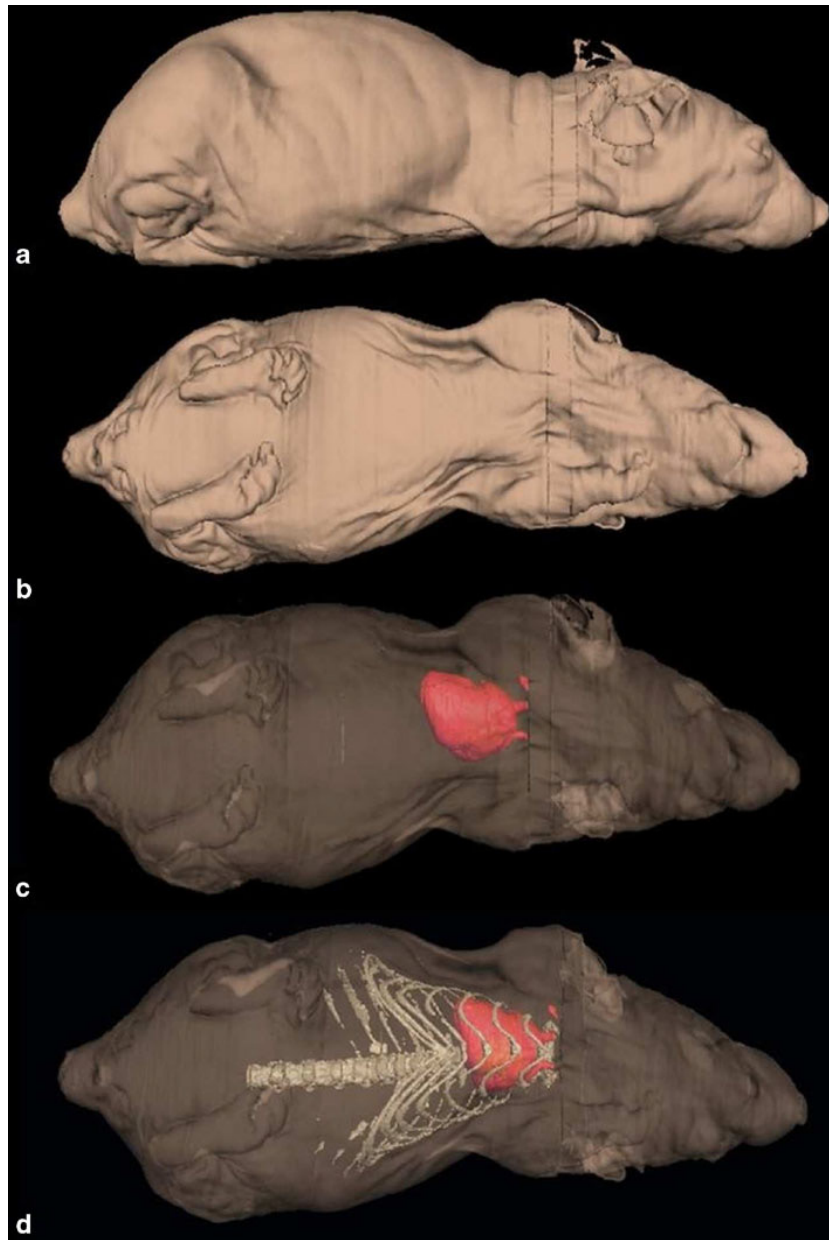


Figure 2-13. Automatic mouse body and internal structure segmentations as a result of thresholding the fluorescent signal. The whole mouse body at two different angles (a, b), the heart (c, d) and spinal cord (d) of the animal are reconstructed with elaborate details.

amplitude of the auto-fluorescence signals is distinctly lower when compared to the probe-induced fluorescence levels.

The ability to volumetrically resolve signals offers the possibility to accurately quantify fluorochrome bio-distribution. This is a big advantage of the multispectral cryoslicing modality compared to conventional planar imaging as there is, now, no uncertainty concerning the inner organ probe accumulation levels. By employing manual segmentations, we delineated the major organs in all probe-injected animals (n=3). Subsequently, we used these segmentations in order to acquire cumulative statistics for the two fluorescent probes bio-distribution on a per organ basis in all three animals. In Fig. 2-11, we calculate the mean value and standard deviation of the fluorescent signal intensity of all voxels per organ for each probe. AngioSense is thus shown to accumulate at least two times stronger in the lung than in other internal organs, while IntegriSense follows a flatter distribution pattern, distributing evenly inside the mouse body with only slightly elevated levels in the spinal cord.

Finally, Fig. 2-10 shows the results of automatic and semiautomatic segmentations and three-dimensional renderings of the data collected. Fig. 2-10a and 2-10b illustrate the result of an automatic segmentation procedure based on applying a threshold to distinguish the fluorescent signal coming from the mouse skin and consequently the mouse body. This segmentation can be used to render the original shape and appearance of the animal with high-resolution details (i.e., skin foldings, toes, etc.) benefiting from the large number (660 in total in this case) of transverse sections available. Internal structures can also be segmented and rendered based on their color appearance of fluorescence intensity information; Fig. 2-10c depicts the results of applying a threshold in order to separate the darkest pixels in the fluorescent image, a process that identifies large blood vessels and essentially the heart tissue. Other structures can also be segmented based on their color appearance using the RGB composite images. One such case is the spinal cord (Fig. 2-10d), which can be segmented using the color reflectance images and specifically the green channel. As bones appear brighter than other internal structures in this channel, these voxels can be rendered and discerned from the rest of the mouse body by making use of a threshold.

Discussion

In conclusion, we have studied in high resolution the distribution of IntegriSense, AngioSense, and auto-fluorescence in nude mice. Using spectral differentiation, the relative bio-distribution of the probes can be studied in the same animal, which allows for accurate comparisons and precise superposition of fluorescence signals on the anatomical images. We observed notable changes in the distribution of the probes (e.g., in the kidneys and skeletal system), and sites of accumulation that were not evidently identified in the past (e.g., the accumulation of AngioSense to the lung and mouth region).

This study shows the tendency of each agent to accumulate in specific structures due to their different molecule characteristics and their targeting and bio-distribution mechanisms. While *ex-vivo* imaging does not offer the power of dynamic interrogations available to *in-vivo* imaging, the results presented herein showcase that multispectral 3D cryoslicing imaging can offer important insights to yet unknown parameters relating to fluorescence probe imaging in small animals. The selected time point where cryoslicing is performed could be however selected based on *in vivo* optical imaging observations and used to validate or to more accurately observe and explain the origin of findings that are already evident on *in vivo* imaging approaches; offering in this case higher resolution and sensitivity.

The approach selected herein operates around a commercially available cryoslicer that is typically found in the biomedical laboratory and can be easily adapted for the investigation of a larger number of fluorescence studies in tissues, including the study of the distribution of different probes, the bio-distribution of probes in animal models of various diseases such as cancer, cardiovascular disease or neuro-degeneration, or the expression patterns of fluorescent proteins. It is expected that such an approach can be especially important also in the development of diagnostic or therapeutic agents, since fluorescence-labeled agents or drugs can be similarly visualized in whole animals.

Overall, 3D epi-illumination fluorescence cryoslicing imaging offers an easy to

implement but powerful and more systematic approach in the study of fluorescent probes' bio-distribution and potentially the study of diseases, and it can emerge as an alternative imaging approach in preclinical and potentially clinical optical imaging.

2.4.2 Bio-distribution in a xenograft mouse model

Introduction

In this study our aim was to observe the bio-distribution specifics of two near-infrared fluorescent agents in diseased animals. Xenograft mouse models were the preferred animal model due to their attractive characteristics of short tumor development period and simplicity to induce tumor growth. 4T1 (murine breast cancer) tumor cells are known to express a series of proteins during the various stages of their development, integrins among them as well. Xenografts with 4T1 cells serve as models for stage IV breast cancer (Kossodo, Pickarski et al. 2010) and grow rapidly to develop solid and dense primary tumors. Furthermore, 4T1 xenografts were to our prior knowledge identified of building leaky, incomplete and generally irregular tumor vasculature mainly due to their rapid development kinetics.

Under the scope of this study we decided to induce not one but two subcutaneous tumors for every animal in order to visualize different time points during the process of tumor growth. Thus we implanted different amounts of cells at two separate sites of the mice thorax. In the end we resulted in having two tumors per animal, each one reflecting a different stage during tumor development, in order to distinguish different bio-distribution patterns between the fluorescent biomarkers.

Studied animals

A breast cancer xenograft model was established by implanting nude mice with 0.4 million and 0.8 million 4T1 cells at different sites on the mammary fat pad. Under daily monitoring they were allowed to grow for 8-10 days until they reached sizes of around 4 and 8mm in diameter respectively. At this point the animals were administered with IntegriSense680 and AngioSense750 (2 nmol each) via a bolus intravenous injection in the tail vein (probe specifics described previously in Chapter 2.4.1.). 24 hours after the administration of the fluorescent probes, all animals were euthanized with an intraperitoneal injection of xylazine and ketamine mixture. All procedures were performed in compliance with the Guide for the Care and Use of Laboratory Animal Resources (1996) and were approved by the local Animal Care and Use Committee.

Sectioning procedure

Every mouse was sectioned in the axial direction and imaged every 125 μ m covering the whole mouse volume from the head to the kidneys area. Color reflectance, intrinsic and fluorescence images for the 680nm-channel and for the 750nm-channel were captured after every section. The 24-h post-injection time point was chosen based on the suggested post-injection imaging time period of IntegriSense. At the same time enough time for AngioSense clearance was provided in order to visualize only vessel leakage and prevent imaging of unbound, still circulating probe contributions.

Results

Fig. 2-12 shows cross-sectional color and fluorescence images for both fluorescent agents at two different heights of the mouse thorax depicting the two implanted tumors. The exact position of the cross-sections with regards to the whole mouse volume is also noted in Fig. 2-13 for a better overview. Although at first both probes seem to have comparable fluorescence bio-distributions, on a closer look, one can observe that

IntegriSense is mostly accumulated inside the tumors. In contrast, AngioSense displays brighter signals in the periphery than inside the tumor (blue arrows). This effect is more pronounced for the larger tumor on the right mouse side. It is evident that in this way AngioSense is mostly trapped in leaky and incomplete vasculature surrounding the tumor rather than the relatively more developed blood vessels found inside of it. Especially in Fig. 2-12c AngioSense seems to have spread at the whole area directly next to the right mouse tumor, which has a red color appearance in Fig. 2-12a, where most probably the newest blood vessels were developing. Interestingly, despite the strong IntegriSense accumulation inside the tumors, a part of the marker still bound in the skeletal system of the mouse, a site of accumulation for this particular probe pointed out by the healthy mouse study of Chapter 2.4.1., as shown in Fig. 2-12e by the signal originating from the spinal cord and the shoulder blades. In contrast, no buildup of AngioSense could be observed inside the mouse

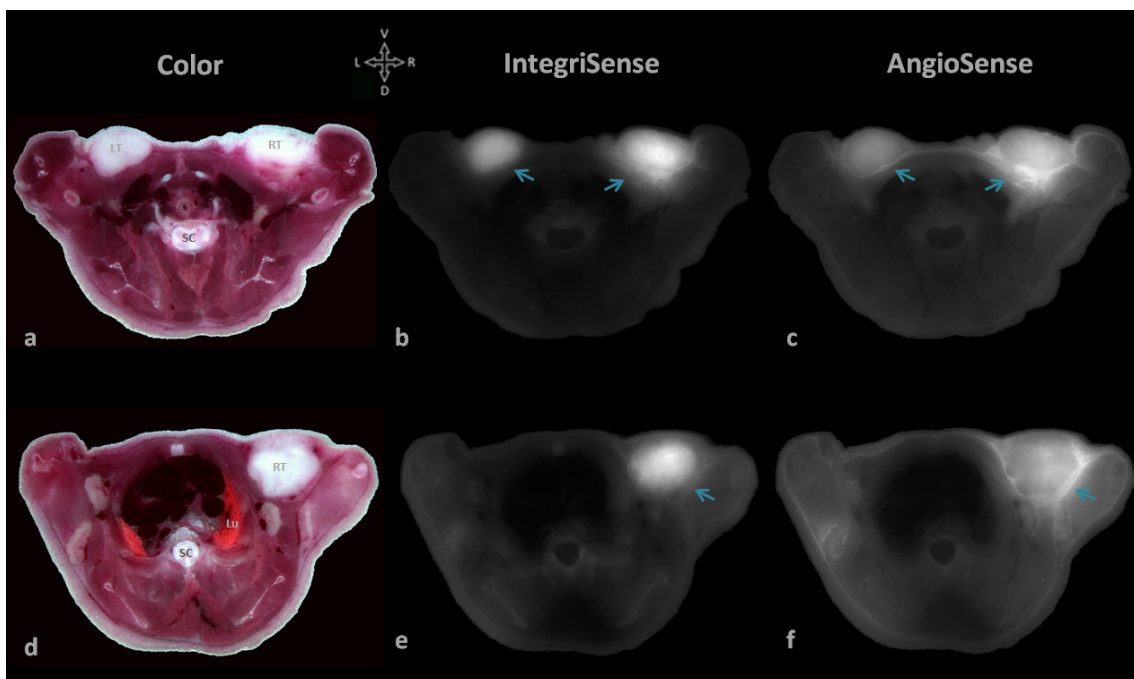


Figure 2-14. Cross-sections at two different levels of the thorax showing the anatomy (a, d) in the xenograft mouse (d) and the distributions of AngioSense (c, f) and IntegriSense (b, e). Every image has been scaled accordingly for clarity. L left, R right, D dorsal, V ventral, T tongue, LG lacrimal gland, ET endoturbiniate.

lungs, which is probably attributed to probe clearance from the particular area because of its kinetics.

Fig. 2-13 displays a three dimensional mouse body segmentation (a) and 3D maximum intensity projections of the series of fluorescence images of IntegriSense (b) and AngioSense (c) with two different color maps. Fig. 2-13b clearly demonstrates the most prominent areas of IntegriSense accumulation, namely the tumors and the skeletal system of the mouse (spinal cord, skull). Especially both the left and the right tumor are precisely targeted and outlined with great contrast compared to their surrounding structures. Furthermore, a fluorescence signal of considerable intensity is emanating from the digestive system of the mouse as previously showcased in Chapter 2.4.1. on healthy, non-injected animals. The stomach and parts of the large and small intestine are clearly outlined due to the fluorescing mouse food, since the animals were not kept on a non-fluorescent diet. By comparison, the AngioSense signal intensity inside the tumors is also significant; it

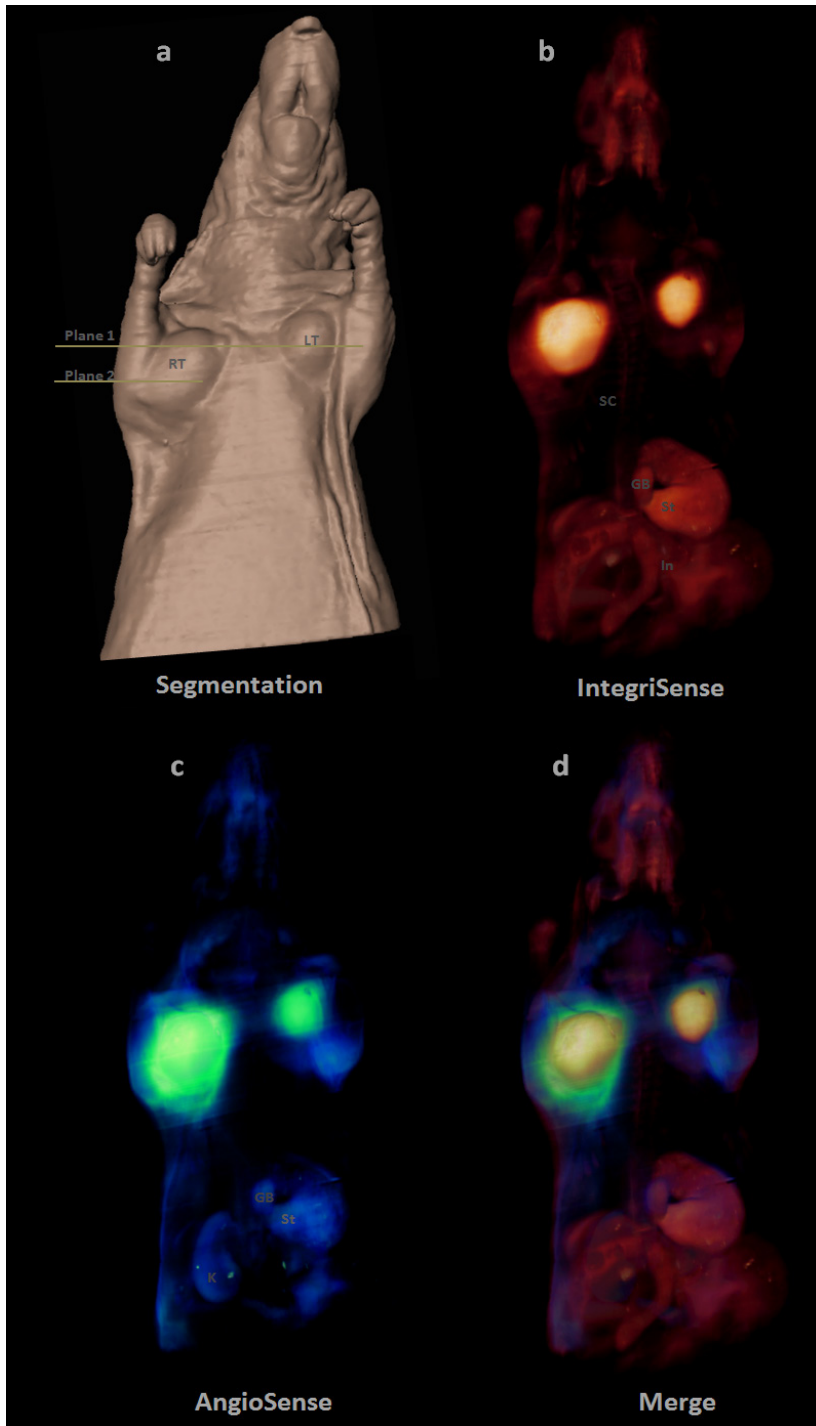


Figure 2-15. 3D maximum intensity projections showing the bio-distribution of IntegriSense (b) and AngioSense (c) and a merge of them (d) inside the whole imaged mouse volume. A segmentation of the mouse whole body (a) is also shown for anatomical comparisons between the tumors and their surroundings. RT: right tumor, LT: left tumor, SC: spinal cord, GB: gallbladder, St: stomach, In: intestine, K: kidney

Seems, however, to be more diffusely distributed around the tumors without a clear border to surrounding tissues. In this case the signal coming from the digestive track is greatly suppressed, with only the stomach being distinguishable as an area of fluorescence accumulation in the abdomen. Furthermore, a relatively low accumulation of AngioSense inside the kidneys suggests that most of the unbound probe has already been cleared from the animal 24h after its injection. Interestingly, significant fluorescence intensity in the AngioSense channel can be observed on the mouse skin, exactly below the left tumor and on the right side of the mouse. This area of unexpected fluorescence activity is notable as such unforeseen contributions would otherwise be impossible to visualize and show the potential of the high-resolution cryoslicing modality. The merge of both 3D bio-distributions in Fig. 2-13d clearly showcases the differences between the two fluorescent agents, with IntegriSense being predominantly confined inside the tumor volume and AngioSense spreading primarily through the actual tumor boundary, visualizing thus local leakage and potentially also neovasculature. Interestingly, the AngioSense 'fluorescence rim' is more clear and noticeable in the bigger tumor rather than in the smaller and the probe's distribution is extended further outside of the tumor periphery, demonstrating that leaky vasculature is increasingly developed as the tumor mass gets bigger, probably in order to balance the insufficient supply-demand equilibrium of the tumor.

Discussion

In this Chapter we showcased that using spectral differentiation our multispectral cryoslicing setup can visualize multiple fluorophores' bio-distribution inside the same animal and provide accurate localization and quantification in diseased mice. The study of dual fluorophore distribution in a xenograft mouse model most obviously demonstrates the advantages of the developed multispectral cryoslicing imaging modality. The resolving power of our imaging system to discover and indentify areas of 'unexpected' and non-obvious fluorophore accumulation is also demonstrated as we underlined a number of

areas of probe binding distant from the two tumors (skin, fatty tissue, etc.), that would otherwise remain not resolved using common planar fluorescence imaging approaches. It is arguable, thus, that the developed multispectral cryoslicing modality compared with planar fluorescence imaging can give further insights into biomarkers bio-distribution and targeting efficacy queries especially during the development of novel targeting strategies.

2.4.3 Bio-distribution in endogenous pancreatic cancer models

Introduction

Pancreatic ductal adenocarcinoma (PDAC) remains one of the most lethal malignancies in the Western world with a 5-year survival rate lower than 4%. There are few main causes for this devastating clinical course: late detection in a then often metastasized stage and insensitivity to nearly all available chemotherapies (Tempero, Plunkett et al. 2003 ; Welch and Moore 2007). Thus, curative resection is still the only curative option. In a subset of 10-15% of patients who present with resectable cancer at diagnosis, resection prolongs the overall survival up to 4 years. Important factors include size, lymph node status and resection margin involvement (Shimada, Sakamoto et al. 2006; Agarwal, Correa et al. 2008; Cartwright, Richards et al. 2008). Thus, earlier detection of resectable PDAC is one of the main goals to improve survival.

Anatomical imaging methods such as Magnetic Resonance Imaging (MRI), Computer Tomography (CT) and Ultrasound (US) provide information on tumor size, location and morphology and are the gold standard in clinical practice (Shami, Mahajan et al. 2011). However, local invasion and small volume metastatic disease are often very difficult to detect. Additionally, anatomical imaging does not provide any information about

the biological processes during cancer development and therapy that are necessary for individualized therapeutic approaches.

Alternative is offered by functional imaging modalities that are adapted to detect biological processes like tumor perfusion, oxygenation or metabolic activity. Molecular functional imaging introduced various molecular probes that target specific cancer associated molecules or processes in cancer research (Jaffer and Weissleder 2005; Neves and Brindle 2006). ¹⁸F-fluorodeoxyglucose (FDG) positron emission tomography (PET) is the currently only molecular imaging method used for detection and staging of PDAC (Lin, Barthel et al. 2011). Although it is reported that FDG-PET is superior to MRI and CT in detection of distant metastasis and recurrence, it fails to differentiate primary benign, premalignant and malignant lesions in 76% of the patients (Lin, Barthel et al. 2011) suggesting that a negative PET result does not exclude the diagnosis of PDAC.

Among molecular imaging techniques, optical imaging with fluorochrome labeled probes is especially appealing due to their good sensitivity, minimal invasiveness, easy detection, low costs and low safety concerns that often rise when using radionuclide labeled probes. Additionally, with near-infrared (NIR) fluorochromes, light attenuation and auto-fluorescence is minimized allowing good tissue penetration (Jaffer and Weissleder 2005). A wide spectrum of molecules can be labeled with fluorochromes and used simultaneously to detect distinct biological processes (Weissleder and Ntziachristos 2003; Condeelis and Weissleder 2010). Importantly, optical imaging found application in surgical practice where other molecular imaging methods are not usable. Intraoperative optical imaging is increasingly used to assist the performing surgeon in defining surgical margins and has been shown to contribute to the full removal of the neoplastic tissue and positive surgery outcome (Kossodo, Pickarski et al. 2010; Nguyen, Olson et al. 2010; Themelis, Harlaar et al. 2011).

In preclinical research, MRI, US, CT and PET have been successfully used to follow tumor development and metastasis formation in xenograft mouse models of PDAC

(Hausner, Abbey et al. 2009; Snyder, Kaushal et al. 2009; Partecke, Kaeding et al. 2011). Xenografted PDACs are also detectable with molecular optical imaging methods (Kaushal, McElroy et al. 2008; McElroy, Kaushal et al. 2008). However, xenografts have proven to be poor predictors for clinical efficacy of therapies probably due to their homogenous molecular profile and tissue composition different to the one of human tumors (Kelland 2004; Carver and Pandolfi 2006; Céspedes, Casanova et al. 2006). In contrast, genetically engineered mouse (GEM) models faithfully recapitulate human PDAC and may have a higher predictive clinical value (Hingorani, Petricoin et al. 2003; Singh and Johnson 2006). Recently, two separate studies validated MRI and US for detection and therapy evaluation in two different GEM models of PDAC (Olive, Jacobetz et al. 2009; Singh, Lima et al. 2010). Using MRI and US imaging Olive and colleagues demonstrated low vascularisation in a mouse model of endogenous PDAC and suggested that poor perfusion is one of the main causes for therapy failure. Singh and colleagues used another GEM model of PDAC and showed using US that combined chemotherapy lead to reduction in tumor burden and improvement in overall survival. The obtained information correlated well with the clinical studies especially in predicting the outcome indicating that these animals model the human response well (Singh, Lima et al. 2010). However, these imaging modalities are limited regarding detection of preneoplastic lesions or early-stage PDAC. Very recently, Eser and colleagues demonstrated a successful molecular imaging approach in a GEM model of PDAC using a cathepsin-activatable probe for diagnosis of preneoplastic lesions (Eser, Messer et al. 2011).

In this study, we validate $\alpha V\beta 3$ integrin as a target for visualization of preneoplastic lesions and PDAC in GEM models via optical imaging. Integrin $\alpha V\beta 3$ belongs to the integrin family of cell surface receptors expressed on activated endothelial cells of new sprouting vessels in the tumor and on tumor cells in many different cancers and has been shown to be overexpressed in primary human PDACs. It has been implicated as a key player in angiogenesis and metastasis in various cancers and was shown to be especially relevant for the metastatic spread of PDAC to the lymph nodes (Hood and Cheresch 2002; Hosotani,

Kawaguchi et al. 2002; Beer and Schwaiger 2008; Desgrosellier and Cheresch 2010). Its role in cancer and the widespread expression make it an important molecular imaging target. We report on increased expression of $\alpha\text{V}\beta\text{3}$ integrin in endogenous murine PDAC and demonstrate by in vivo and ex vivo optical imaging that preneoplastic lesions and PDAC can be visualized with $\alpha\text{V}\beta\text{3}$ targetable agents.

Studied animals

As pancreatic cancer is a complex disease that develops stepwise and pancreatic tissue displays dramatic changes in this process, we introduced two genetically modified animal models into our study. To evaluate the $\alpha\text{V}\beta\text{3}$ integrin as a target for pancreatic cancer imaging, we used multiple animals from different cohorts: mice with normal pancreatic tissue (*wild-type; wt*), with preneoplastic PanIN lesions (*Ptf1a^{+Cre};Kras^{+LSL-G12D}; CK*) and invasive PDAC (*Ptf1a^{+Cre};Kras^{+LSL-G12D};p53^{LoxP/LoxP}; CKP*). These animal models describe morphological changes in the pancreas during cancer development and provide staging of pancreatic carcinoma in humans and in mice.

Pancreas specific activation of oncogenic KrasG12D in CK mice leads to development of preneoplastic lesions that recapitulate the full spectrum of human pancreatic intraepithelial neoplasia (PanIN), the most common precursors to PDAC (Fig. 1B) and are an excellent tool for modeling the pre-cancer state of pancreas, rich in preneoplastic lesions that are putative precursors to PDAC, but without real tumor. Only at advanced, PDAC develops in a subset of animals (Hingorani, Petricoin et al. 2003). To model PDAC, we introduced into the study animals with oncogenic KrasG12D and concomitant deletion of p53 (CKP). These mice develop well-differentiated pancreatic adenocarcinoma with dense stroma already at 6-8 weeks of age (Fig. 1B), exhibit 100% tumor penetration and develop tumors that are always histologically graded as adenocarcinoma (Bardeesy, Aguirre et al. 2006). Our combined multi-model approach, compared to xenograft models, not only utilizes an endogenous mouse model for PDAC, it also takes into account

intermediate stages of the disease, proposing, thus, a more realistic representation of the various stages of disease progression.

Imaging procedures

All animals used in this study (n=17, of which 2 wildtype, 7 CK and 8 CKP mice) were imaged by T2-weighted MRI on a 1.5T clinical scanner (Achieva 1.5T, Philips Medical Systems, Best, The Netherlands) and directly afterwards were administered with IntegriSense 680 (Perkin Elmer, Waltham, MA) (2nmol) via a tail vein bolus injection. The fluorescent probe was allowed to circulate for 24h and at that point the mice were anaesthetized using a 2% isoflurane-oxygen mixture. A surgical incision exposed the abdominal cavity to our intra-operative imaging setup (described in Section 3.2) that captured images of the exposed pancreas and its surroundings, simulating in this way the intra-operative imaging procedure. These images were used to evaluate the tumor border delineation properties of the targeted contrast agent for every different mouse model. Directly afterwards, the animals were euthanized by an intra-peritoneal injection of ketamine and were quickly frozen in sealed dry ice containers. The frozen animals were later dissected so that only the abdominal area around the pancreas could be embedded in OCT-India ink mixture, sectioned and imaged with the developed cryoslicer modality (Sarantopoulos, Themelis et al. 2010). Color and fluorescence images were captured every 200 μ m and were used to visualize volumetrically and in detail all the pancreas surrounding tissues and to compare the fluorescence distribution with the equivalent MRI cross-sectional images under the same geometry.

Results

α V β 3 expression is increased in precursor lesions and PDAC

To evaluate if $\alpha V\beta 3$ integrin would be a good target for optical imaging of PDAC, we analyzed the expression of αV and $\beta 3$ integrin subunits in mice with normal pancreatic tissue, preneoplastic PanIN lesions and invasive. Western Blot analysis demonstrated an increase in expression of both αV and $\beta 3$ protein subunits in PDAC compared to wt and PanINs (Figure 2-14A). Immunohistochemistry for the $\beta 3$ subunit showed that in wildtype pancreas $\beta 3$ expression is limited to occasional blood vessels while no staining was observed in the acinar or ductal compartments (Figure 2-14B-a). In PanINs of CK mice, an increase in $\beta 3$ staining was observed. Cells positive for $\beta 3$ were found in PanINs and duct-like lesions and occasionally in the surrounding stroma (Figure 2-14B-b, d).

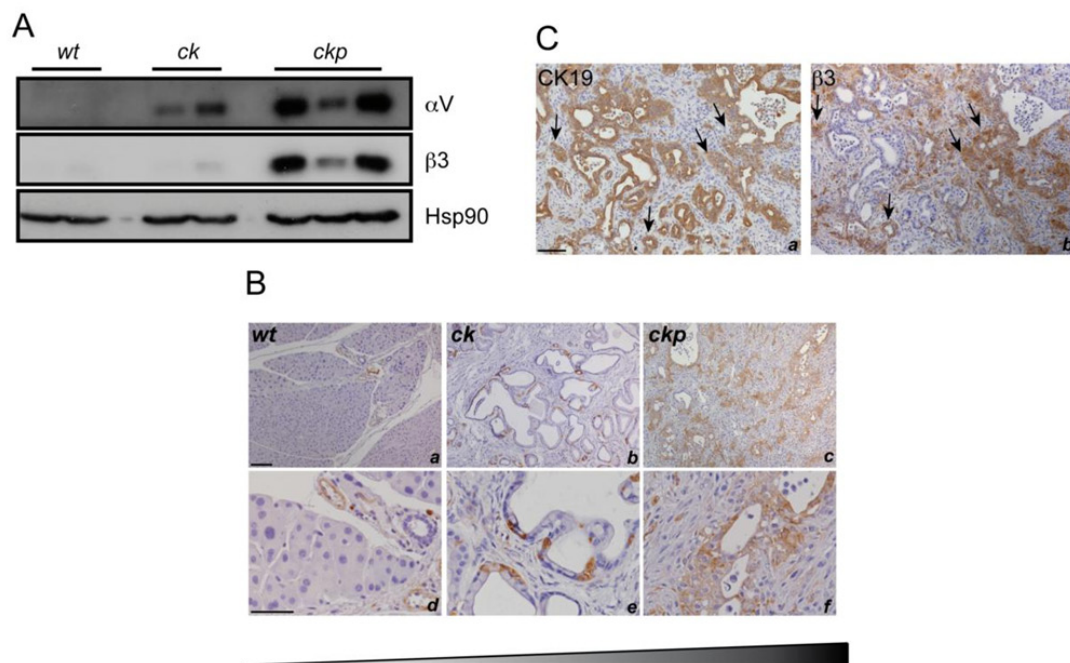


Figure 2-16. A) Western blot analysis demonstrating increase in αV and $\beta 3$ expression in PDAC from CKP animals compared to preneoplastic tissue from CK animals and healthy tissue from wildtype animals. HSP90 expression demonstrates equal loading in all lanes. B) Immunohistochemistry for $\beta 3$ integrin demonstrating no expression in the wildtype exocrine tissue (a), low patchy expression in pancreatic tissue from CK animals (b, d) and high expression in CKP PDAC (c,e). High magnification image (d) shows $\beta 3$ expression in ductal lesions and PanINs in CK pancreata. C) Immunohistochemistry for (a) CK19 and (b) $\beta 3$ on consecutive paraffin sections of CKP tumors. A partial overlapping pattern between both markers was observed (arrows).

Scale bars: 50 μ m.

In CKP mice with PDAC, a dramatic increase in staining signals for the $\beta 3$ subunit was observed. $\beta 3$ positive cells were numerous and scattered throughout the tumor and could be attributed to malignant, invasive cells but also to the surrounding reactive stroma (Figure 2-14B).

To determine whether the $\beta 3$ positive cells in tumor tissue were of ductal (epithelial) origin, we performed immunohistochemistry on consecutive paraffin sections for cytokeratin 19 (CK19) and $\beta 3$. As expected, both proteins demonstrated membranous localization. Here, the staining pattern for $\beta 3$ and CK19 was partially overlapping. Some areas positive for $\beta 3$ were also positive for CK19 while some of the $\beta 3$ positive cells were negative for CK19 (Figure 2-14C). Similar results were observed with double immunofluorescence staining for $\beta 3$ and CK19 with membrane-expression pattern for both proteins and only a partial overlap between $\beta 3$ and CK19 fluorescent signals. Some of the $\beta 3$ positive cells were also positive for CK19 but some cells were positive for $\beta 3$ staining and negative for CK19 (image not shown). Additionally, as $\alpha V\beta 3$ is expressed in newly sprouting vessels in the tumor (Hood 2002, Desgroselier 2010), we investigated whether increased $\beta 3$ positivity can be attributed to blood vessels in the tumors. CD31 is a marker of endothelial cells and its staining pattern differed significantly from staining pattern of $\beta 3$ integrin on consecutive paraffin sections of CKP cancers (image not shown). By direct comparison, some $\beta 3$ immunoreactivity could be attributed to blood vessels but the majority of $\beta 3$ positive cells were rather not the endothelial cells of vessels.

Intra-operative planar *in vivo* imaging of IntegriSense faithfully identifies PDAC

As $\beta 3$ expression was highly increased in murine tumor tissue compared to healthy tissue and preneoplastic lesions, we assumed that $\beta 3$ would be a good target molecule for optical imaging of PDAC. For this purpose, IntegriSense 680, a small non-peptide near-infrared (NIR) labeled molecule that binds specifically to $\alpha V\beta 3$ integrin (Perkin Elmer, Waltham, MA) was used for optical imaging. At 24 hours post-injection, planar, epi-

illumination fluorescence images of the open abdomen were taken. Histopathological analysis was carried-out post-mortem for every animal.

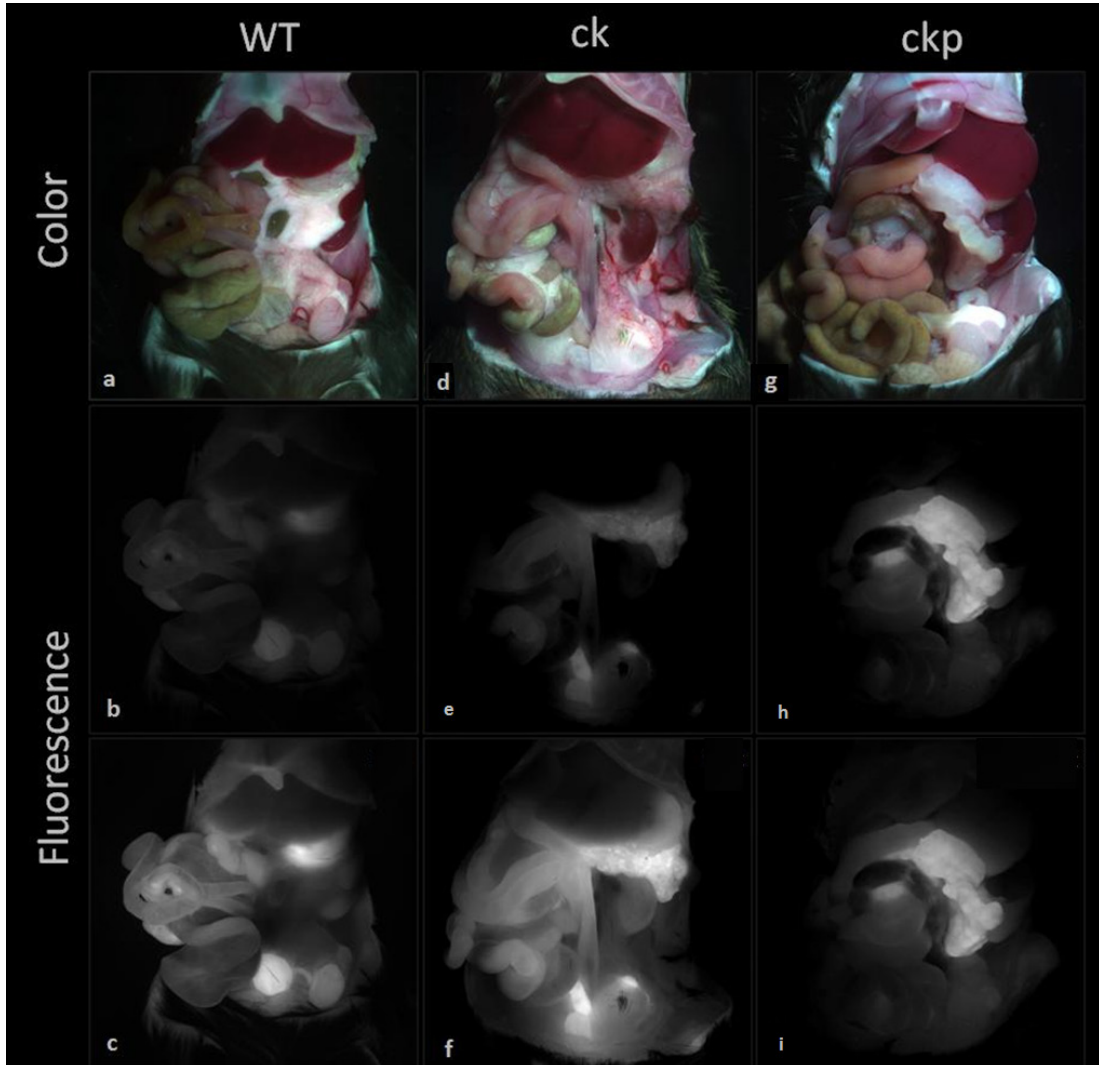


Figure 2-17. Representative planar whole body color (a, d, g), normalized fluorescence (b, e, h) and original fluorescence (c, f, i) images of wildtype (WT), CK and CKP animals. The planar fluorescence images from different animals are presented both in their original color scale/dynamic range (c, f, i) and normalized (b, e, h) to the fluorescence intensity of the intestine (using a common color scale) for direct comparison of the fluorescence contrast among animals. Intra-operative optical fluorescent imaging differentiates very well between healthy, CK and CKP pancreas: strong equally distributed IntegriSense 680 fluorescence signals are detectable from tumor surface in CKP animals (h, i), spots of fluorescence in CK animals (e, f) and no signals from wildtype pancreata (b, c).

In Fig. 2-15, representative color autopsy (a, d, g) and fluorescence images are shown. Figures 2-15b, e, h are normalized in the same color map for direct comparison, while Fig. 2-15c, f, i have different color maps for clearer visualization. In wildtype animals, no fluorescence was detectable at the surface of healthy pancreas suggesting no specific accumulation of IntegriSense 680 in the normal pancreatic tissue (Fig. 2-15b,c). This result corresponded well with immunohistochemistry showing low $\beta 3$ protein expression levels in wt pancreas (Figure 2-14B). In CK animals, the pancreas was well visualized via optical imaging. Patchy fluorescence pattern with spots of IntegriSense signals was noticed suggesting probe accumulation in defined places in pancreas (Fig. 2-15e, f). In CKP animals, PDAC were remarkably well visualized with intra-operative imaging showing strong and very specific fluorescence signals on tumor surface (Fig. 2-15h, i). Fluorescent contrast to the adjacent tissues was very strong and high NIR fluorescence signals were detected only from the tumor surface indicating that IntegriSense accumulated specifically in the tumor. Also, tumor borders were demarcated very well and delineation of the tumor to surrounding organs was easily done. Examination of other exposed organs showed occasional weak fluorescence signals coming from the gut, stomach, fat pads, urinary bladder and ovaries in females.

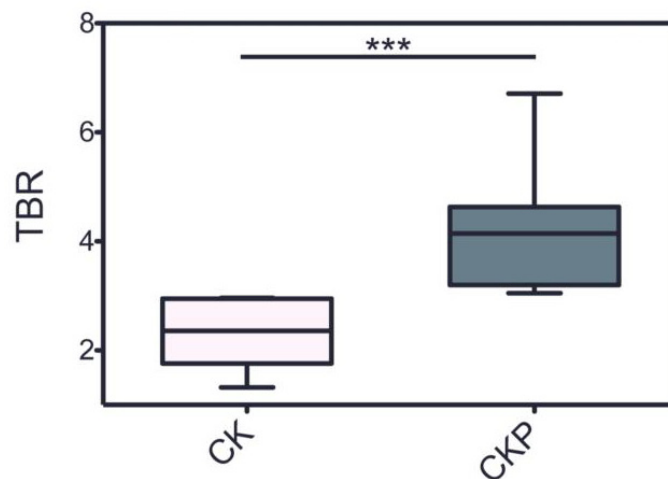


Figure 2-18. Relative fluorescence tumor to background (TBR) ratios for CK and CKP animals. Higher values were determined for tumors of CKP animals compared to pancreata of CK animals.

For CK and CKP animals, fluorescence intensity ratios between tumor/pancreas and surrounding tissue (tumor to background, TBR) are calculated with respect to the fluorescence intensity of the intestine (“background”), which is the prominent and most intense fluorescing structure at the abdominal area. The fluorescence signal of the intestine is caused primarily by the ingredients of the mouse diet and, to a lesser extent in this spectral range, by tissue autofluorescence and therefore can be considered as constant throughout different experiments. This ratio was always clearly higher for CKP tumors than for CK pancreata (Fig. 2-16), suggesting higher specific accumulation of IntegriSense in the tumor.

***Ex vivo* multispectral cryoslicing validates *in vivo* intra-operative IntegriSense imaging**

Intra-operative epi-illumination *in vivo* imaging detects fluorescence signals primarily from tissue surface but does not represent the real fluorophore bio-distribution inside the tissue. To evaluate intra-tissue probe penetration, we employed the developed multispectral cryoslicing system. Cryosectioning enables direct comparison of probe accumulation in the tissue volumes of interest and other surrounding organs. As in intra-operative imaging no specific fluorescence was detected at the surface of healthy pancreas, we excluded wt mice from cryoslicing analysis. CK and CKP mice were whole-mount frozen and cryosliced and fluorescence patterns and intensities were compared. In addition, fluorescent images were compared to axial T2w-MRI images from corresponding animals. In Fig. 2-17 representative cryoslicer color, fluorescent and equivalent axial T2w-MRI images are shown. Histological analysis (not shown) for all animals confirmed presence of PanIN preneoplastic lesions typically found in 6-12 months old CK mice and presence of adenocarcinoma in CKP animals.

In CK animals, the fluorescence pattern inside the tumor corresponded very well to the pattern observed at the tumor borders. Pancreata were well visualized and delineated

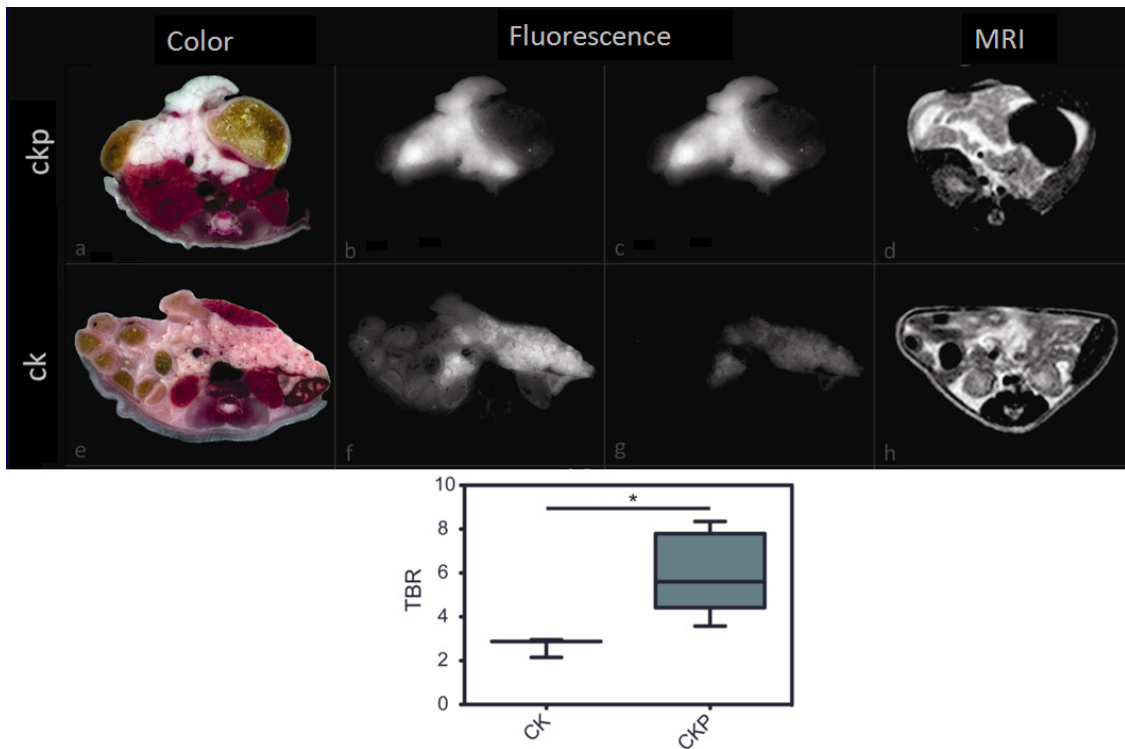


Figure 2-19. Representative cross-sectional (axial) cryoslicer images: color (a,e) , original fluorescence (b,f), normalized fluorescence (c,g) and corresponding T2w-MRI (d,h) images for CK and CKP animals. Patchy fluorescence pattern was observed in cross sections of CK pancreas while more equally distributed fluorescence was observed in cross sections of PDAC. Axial T2w-MRI and fluorescence images correlated very well but delineation of tumor borders was more clearly seen on fluorescence images. Histological analysis showed typical tissue composition for both models. In the lower part the TBR ratios that were calculated from the cryoslicer images are shown. Higher values were determined for PDAC of CKP animals than for pancreata of CK animals.

from the surrounding tissue. Fluorescence was not equally distributed through the tissue but demonstrated a rather spotty pattern as in intra-operative images. This was also in good correlation with patchy pattern of $\beta 3$ expression demonstrated by immunohistochemistry in CK pancreata (Fig. 2-14B). In tumor animals, cryosectioning revealed that IntegriSense penetrated very well into PDAC. Strong and specific fluorescence signals were observed throughout the tumor with little or no background signals from most of the surrounding tissue. The high fluorescence tumor to background contrast correlated very well high expression of $\beta 3$ protein in CKP tumor samples demonstrated by immunohistochemistry and Western blot. Fluorescence was detected in all parts of the

tumor, independently of its location or size. Fluorescence accumulation at the tumor rims that could account for false positive epi-illumination signals from tumor surface in intraoperative imaging was not observed. IntegriSense accumulated well even in the small tumor lobes. Generally, axial fluorescent images of the tumor correlated well with the axial T2w-MR images. Tumors appeared hyperintense compared to the liver and were easy to recognize. However, in some parts of the body, hyperintense T2w signals from the tumor were comparable to hyperintense T2w signals of the gut making delineation of tumor to gut borders very difficult. In fluorescence images, this demarcation of tumor borders was dramatically eased. All parts of the tumor were clearly distinguishable from the surrounding organs including gut. Some low fluorescence was observable in certain parts of the gut probably due to potential specific or unspecific probe accumulation in the gut and its walls and food autofluorescence. However, fluorescence signals of the tumor were always stronger than signals from the gut. Measurements of signal to background ratios from fluorescent images of CK pancreata and CKP cancers confirmed the observations from intraoperative images. Ratios were always higher for CKP tumor tissue than for CK tissue with preneoplastic lesions suggesting a higher accumulation of probe in the cancer.

Based on the multiple cross-sectional cryoslicer images, volumetric rendering of 3D fluorescence distributions were created using Amira and its built-in maximum intensity projection algorithm. Once again, the intricate details of the pancreatic tissue as well as different contrast enhancements of Integrisense among the different animal models are evident. As shown in Fig. 2-18 (right side), only the shape of the tumor can be distinguished, as there is barely any comparable fluorescence intensity originating from the PDAC surrounding structures. This rendering demonstrates the high Integrisense accumulation in this GEM model of PDAC. Fig. 2-18 (left side) displays the patchy nature of fluorescence signal emanating from the CK pancreas. Although the pancreatic tissue is distinguishable, its fluorescent contrast is reduced compared to the cancer in PDAC mice.

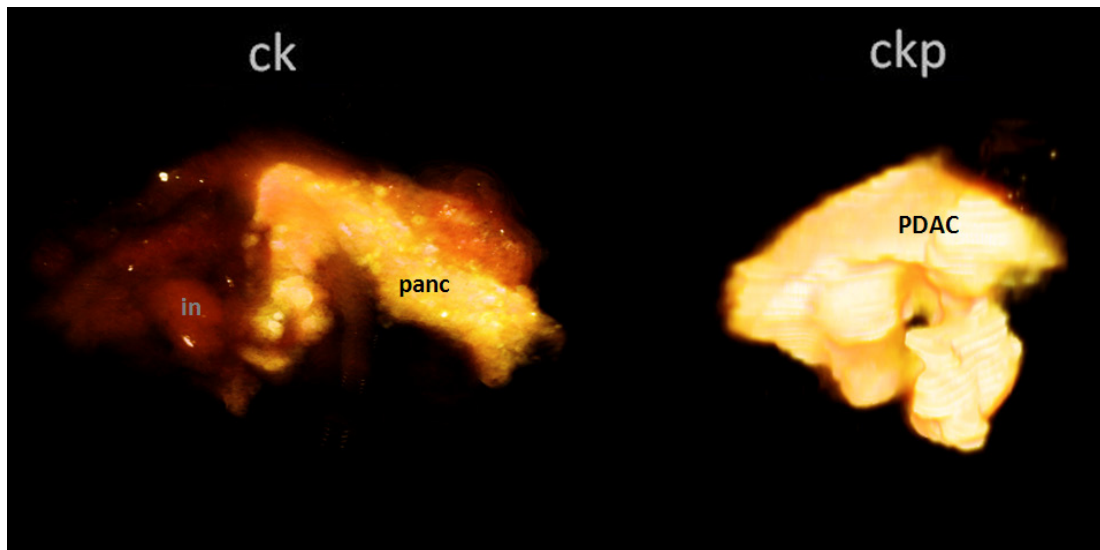


Figure 2-20. Volumetric rendering of the three-dimensional fluorescence distributions for CK and CKP animals. Inherent details of pancreatic tissue as well as different contrast of IntegriSense between the animal models are evident. The shape of the tumor can be distinguished, while no surrounding structures are visible; this demonstrates the high IntegriSense accumulation in the GEM model of PDAC. CK pancreas demonstrates a patchy fluorescence, with reduced contrast compared to CKP mice.

Discussion

Although still irreplaceable for diagnosis of PDAC in clinical practice, anatomical imaging methods suffer from poor sensitivity for small masses and often miss early developing cancer (Shami, Mahajan et al. 2011). Until now, detection of PanIN lesions in humans is not possible. Additionally, anatomical imaging has limited application spectrum: it does not provide any kind of functional information about the tumors proliferative capacity, angiogenesis, metastasis or any other tumor related process. Furthermore, translation of the MRI, CT or US images to the operation field is a major challenge for the surgeon.

Functional molecular imaging technologies expanded into the PDAC research after introduction of GEM models (Olive, Jacobetz et al. 2009; Eser, Messer et al. 2011). Molecular signatures in PDACs from GEM mice are similar to those in human cancers

(Wagner, Greten et al. 2001; Hingorani, Petricoin et al. 2003; Hingorani, Wang et al. 2005; Bardeesy, Aguirre et al. 2006; Siveke, Einwächter et al. 2007), allowing identification of novel target molecules for molecular imaging of cancers. One such molecule of known importance for cancer angiogenesis and metastasis is integrin $\alpha V\beta 3$ (Hood and Cheresch 2002). Because of its cancer restricted expression and functional importance, $\alpha V\beta 3$ is a very attractive molecular imaging target. Many different radiolabeled RGD molecules that target $\alpha V\beta 3$ are in preclinical and clinical use for detection of angiogenesis and tumor load via PET in various cancers. However, RGD-PET is burdened by low sensitivity, high costs and use of ionizing radiation. Moreover, RGD-PET has never been used in PDAC preclinical or clinical practice. Probable reason for this is that only very recently the importance of $\alpha V\beta 3$ integrin in PDAC biology has been recognized. In 2010, Desgrosellier and colleagues demonstrated that $\alpha V\beta 3$ expressed in pancreatic carcinoma cells enhanced anchorage-independent tumor growth and increased lymph node metastasis. Additionally it was shown that 58% of human PDACs express $\alpha V\beta 3$ and this is associated with lymph node metastasis. This work suggested that $\alpha V\beta 3$ might be an interesting target for molecular imaging of PDAC.

In the present study, we focused our attention on endogenous PDAC in GEMs and potentials of molecular optical and PET imaging of $\alpha V\beta 3$ integrin in these models. Optical and PET imaging were chosen for 2 main reasons: optical imaging is a new emerging technology with better sensitivity than traditional anatomical imaging techniques and large application spectrum but is largely in the preclinical phase; on the contrary, PET has entered the clinic several years ago and is in everyday practice in cancer patients.

In good correlation with the human data (Desgrosellier and Cheresch 2010), we found an increased expression of $\alpha V\beta 3$ protein in PDAC from CKP mice by Western blot and immunohistochemical analysis. Most of the $\beta 3$ expression could be attributed to malignant cells or reactive stroma and only partially to endothelial cells of vessels indicating that by targeting $\alpha V\beta 3$, one is rather detecting the PDAC itself and not the angiogenesis in it.

For optical imaging, we used Integrisense680, a $\alpha V\beta 3$ binding NIR fluorescent commercially available (Perkin Elmer, Waltham, MA) molecule, which application does not demand exhausting optimization or labeling and has been previously used for detection of $\alpha V\beta 3$ positive cancers (Kossodo, Pickarski et al. 2010). Two different optical imaging procedures demonstrated that Integrisense is able to faithfully identify the tumor in GEM mice: intraoperative imaging of abdomen in CKP animals showed specific fluorescence signals at the tumor surface and multispectral cryoslicing demonstrated good penetration and specific distribution inside the tumor. In comparison to T2w MRI as traditionally used anatomical imaging method, molecular optical imaging of $\alpha V\beta 3$ had at least two advantages. First, Integrisense was able to differentiate between healthy pancreas in wildtype pancreatic tissue and preneoplastic lesions in CK animals and fully developed cancer in CKP animals. Not only that measured fluorescence intensities were lower in pancreas of CK animals than in CKP animals, but also the fluorescence pattern differed: spots of fluorescence in CK pancreata versus strong, equally distributed fluorescence in CKP tumors. Second, definition of tumor borders in CKP mice was dramatically easier with optical than with T2w-MR imaging.

Importantly, as Integrisense was able to detect already the preneoplastic lesions, optical image guided explorative surgery in high risk patients may be offered as an option for early detection of cancer. T2w-MRI was not suitable for detection of preoplastic pancreas in CK animals and this tissue was easily mistaken for healthy one. Although one can argue that sensitivity of 1,5T MR scanner is perhaps low and nowadays scanners with 17T field strength are available, 1,5T is still the most commonly available clinical scanner where patients are routinely examined. In comparison to this scanner, intraoperative optical imaging was more powerful in identification of preneoplastic pancreas and definition of tumor borders.

$\alpha V\beta 3$ expression has been directly correlated with the metastatic potential of the tumor and it is even suggested to be a marker of metastatic cells in these tumors. Although metastases usually do not occur in the CKP mouse model due to fast tumor progression

(Bardeesy, Aguirre et al. 2006), one can envisage that Integrisense would be a good option for intraoperative optical detection of $\alpha V\beta 3$ positive metastasis in humans.

In conclusion, we provide evidence for $\alpha V\beta 3$ as a promising target in PDAC. The data provided for optical and PET imaging provide a strong basis for novel approaches for early detection, tumor imaging and targeted therapies in this still fatal disease.

2.4.4 Bio-distribution using spectral fitting

Introduction

The term 'spectral unmixing' refers to a family of signal/image processing methods that are used to decompose spectrally overlapping signals/objects of different intensities after processing on a per pixel basis. Spectral fitting is the simplest form of spectral unmixing and refers to the procedure of finding the component (a series of pixels) of an image that best fits a reference spectrum. Usually the *a priori* known excitation or emission curve of a fluorophore is used as reference for the identification of fluorescing tissues inside an animal. Spectral fitting can be applied using the existing cryoslicer hardware thanks to the incorporation of multi-position filter wheels that enable the mounting of multiple excitation and/or emission filters. The acquisition and processing of spectral images is a unique ability of the cryoslicing setup that enables to resolve fluorescent signals from tissues not only based on their intensity, but also on their spectral signature. In this way, contrast between tissues can be extracted not only on a 'target-to-background' basis (intensity-wise) but also in terms of spectral differentiation. Fluorescence contributions of low or moderate intensity that would otherwise be masked by other parasitic signals can be now successfully identified and accurately distinguished, increasing, thus, the detection sensitivity of the method.

An application of spectral unmixing in the field of optical fluorescence imaging is the differentiation of disease-specific low intensity areas from the disease-unspecific surrounding auto-fluorescence (Levenson and Mansfield 2006). Tissue auto-fluorescence has a strong intensity and broad emission spectrum covering the majority of the visible light spectrum, especially when excited with ultraviolet or blue light. As a result, it is often difficult to image fluorophores in the visible region without the presence of significant auto-fluorescence background. In these cases, spectral unmixing is especially beneficial, as it can retrieve the fluorescent signals of interest (for instance deriving from fluorescent protein-expressing cancer cells) based on their spectral signatures and not on their intensity.

Studied animals

We evaluated the performance of spectral fitting for cryoslicer volumes using an animal model of leukemia, where EGFP (enhanced green fluorescent protein) and luciferase labelled cancer cells were injected in a mouse model. Human ALL cells were obtained from pediatric patients and NSG mice (NOD-scid IL2R γ manull; The Jackson Laboratory) mice were maintained as described (Hoefig et al, paper submitted). After the development of leukemic disease, patient-derived leukemia cells were isolated from mouse spleens, purified and transduced overnight in a 12-well plate with extGLuc virus at a multiplicity of infection of 1 transduction unit / cell in the presence of 3 μ g/ml Polybren (Sigma) in RPMI medium (Invitrogen) supplemented with 20% FCS (Biocrom AG), 1% Glutamine (Gibco), 1% Pen-Strep (Gibco), 1% Gentamicin (Biocrom AG), 0,1% Insulin-Transferrin-Selenium (Gibco), 50 μ M α -Thioglycerol (Sigma) and 1mM Sodium Pyruvate (Sigma). After extensive washing in phosphate-buffered saline (PBS) plus 2% FCS, about 1-3 million cells per mouse were injected intravenously into recipient NSG mice.

The leukemia cells were primarily accumulated in the skeletal system (spinal cord and limbs) and the spleen, but were also suspected for aggressive metastatic behavior throughout the mouse body. We imaged different whole body cryosliced animals that

represented three distinct stages of the disease progression (early, medium and late) in order to identify the overall system sensitivity and visualize tumor growth at different time points. All mice were dissected at the lung area, embedded in OCT-India ink mixture and imaged every 125 μ m.

Results

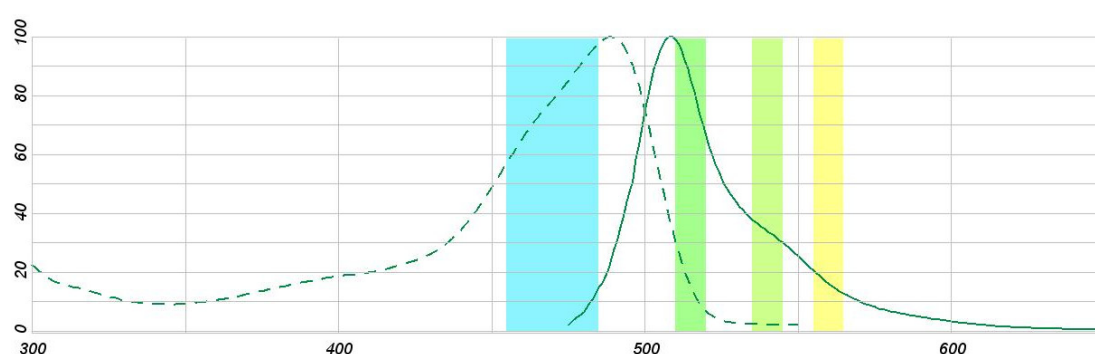


Figure 2-21. EGFP excitation (dotted line) and emission (solid line) spectra

(<http://www.invitrogen.com/site/us/en/home/support/Research-Tools/Fluorescence-SpectraViewer.html?fileId1=EGFPpH7>).

Blue highlight denotes the excitation filter (30nm bandwidth), while the 3 fluorescence filters utilized to capture the multispectral fluorescence emission are displayed with green and yellow lines (10nm bandwidth each).

Fig. 2-19 displays the excitation and emission spectra of the EGFP protein that was used in the experiments. A narrow band pass filter at 470nm with a 30nm bandwidth was chosen for excitation at the peak EGFP excitation (488nm), while three 10nm-wide band pass filters captured fluorescence images at 515nm (peak EGFP emission), 540nm and 560nm (all filters from Chroma, Rockingham, VT, USA). The three spectral measurements at the emission curve of EGFP were used in order to distinguish the areas (pixels) of the fluorescence images that featured this steep decline and discriminate them for the other measured spectra (auto-fluorescence, food fluorescence, etc). We chose to use image derived spectral components as a reference in order to fit our series of images rather than use the theoretical emission spectrum of EGFP, as this would better describe the real situation and provide an adequate decomposition of the values. For all the series of images,

the exposure times were normalized and the dark current counts were subtracted before the spectral fitting processing step.

Fig. 2-20 depicts a cross-section at the mouse abdomen of an animal at the late stage of the disease, displaying the spinal cord, spleen, kidneys and intestine. The top row (Fig. 2-20a-c) shows the fluorescence images captured at different points of the EGFP emission spectrum, namely at 515nm, 540nm and 560nm. The strongest signals in all of them are originating from the intestinal tract and

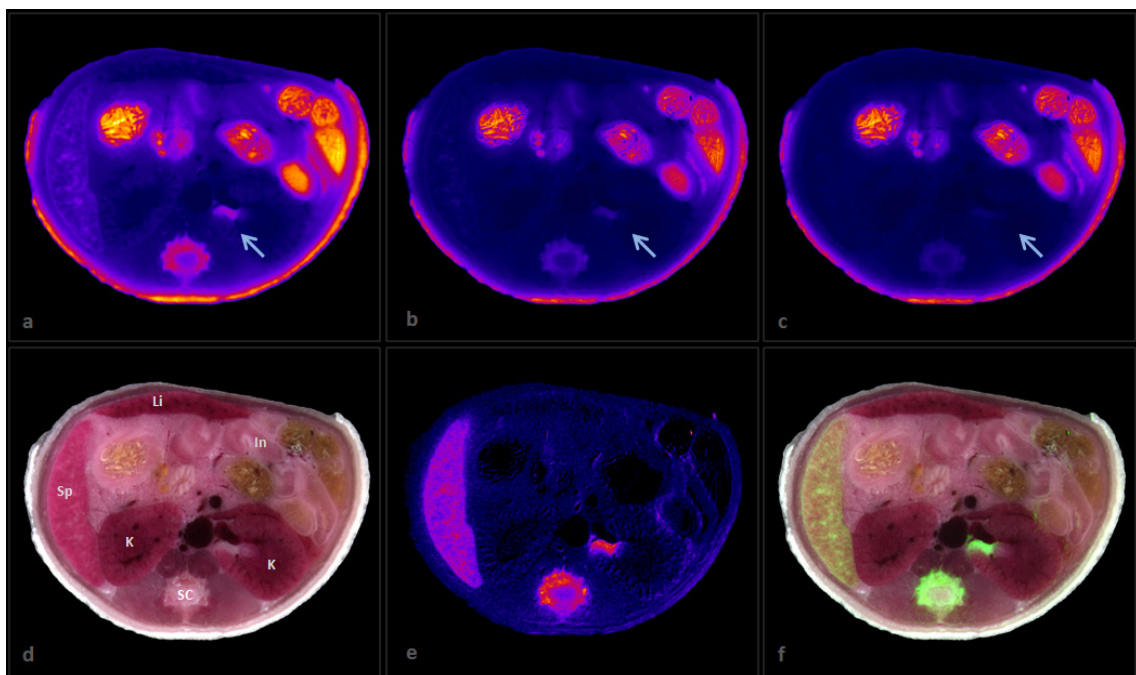


Figure 2-22. A cross-sectional cryoslicer image depicting the kidneys, spleen and the intestine. The top row (a-c) displays the fluorescence images in false color captured with the 515nm, 540nm and 560nm narrow band pass filters, while (d) is the color composite. The result of the spectral fitting (e) is showing in false color the areas that were decomposed due to their spectral signature. It is interesting to note how metastatic signals, like the one coming from the right kidney, can be easily resolved with the multispectral method. The decomposed signal is then superimposed in the green channel of the color reflectance image of the sample (f). SC: spinal cord, K: kidney, Sp: spleen, In: intestine, Li: liver.

from the mouse skin and are attributed to the fluorescent diet and auto-fluorescence respectively. As expected the fluorescence intensity of the spinal cord and the spleen shows a gradual decline through the images. Interestingly, though, the same pattern is also visible

around a blood vessel that supplies the right kidney (arrow). Indeed, after the spectral fitting (Fig. 2-20e) all these areas are resolved and precisely identified as EGFP-positive. For visualization purpose, we overlaid the spectral fitting result on the color image of the sample to illustrate the exact localization of the signals. The activity inside the kidney is attributed to the highly metastatic nature of the mouse model and was not identified prior to the cryo-imaging procedure.

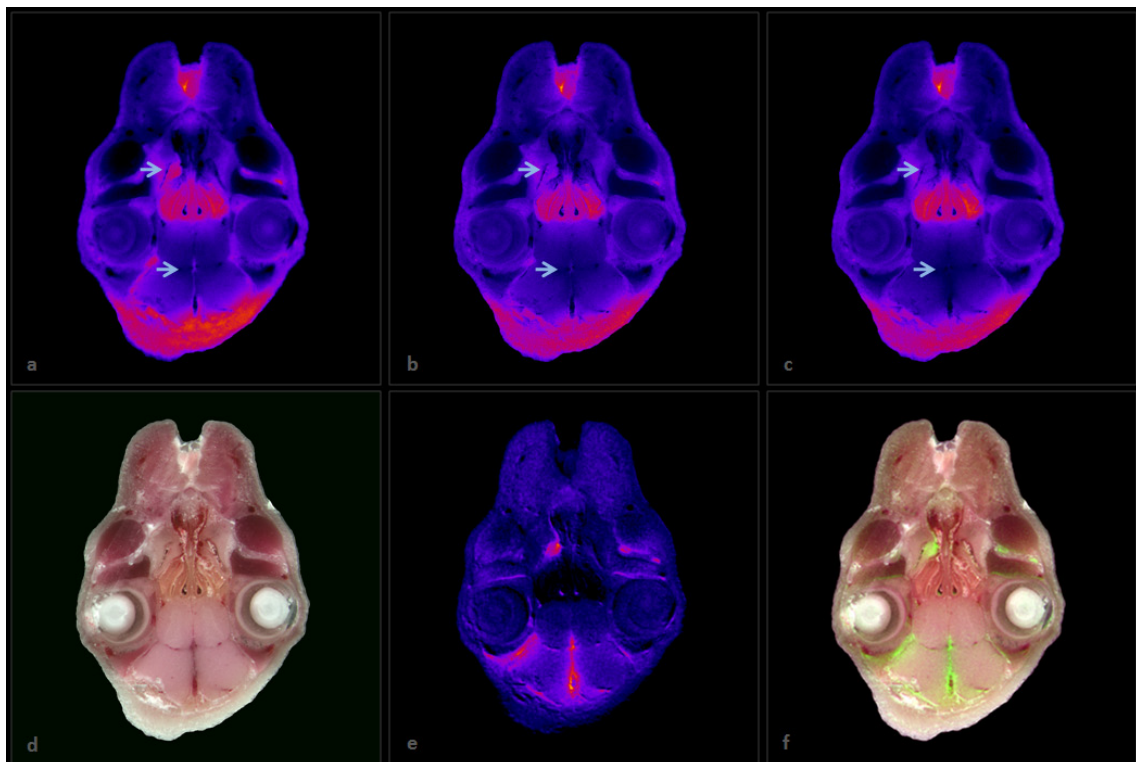


Figure 2-23. Cross-sectional cryoslicer image depict the mouse brain and eyes. The top row (a-c) displays the fluorescence images in false color captured with the 515nm, 540nm and 560nm narrow band pass filters, while (d) is the color composite. The result of the spectral fitting (e) shows metastatic activity in fine structures of the skull and inside the brain that are close to indiscernible even in the fluorescence image at the protein's peak emission (a) . The decomposed signal is then superimposed in the green channel of the color reflectance image of the sample (f). B: brain, E: eye, ET: endoturbinate.

Fig. 2-21 displays an additional cross-section through the brain of the previous mouse. In this case, strong fluorescence signals from parts of the skull-overlying skin, the endoturbinate and the mouth are dominant. Otherwise, there are hardly any areas in the images that can be identified to follow the steep decline pattern of EGFP. Only after the

spectral unmixing (Fig. 2-21e) can one look back at the initial spectral images (a-c) and identify the resolved structures as such of declining intensity (arrows). Interestingly, parts of the skull but also a fairly large area inside the brain are found to contain metastases

Fig. 2-22 shows 3D maximum intensity projection reconstructions at the abdominal area. Fluorescence volumes at the EGFP peak emission (515nm) (a, c) are compared with the result of the spectral fitting processing (b, d). Evidently, the fluorescing cancer cells accumulated in the spinal cord and spleen,

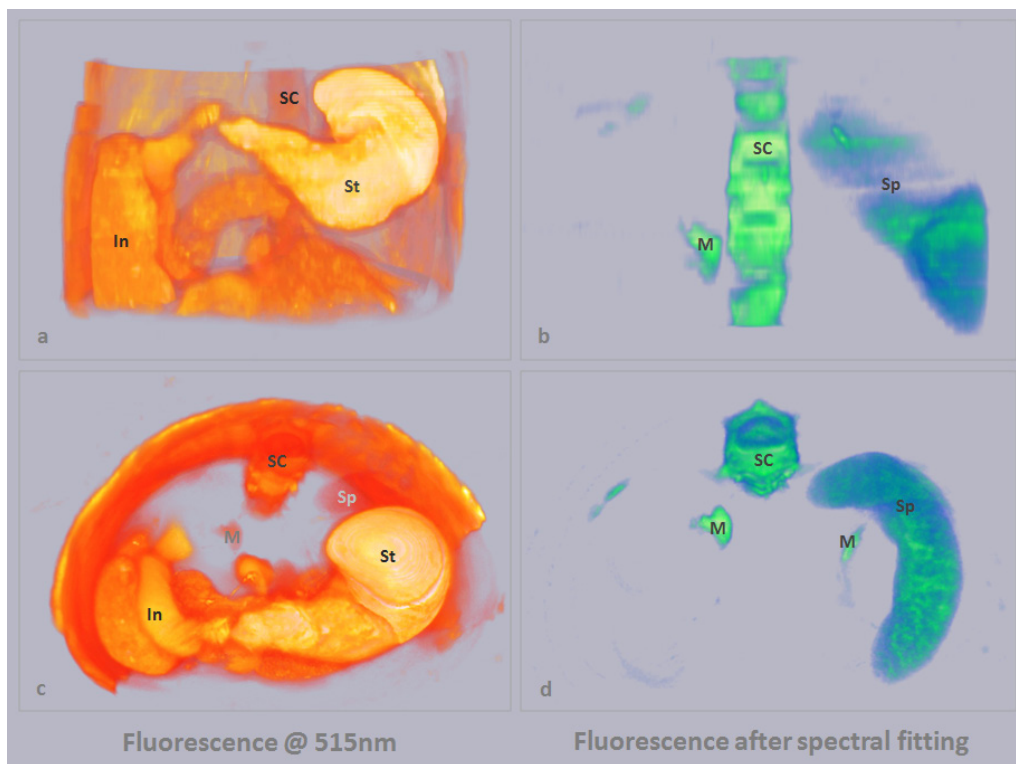


Figure 2-24. 3D reconstructions of the abdominal area using the fluorescence images acquired at the peak emission wavelength of EGFP (515nm) (left: a, c) and using the spectral unmixed data (right: b, d). SC: spinal cord, St: stomach, Sp: spleen, In: intestine, M: metastatic foci.

featuring a low/moderate fluorescence intensity, cannot be distinguished due to the increased surrounding auto-fluorescence (skin) and animal diet fluorescence levels (gastrointestinal tract). In contrast, spectral fitting takes into account the spectral signature

of the diseased tissues and manages to decompose not only the areas of accumulated cells (spinal cord and spleen) but also resolve small metastatic foci.

Spectral fitting could not decompose any areas of EGFP expression in earlier stages of the disease and therefore these results can only be thought of as preliminary. The reason is that the fluorescent intensity from diseased areas in earlier leukemia development stages is so very low and, at the same time, the food fluorescence so high that the EGFP signal at the peak fluorescence emission drops below the camera dark noise level and, therefore, cannot be captured by the imaging system. As observed in bioluminescence images (not shown), the signal intensity (and therefore also the number of fluorescing cells) strongly decreases at the early time points of leukemia development. Future improvements are needed to reduce these effects; namely the use of special non-fluorescing mouse nutrition and the implementation of a CCD sensor with higher dynamic range could reduce the parasitical fluorescence signal and further boost the resolving power of the method.

Overall, these preliminary experiments showcased that multispectral cryoslicing is indeed able to identify fluorescence signals of low intensity but discrete spectral pattern. The imaging hardware design that incorporates multiple excitation and emission filters allows the use of spectral unmixing techniques in order to discriminate between fluorescent objects of different spectral profiles. This is a very interesting feature, especially when it is combined with fluorescent proteins and genetically engineered mouse models. Since the majority of the commonly used proteins have an emission spectrum at the visible wavelengths and therefore suffer from strong parasitic signals (auto-fluorescence, food fluorescence), spectral unmixing is the ideal method to resolve the disease-specific activity from the surrounding unspecific fluorescence intensities.

2.5 Validation of other tomographic modalities

Of particular further importance is the use of the multispectral cryoslicing modality to validate the performance of non-invasive *in-vivo* fluorescence imaging approaches, such as fluorescence molecular tomography (FMT) (Ntziachristos, Tung et al. 2002) applied alone or in hybrid implementations together with X-ray computed tomography (FMT-XCT) (Schulz, Ale et al. 2010) or multispectral opto-acoustic tomography (MSOT) (Razansky, Distel et al. 2009).

Fig. 2-17c depicts a midline sagittal reconstructed slice of a mouse instilled with the near-infrared fluorophore Alexa Fluor 680. In the same image, the XCT information (black and white) displays the anatomical surroundings and is superimposed with the result of an FMT reconstruction algorithm in false color. The interest in this case was to compare the volumetric distribution of a novel FMT reconstruction method ('weighted-segments') with the cryoslicing imaging as the 'gold standard' for fluorescence 3D bio-distribution. For this reason, we compared the fluorescence intensity of four cross-sections on the lung as captured by the multispectral modality (Fig. 2-17a) with the corresponding virtual slices of the tomographic method (Fig. 2-17b). The anatomical cryoslicer images are displayed with a gray scale, while the fluorescence distribution is color coded with red and yellow denoting strong and moderate fluorescence signals correspondingly. It is evident that the weighted segments reconstruction method (Ale, Schulz et al. 2010) accurately correlates with the *ex-vivo* cryoslicing imaging results, both in shape and in intensity.

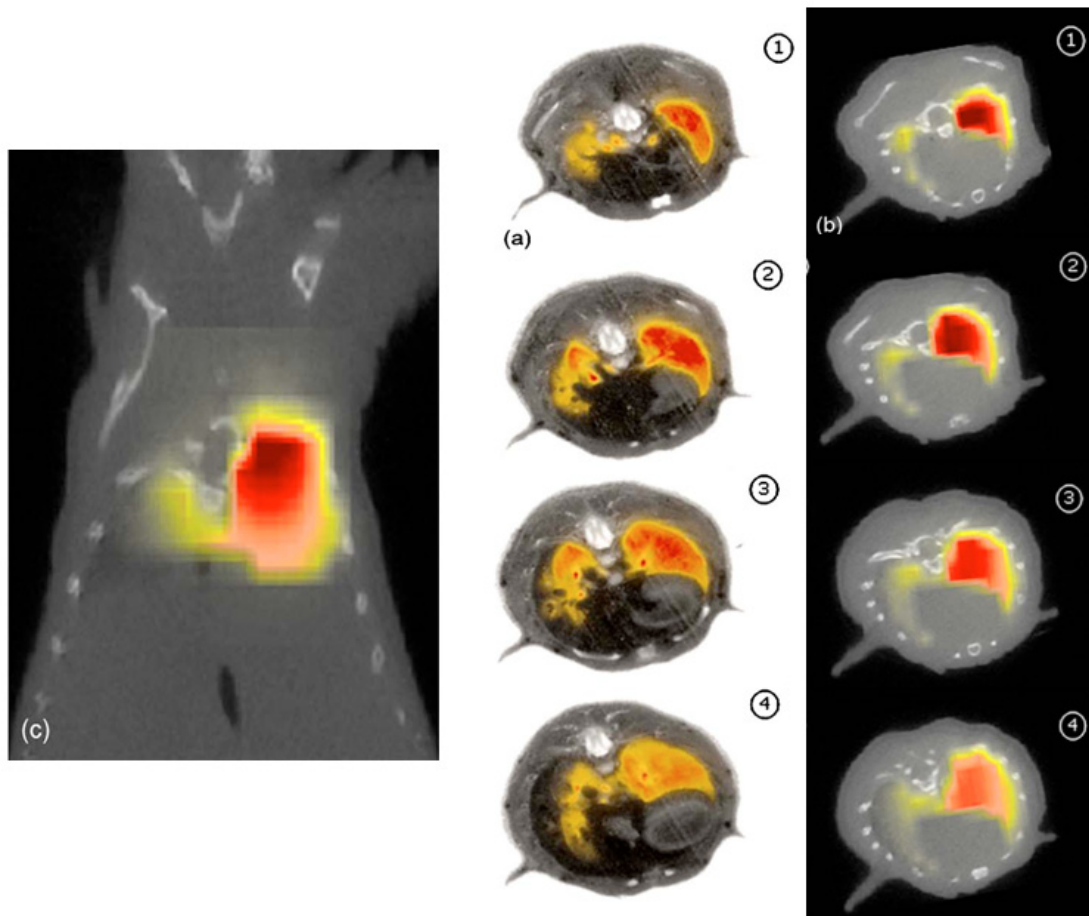


Figure 2-25. Cryoslicing cross-sections at the lung area. The anatomical image (b/w) overlaid with fluorescence image (a) and the FMT/XCT reconstruction using weighted segments regularization(b). A sagittal reconstructed slice depicts the fluorescence activity volumetrically inside the lung. Image taken from(Ale, Schulz et al. 2010).

It is interesting to note that we would not be able to visualize the intensity variations of the fluorescence signal within the lung (Fig. 2-17a1 compared to a4) using conventional planar fluorescence imaging, as it would only capture superficial information and would fail to accurately probe deeper inside the optically thick lung structure. Thus, this experiment demonstrates the basic advantage of cryoslicing imaging compared to planar fluorescence imaging, namely the acquisition of real three-dimensional fluorescence information.

Furthermore, Fig. 2-18 displays three cross-sectional images at the lower neck and upper thorax of a healthy mouse. Optoacoustic tomography reconstructions (Taruttis,

Herzog et al. 2010) are compared with the equivalent anatomical color images of the ‘gold standard’ cryoslicer for the accurate localization of carotid arteries and major veins in the

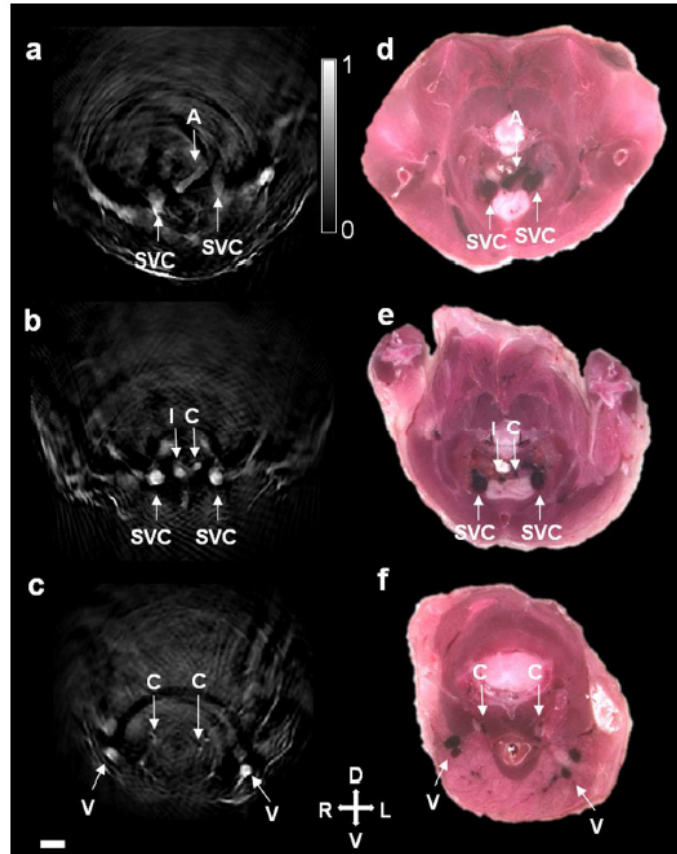


Figure 2-26. Transverse optoacoustic slices of arteries in the upper thorax and neck (a-c) and corresponding cryoslicing color images(d-f) A: aortic arch, SVC: left and right superior vena cava, I: Innominate artery, C: carotid arteries, V: veins branching from external jugular vein. Scale bar: 2 mm. Image taken from (Taruttis, Herzog et al. 2010).

area. This experiment showcases evidently that the ability to freeze mice under identical placement conditions to the ones used for *in vivo* imaging can provide accurate data that can be used as reference to confirm *in-vivo* images produced by tomographic techniques under development and to examine their imaging performance parameters during deep-tissue imaging, such as sensitivity or resolution achieved.

Chapter 3: Development of an experimental clinical-grade real-time intra-operative imaging system for surgical guidance

3.1 Introduction

Cancer is one of the most lethal diseases worldwide and particularly in the Western world. Although novel chemo- and radiotherapy approaches are being increasingly developed, it is overall accepted that surgical resection of cancer with tumor negative resection margins is the most efficient strategy against it, as it offers patients the best chance for long-term cancer cure. At the same time the surgical procedure should minimize unnecessary tissue removal in order to provide minimal post-operative complications.

For this purpose, many non-invasive imaging modalities have been developed and are commonly used in everyday clinical practice. Magnetic resonance imaging (MRI), positron emission tomography (PET), ultrasound (US), x-ray computed tomography (CT), gamma cameras and probes have appealing characteristics and can be utilized to non-invasively provide information concerning tumor existence and localization, growth and

volume, metabolism (FDG-PET) and perfusion during pre-operative diagnosis, the surgical procedure and post-operative therapy. Being increasingly developed in the last decade, fluorescence imaging is now starting to be considered as a promising complementary technology for the clinical practice, thanks to its attractive characteristics. The use of non-ionizing radiation, the real-time video rate operation, the ease-of-use and the portable size of small form factor make fluorescence imaging an ideal candidate to provide useful information, both at the diagnostic and therapy monitoring level using non-invasive tomographic techniques (i.e. fluorescence and optoacoustic tomography) and for image-guided surgery using planar imaging modalities. The primary advantage of fluorescence technology, however, is the plethora of increasingly available fluorescent bio-markers that are currently being developed (proteins, antibodies, peptidomimetics, etc) and are expected to reach clinical translation in the coming years. Being able to specifically identify carcinogenesis, inflammation, neuronal activity or simply local vascularization, these targeting moieties can be extremely useful in various cases of disease.

In surgical oncology, in particular, a field where other modalities (MRI, PET, CT) provide limited information, planar fluorescence imaging could potentially play a leading role. Typically the outcome of a surgical intervention depends mostly on the skills and experience of the surgeon, who, during the operation, relies only on his color vision (color appearance) and haptic perception (tissue stiffness or elasticity) in order to distinguish cancerous tissue from healthy and excise it. Although pre-operative data from non-invasive modalities are available during the surgical procedure, they are of limited use as the imaging has been typically performed days before the actual surgery. For this reason, the 3D volumes acquired are difficult to be interpreted from the surgeon both due to the unavoidable movement of internal organs and tissues but also due to the different visualization provided (different, mismatched coordinate systems) and the, sometimes, limited anatomical information of such modalities (i.e. PET) about the tumor at its surroundings. In contrast, planar fluorescence imaging is an ideal modality for image-guided surgery, since tumor surfaces are exposed during surgical resection. Furthermore early

tumors arise relatively superficially in intra-epithelial layers and can, thus, be easily imaged. As a result, it is in surgery that fluorescence technology can capitalize on its advantages of ease-of-use and non-harmful radiation, but most importantly on its real-time operation that relies directly to the surgeon's vision and course of action. Ultimately, the goal of planar fluorescence imaging is to enhance surgical vision in real-time by bringing to light anatomical and functional characteristics of biological tissue and to provide surgeons with feedback in order to accurately identify cancerous tissue and resect it, while leaving negative resection margins and minimally affecting surrounding structures.

Although clinical imaging using fluorophores is considered at least since 1947 (Moore 1947), it has only recently received a revitalized interest for clinical trials of intra-operative fluorescence-based image-guided surgery in oncology. The first major impact clinical fluorescence imaging trials of recent years for surgical feedback and guidance were performed not earlier than the 2000s, studying the use of ICG for the detection of sentinel lymph nodes (Trojan, Kianzad et al. 2009) and as a contrast agent of hepatocellular cancer. The studies presented herein are not only re-introducing fluorescence imaging at the clinical environment but also pushing the field into new pathways for the future by introducing novel applications of fluorescence-guided surgery and the idea of systemically administered targeted fluorescent agents presenting the first-in-human targeted fluorophore clinical trial.

The scope of the current work has been the development of a clinical-grade multispectral intra-operative imaging setup for image-guided surgery, its introduction to the routine clinical environment and its application in a number of first-ever clinical studies using non-targeted and targeted fluorescent agents for the identification of sentinel lymph nodes (SLNs) and cancer.

The remainder of the Chapter is structured as follows. In section 3.2 we describe in detail the real-time multispectral fluorescence imaging implementation that we developed. Section 3.3 presents an animal study that was carried out during the system development

process that showcases the benefits of targeted fluorophores for real-time surgical feedback and accurate tumor resection. In section 3.4 we introduce the imaging protocol that was used during our clinical trials, which are in turn are presented in Chapter 3.5. These include sentinel lymph node detection studies for breast cancer patients and in gynecologic oncology as well as the first-ever clinical trial with targeted fluorophores in ovarian cancer patients. Finally Chapter 3.6 summarizes the clinical results and discusses about the future role of planar fluorescence imaging in surgical oncology.

3.2 Development of a clinical-grade real-time intra-operative multispectral imaging system for surgical guidance

The development of our clinical-grade intra-operative setup was based on an earlier experimental multispectral system previously described (Themelis, Yoo et al. 2009), that was however fundamentally altered to meet the challenging and stringent rules of clinical imaging. The basic alterations had to do with the overall fluorescence sensitivity, the flexibility to image multiple fluorophores and the requirement of easy sterilization. Overall, our aim was to develop a multispectral imaging setup for image-guided surgery that would provide real-time feedback to the surgeon inside the operating theater that would be easy-to-use. The experimental system and the imaging procedure should not intervene during the standardized surgical procedure or unnecessarily prolong surgery. Furthermore the imaging system should have a high sensitivity especially for fluorescence imaging in order to produce video streams of high frame rate, good dynamic range and high accuracy. Moreover it should be able to operate multiple cameras at the same time capturing reflectance and fluorescence video streams and should be flexible to image various fluorophores in the visible and near-infrared area of the spectrum, creating, thus, an adaptable imaging platform for the evaluation of novel targeted contrast agents.

For this reason, the trans-illumination arm and glass window of the previous system version were abandoned along with the x-y translational stages. In contrast we used the same zoom lens that provided high magnification and variable field of view with a zoom factor of 6:1 and the same relay lenses for all 3 imaging channels. The main shortcoming of the previous implementation was the sensitivity of the fluorescence camera. Imaging in the near-infrared is especially challenging and only few devices can achieve high quantum efficiency above 700nm. Thus, for the clinical-grade setup we chose a CCD camera with electron-multiplying technology (DU-897, Andor Technology, Belfast, UK) that could meet the requirements of high sensitivity (QE>60% at 850nm) and frame rate.

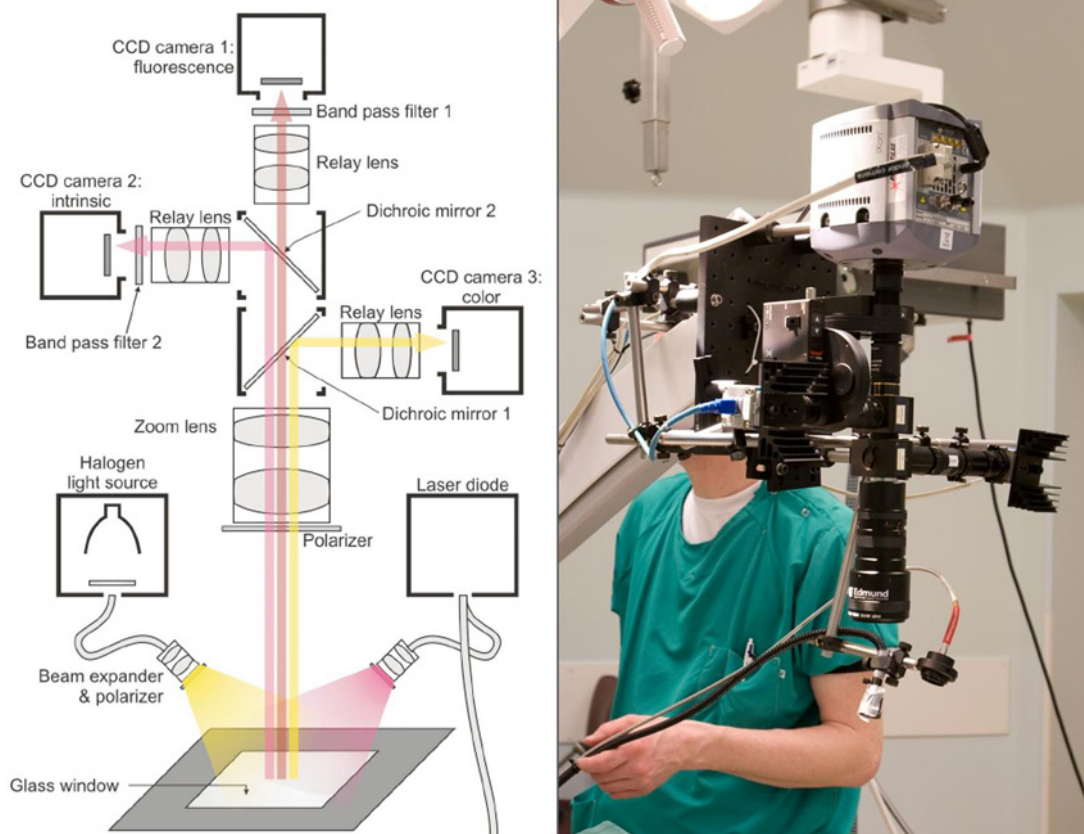


Figure 3-1. Schematic of the developed intra-operative imaging setup featuring a parallel-capturing three-camera (color, intrinsic, fluorescence) system. Two filter wheels for the selection of the suitable emission and intrinsic filters when different fluorophores are imaged.

It should be noted that sensitivity is of utmost importance in clinical imaging as it significantly speeds up the imaging procedure by providing motion free images and considerably facilitates the system movement, handling and the easy selection of the desired field of view from the surgeon. To further enhance the ability to image multiple fluorescent probes, 2 pc-controlled motorized filter wheels (FW102B, Thorlabs, Newton, NJ, USA) were installed in front of the intrinsic and fluorescence camera respectively and control the selection of the appropriate filters. In this way we created a modular imaging platform that could accommodate the imaging of different fluorescent probes with excitation and emission at different wavelength bands.

Accordingly, new optical filters (all from Chroma, Rockingham, VT, USA except from NF03-532E-25 from Semrock, Rochester, NY, USA) with high off-band blocking capabilities were used in order to optimally match both the excitation and the emission spectra of ICG, Cy5.5 and FITC spectral bands for the intrinsic and fluorescent filter wheel respectively. To optimize the multispectral imaging system for clinical use and provide mobility custom adapters (Boehm & Wiedemann, Eching, Germany) were constructed in order to mount the imaging system on a commercial surgical microscope arm (OPMI 1 FC, Zeiss, Sliedrecht, the Netherlands) and to allow many degrees of freedom for accurate and easy movement and positioning of the camera assembly. Easy sterilization was achieved with standard exchangeable sterile drapes (Carl Zeiss Vision BV, Sliedrecht, the Netherlands, OPMI Drape REF 306071) thanks to the system design approach of small form factor. White light for the color imaging and excitation light for contrast agents fluorescing in the visible range is provided by a cold light source (KL2500LCD, Carl Zeiss Microimaging GmbH, Göttingen, Germany), while infrared excitation light is supplied by two diode lasers at 673nm and 750nm (B & W Tek, Newark, DE, USA). Finally, after the final setup assembly, current leakage tests were performed to ensure that the device is safe for use in patients.

Although more modes of operation are possible, at the current implementation, our multispectral clinical-grade setup is able to capture color and fluorescence video streams for fluorophores excited at 488nm (Fluorescein-labelled), 680nm (Cy5.5-labelled) or 750nm

(AlexaFluor750-labelled or Indocyanine Green (ICG)). Reflectance videos are simultaneously recorded at the excitation wavelength ('intrinsic') of each fluorophore. The maximum frame rate is currently hardware-limited at 12fps, which is satisfactory for clinical imaging. Of primary interest was the ability to provide both anatomical (color) and fluorescence feedback (as well as their overlay) to the surgeon for every mode of operation. This is a very important feature for image-guided surgery as it allows the surgeon to precisely identify the exact location of fluorescence bio-distributions and associate it with his direct field of view in the complex surgical environment which usually includes multiple tissue types of varying morphology and/or cavities.



Figure 3-2. Picture of the developed multispectral intra-operative system during measurements inside the operating room. Specialized microscope drapes are used for sterilization, while the small form factor of the setup minimally intervenes in the surgical field.

Although various groups around the world have been working on developing imaging setups for clinical fluorescence imaging, we can argue that our approach is not only unique but also the most appropriate for image-guided surgery. Multiple implantations of highly sensitive fluorescent imagers have been developed (Sevick-Muraca, Sharma et al. 2008; Pic, Pons et al. 2010); the lack of ability, however, to provide real-time anatomical (color) information considerably reduces not only the user-friendliness and flexibility of the approach as well as the ability to clearly and quickly interpret images. It is, for instance, a common case in ICG imaging that the fluorescent signal originating from a lymph node or a lymphatic vessel is spatially so restricted that without any visual color reference it is difficult and time-consuming even for the surgeon to localize its origin. Thus, such implementations are a lot more suited for pre-clinical or pre-operative studies rather than surgical guidance.

Furthermore, although the significance of tissue optical properties inhomogeneity and its effects on fluorescence imaging is often neglected (Trojan, Kianzad et al. 2009), it is of utmost importance in surgical guidance. In this work, we show specific examples that describe how even moderate variations in absorption and scattering properties of tissues can fundamentally influence the captured fluorescence images and induce false positives and false negatives (Chapter 7 and 8). From this point of view, our clinical-grade multispectral imaging system is unique since it features a specific correction approach (Themelis, Yoo et al. 2009) that can be followed to compensate and reduce the effects of optical properties variations.

3.3 Animal Studies

3.3.1 Tumor margins identification

Introduction

This study was designed to examine the performance of the newly developed clinical imaging system and to investigate whether intra-operative fluorescence imaging could assist and improve the procedure and outcome of cancer surgery by means of real-time molecular feedback of tumor spread and margin delineation using targeted near-infrared fluorescent probes with specificity to tumor biomarkers. Currently, the assessment of tumor borders is achieved by post-operative pathology or, less reliably, intra-operative frozen sectioning. We showcase that, with the use of targeted probes, fluorescence intra-operative imaging can significantly improve the surgical feedback and outcome and can lead to a highly accurate and tumor-specific surgical resection.

Studied animals

The commercially available bioluminescent human breast cancer cell line MDA-MB-231-luc-D3H2LN (Caliper Life Sciences, Hopkinton, MA, USA) was used to establish a xenograft tumor model by implanting 2 million MDA-MB-231-luc-D3H2LN cells in the pectoral mammary fat pad of 6-week-old female nude mice. This luciferase-expressing human adenocarcinoma cell line was chosen as it enables the use of bioluminescence imaging as 'gold standard' for corroboration and comparison of the fluorescence imaging. A total of 12 mice were inoculated and nine mice showed tumor growth after 3–4 weeks. Among them, three mice developed a tumor with a size of 10 mm, with involvement of the pectoral muscle as determined by palpation and confirmed by surgery, while six mice developed tumors of 5 mm or smaller with involvement of the overlying skin. At this point, the tumor-bearing animals were administered with IntegriSense680 (2 nmol) that specifically targets the avb3-integrin receptor via an intravenous injection in the tail vein. 24 hours later and 10 minutes before the surgery, the animals were injected intraperitoneally with D-luciferin (Caliper Life Sciences) at a dose of 150 mg/kg. Subsequently, the surgical tumor resection procedure was simulated on mice under isoflurane anaesthesia, while both bioluminescence and fluorescence imaging was performed.

Imaging procedure

The experimental procedure consisted of the following steps: A) the tumor was exposed by removing the overlying skin. Bioluminescence images were captured using a separate CCD camera (DU-888, Andor Technology, Belfast, UK), while fluorescence, intrinsic, and color images of the region of interest were obtained using the developed custom multispectral clinical imaging setup. B) 90% of the tumor was removed by the surgeon under visual guidance, leaving behind a rim of tissue (around 10%) to simulate residual disease and examine the ability of fluorescence imaging to detect smaller foci of disease. After this excision, the imaging procedure of step A was repeated. C) The residual 10% of the tumor was removed under visual guidance. Afterwards, under fluorescence guidance, any fluorescent lesions that appeared in the field of view were also removed. D) Non-fluorescing tissue that surrounded the tumor was also taken as control tissue for pathological examination. Subsequently, the mice were euthanized by a lethal dose of ketamine, while all removed tissue samples were immediately imaged *ex-vivo* as in step A. All tissues were then snap-frozen in liquid nitrogen and stored at -80C for histological analysis of the resection margins. All excised tissue specimens were submitted to hematoxylin and eosin (H&E) staining for the presence or absence of tumor. The histological analysis was performed by an expert oncology pathologist who was blinded to the imaging results.

Results

Figure 3-3 shows bioluminescence and fluorescence images from a tumor bearing mouse overlaid on the equivalent color images at different stages of the simulated surgical excision. The three rows of images correspond to surgical steps A–C. The first two columns depict *in-vivo* bioluminescence images and fluorescence epi-illumination images respectively captured during the surgical procedure, while the third column illustrates the corresponding *ex-vivo* images of excised tissue.

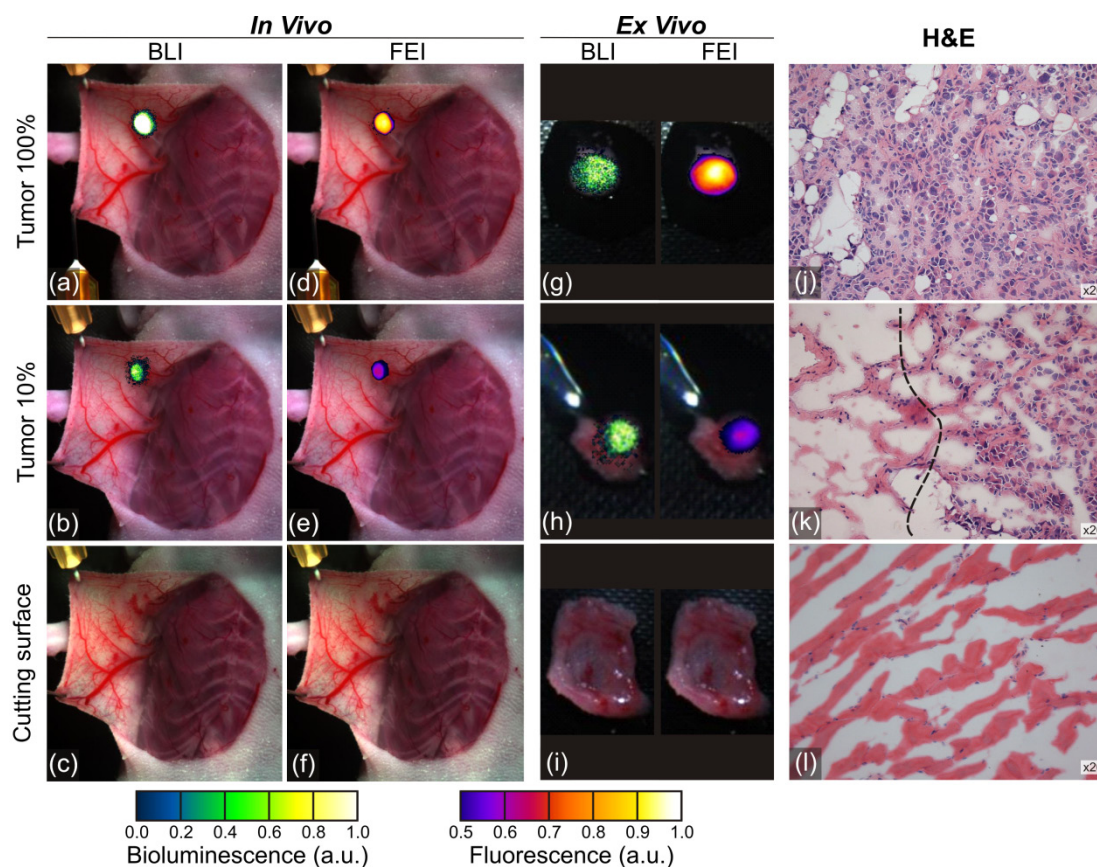


Figure 3-3. In-vivo and ex-vivo intra-operative fluorescence epi-illumination imaging (FEI) in a xenograft breast cancer mouse model. The detected signal of the bioluminescence (BLI) (a, b, c) and fluorescence images (FEI) (d, e, f) were compared by using different pseudo-color scales (BLI = green/fire/blue, FEI = fire). BLI and FEI show good correspondence in anatomical localization both in-vivo and ex-vivo (g, h, i). All excised tissue was confirmed to be tumor-positive by H&E staining (j, k). Interestingly, the rim of healthy tissue can be visualized (k) with a black interrupted line. In the cutting surface (l) there was no tumor detectable.

In this way, bioluminescence signals can be used for direct 1:1 confirmation of the fluorescence images both for *in-vivo* and *ex-vivo* images. On the fourth column are displayed H&E images that originated from the tissue samples imaged at the third column.

Bioluminescence signals were detected in all tumor bearing mice, confirming, thus, tumor growth and demonstrating the extent of tumor spread. In comparison, fluorescence imaging not only detected all tumors, it also successfully guided total tumor excision by effectively detecting small tumor residuals of strong contrast, occasionally overlooked by

the surgeon during the visual examination. Overall, the fluorescence images were in very good correspondence with the ‘gold standard’ bioluminescence images in respect to signal co-localization and distribution, even in cases of particularly small foci of disease as depicted in Fig. 3-3h. The bioluminescence and fluorescence results were further validated by histology. Fig. 3-3k clear demonstrates a distinct margin between healthy and cancerous tissue and confirms the margin between fluorescence and non-fluorescent regions seen on the *ex-vivo* images of Fig. 3-3h obtained from the same sample before staining. Similarly, Fig. 3-3i confirmed a cancer-free tissue in fluorescence-free samples. Overall, histopathology confirmed the capability of the method to identify tumor negative margins with high specificity and better prediction rate compared with visual inspection.

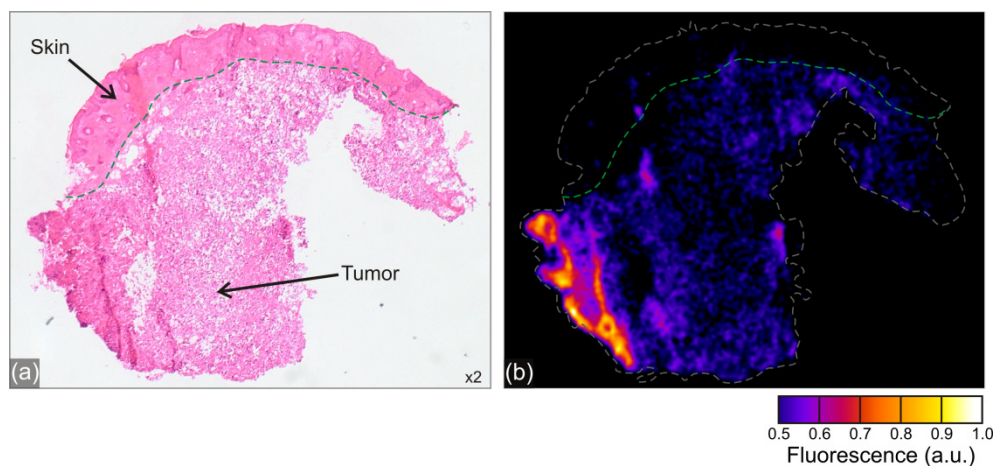


Figure 3-4. H&E staining (a) and planar fluorescence image (b) of a cryosection (10µm) of residual breast tumor that grew into the overlying skin. The green interrupted line depicts the border between tumor and healthy tissue. The fluorescent signal was distinctly stronger in the tumor area and noticeably followed the tumor border.

To further examine the spatial agreement of fluorescence signals and histological findings, planar fluorescence images of tissue slices were acquired from the excised tissue before the H&E staining and were contrasted to the results obtained after the staining. Fig. 3-4 shows representative results from a tumor that developed in the skin and was radically resected. This image demonstrates excellent congruence between the appearance of the tumor and the result of histological analysis on the H&E slice and the corresponding fluorescence distribution illustrated with the false color scale. Clear borders between tumor

and healthy skin tissue in Fig. 3-3b suggest that fluorescence imaging with systemically administered tumor-selective fluorescent probes can precisely identify the tumor area and borders, guide the surgical resection and provide, thus, negative tumor margins (R0 resection).

Furthermore, a tumor-to-background ratio (TBR) analysis was performed to obtain metrics on the contrast achieved. Background tissue was defined as the area directly next to the tumor and was calculated as the average of four regions of interest (ROI) selected adjacent to the tumor (proximal, distal, lateral, and medial). Interestingly, tumor tissue exhibited target-to-background ratio of 4.0 ± 0.67 , which was significantly higher compared with white-light images representing the visual contrast (Themelis, Harlaar et al. 2011).

Discussion

We investigated the combination of our clinical-grade intra-operative imaging system for fluorescence imaging, together with a systemically administered avb3-integrin targeting fluorescence agent as a novel imaging strategy toward the detection of microscopic residual disease and invasive borders. Indeed, fluorescence imaging can successfully identify tumor margins when coupled to targeted fluorescent probes. Results showcased sensitive and robust performance that improved the surgical outcome over human vision, in small animal surgery. Interestingly, the findings showed that fluorescence guidance not only correctly identified the primary tumor but also accurately detected residual disease with high contrast.

Curative resection (R0) is the ultimate goal of surgical oncology and is predominantly dependent on local invasion in surrounding tissues; yet, modern surgical oncology is confronted with limitations in achieving negative margins. The absence of real-time feedback on the pathological appearance of tissue is a major deficiency that often restricts the identification of remnant disease. The current 'gold standard' of cancer confirmation and margin evaluation is the pathological examination of the excised specimen, which accurately observes the margin status. However, complete sensitive

histopathological examination usually lasts several days and often only a part of the specimen is examined. Thus, pathological examination does not generally allow for an immediate evaluation of the surgical outcome. Real-time multispectral fluorescence imaging using tumor specific molecular probes is a promising modality for the evaluation of tumor resection, as it can efficiently provide real-time feedback and surgical guidance and possibly improve surgical procedures, thanks to its high flexibility in contrast mechanisms, higher resolution than human vision, and real-time feedback.

3.3.2 Clinical imaging setup evaluation

Introduction

In parallel with the previous study we investigated technical aspects of the developed clinical-grade multispectral imaging setup such as resolution, sensitivity and frame rate, portability and movement capabilities (rotation, height adjustment, zooming, etc). Furthermore, we explored multiple approaches to overlay the fluorescence signal on top of the color image and thoroughly tested the general surgeon-device interface for user-friendliness and accessibility. To achieve this, the multispectral imaging platform was covered with a sterile drape and the real surgical procedure was simulated: the surgeon was asked to resect tumors in mouse xenograft models using only the fluorescence-on-color function of the software in order to test its performance and confirm its suitability for real-time surgical guidance.

Studied animals

Two animals implanted with MDA-MB-231 cells were used, while a supplementary ovarian cancer model was established by an intra-peritoneal injection of 1 million A2780 (human ovarian cancer) cells in three additional female nude mice. The tumors were allowed to grow for 3 weeks and at that point the animals were injected with

IntegriSense750 that was allowed to circulate and bind for 24h before the surgery. This wavelength channel was used as it was more relevant to the clinical imaging of ICG, as the same laser excitation (diode laser, fiber bundle, light diffuser) and filter set would be used in both cases. All mice were kept on a fluorescence free diet (type) in order to minimize food fluorescence that would inevitably reduce contrast during the ovarian cancer resection procedure.

Results

Only video streams (no snapshots) of fluorescence, color, intrinsic and their overlay were captured during these experiments, while the surgeon was asked to personally handle

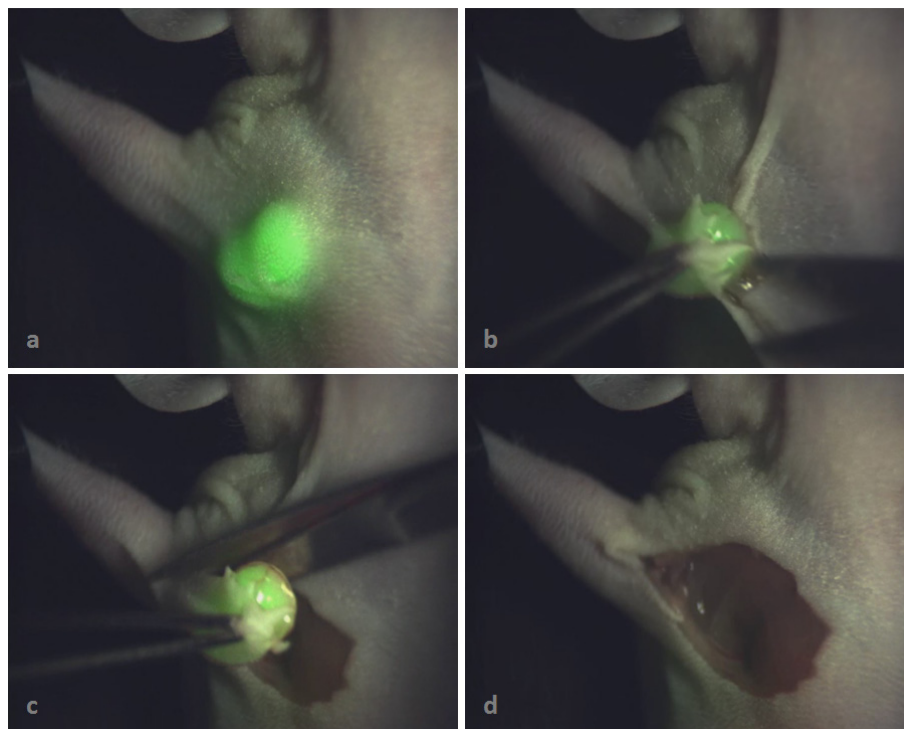


Figure 3-5. Different frames during the tumor resection surgery in a tumor bearing xenograft mouse model. Even before the first incision (a) the tumor has a strong contrast and can be easily distinguished. Instances during the surgical procedure (b, c) showcase the straightforward use of the setup as it allows the surgeon to clearly detect the tumor borders and thus resect the entire tumor, leaving no fluorescence spots (d) at the surgical cavity.

the imaging system and set the preferred field of view. The emphasis was this time on inducing a high frame rate (around 10fps) in order to simulate the real-time surgical resection and fluorescence feedback inside the operating room. Fig. 3-5 depicts various individual color frames overlaid with the fluorescence signal at four different instances during the surgical procedure. Generally, the good localization of IntegriSense inside the subcutaneous tumor provides high fluorescent contrast. Therefore, accurate visualization of the tumor and its borders is possible also before the initial section (Fig. 3-5a) due to the thin (~1-2mm) overlying skin tissue and the reduced tissue absorption at near-infrared wavelengths. For the overlay the preferred approach was to add the fluorescence signal in the green channel of the color image in order to create a pseudo-color appearance that is easy to distinguish from surrounding tissues and is absent in the human body. Throughout the study, the green tumor color was found not to disturb the surgeon's operation during the resection process and to clearly distinguish cancerous tissue from its neighboring tissues of red color appearance. Further images (Fig. 3-5b-d) demonstrate good tumor border identification that facilitated a quick and efficient surgical resection and a fluorescence-free surgical cavity at the end of the procedure.

Although IntegriSense did not supply the same contrast in A2780 animals as in the breast cancer xenografts due to auto-fluorescence from the intestinal tract and possibly not as high probe binding, it selectively targeted the tumors and significantly aided resection by providing local contrast. By comparison with Fig. 3-5a, visual inspection of the ovarian cancer mice (Fig. 3-6a) did not show an accurately delineated tumor, but rather a blurred area of fluorophore accumulation. This is attributed to the more irregular tumor morphology and the complex surrounding structures that can easily mask the cancerous lesions. Once the surgical cavity was exposed (Fig. 3-6b), tumor resection under the system's guidance could be easily accomplished. In almost all ovarian cancer cases, the animals developed more than one primary tumors. In these cases the fluorescence guidance was especially valuable since it could quickly and clearly identify small local

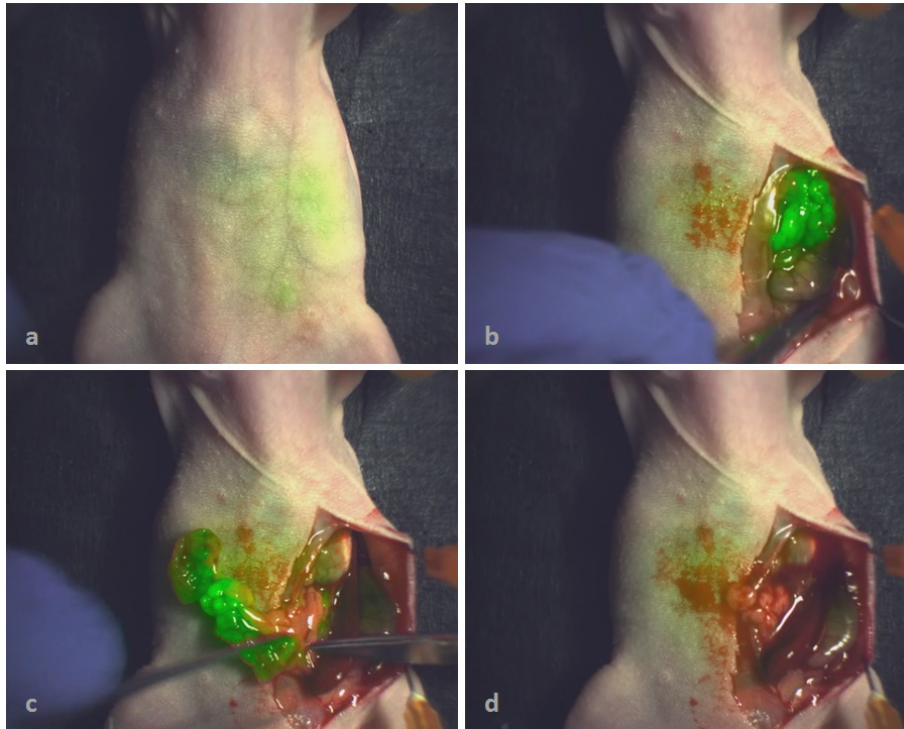


Figure 3-6. Different frames during the tumor resection surgery in an ovarian cancer mouse model. In this case, the exact tumor localization was not clearly visible before the first incision (a). However, during the surgical procedure (b, c), the surgeon could successfully identify areas of tumor development and resect them, leaving no fluorescence spots (d) at the surgical cavity.

tumors or metastases during the visual inspection that would otherwise be missed by the surgeon. Histological analysis was not as intricate as in the previous study, it confirmed, however, that the resected tissues were indeed cancerous.

3.4 Clinical Imaging Protocols

The following research protocols describe the procedural steps for fluorescence intra-operative imaging during clinical studies of image-guided surgery. Both protocols were approved by the local Investigational Review Board (IRB) of the University Medical

Center Groningen and the patients' documented informed consents were acquired prior to all clinical trials.

Intra-operative imaging of lymph nodes with a local injection(s) of Indocyanine Green (ICG)

I. The multispectral imaging setup is introduced and positioned inside the operating theatre prior to surgery to minimize interference with the standard surgical procedure. The computer units are connected to the operating room monitors and the imaging system is initialized. Image registration algorithms are executed, computer memory is allocated and the intra-operative system is set in standby mode. Finally, the camera setup is covered in sterile drapes.

II. During the initial steps of the surgical procedure, the fluorescent contrast agent indocyanine green (ICG) is prepared under sterile conditions. A vial of 25 mg ICG powder (Pulsion Medical Systems AG, Munich, Germany) is dissolved in 50 ml of sterile distilled water (B. Braun Medical), to yield a concentration of 0.5 mg/ml. 1.0ml of the solution is mixed with 1.0 ml of standard blue dye (that is commonly used for lymph node identification) (patent blue, Guerbet, France) in one syringe, which is kept in a light-tight environment to prevent fluorescence bleaching.

III. When the area of interest is exposed, the imaging setup is rolled above the patient and the camera field of view (zoom, focus) is adjusted by the surgeon. Lights in the operating theatre are switched off to prevent cross-talk, while the surgical procedure continues using the imaging setup's individual white light illumination, as near-infrared light is invisible and there is no change on the look of the surgical field. Video recording for all three imaging channels is performed while the surgeon injects the ICG-patent blue solution in four quadrants around the primary tumor. Lymphatic flow and ICG accumulation in the sentinel lymph node (SLN) are captured, processed and displayed in real-time to assist the

SLN identification procedure. In parallel, the SLN is also detected according to the standard protocol, either using a gamma probe (the radioactive tracer (99mTc-nanocolloid, GEHealthcare BV, Eindhoven, the Netherlands) is typically administered one day before surgery) and/or by visual inspection of a local blue discoloration.

IV. The real-time SLN excision is guided by all three ‘modalities’ (intra-operative imaging, gamma probe and visual inspection). After the successful SLN identification and removal, the surgical field is scanned for additional lymph nodes as previously.

V. After the excision of all the lymph nodes, the multispectral system is rolled outside of the surgical field and *ex-vivo* still images of the excised samples are acquired. The exposure times are here generally longer than in Step III in favor of a higher dynamic range. Finally, the excised samples are labeled and sent for histopathological analysis.

Throughout the SLN imaging procedure and especially during the ICG preparation and injection, it is important to prevent ICG leaks that would contaminate the camera field of view, as ICG is a highly fluorescing dye. Such parasitical contributions can be best avoided by frequently changing gloves or by locally covering the tissue area where ICG has accidentally escaped.

Intra-operative imaging of ovarian cancer with a systemic injection of a folate-targeting fluorescent agent (folate-FITC)

I. The targeted fluorescent agent folate-FITC is produced and supplied by Endocyte Inc. (West Lafayette, IN, USA). For every patient, one vial is dissolved in 10 ml sterile normal saline and this solution is intravenously injected 2 hours prior to surgery at a dose of 0.3 mg/kg body weight over a period of 10 minutes. After the administration of folate-FITC, all patients are monitored during the in-hospital admission. Patients are not limited in their normal behavior or intake of diet or medication prior to the study.

II. The multispectral imaging setup is introduced and positioned inside the operating theatre prior to surgery as in Step II of the previous protocol.

III. After the abdominal cavity has been exposed, inspected and palpated by the surgeon and the tumor(s) has been localized, the imaging setup is rolled above the patient and the camera field of view is adjusted by the surgeon. Lights in the operating theatre are switched off during imaging to prevent cross-talk, while the surgical procedure continues using the multispectral setup's individual white light illumination, as there is no change on the look of the surgical field. Video recording for all three imaging channels is performed, as the surgeon is free to change the intra-operative system's field of view and navigate inside the abdominal cavity in order to discover and easily visualize cancerous tissue(s) with high magnification.

IV. The surgeon proceeds with the standard procedure. All tumor-suspicious tissue(s) are excised while *in-vivo* video streams are captured by the multispectral imaging setup both during and after the excision for remnant fluorescence signals.

V. The multispectral system is rolled outside of the surgical field and *ex-vivo* still images of the excised samples are acquired. Finally, the excised samples are labeled and sent for histopathological analysis.

During the surgical procedure, Steps III, IV and V might be several times repeated as the surgeon discovers additional fluorescent/tumor deposits inside the abdomen.

Throughout all the clinical trials, disinfectants, surgical markers, drapes and generally anything that could potentially influence the imaging procedure by generating false fluorescence signals was carefully selected and even avoided if found out to auto-fluoresce.

3.5 Clinical Studies

Prior to the beginning of the clinical studies phantom measurements were performed (Pleijhuis, Langhout et al. 2011) to identify the optimal ICG concentration and

the maximum imaging depth of our setup. Furthermore, corpse measurements were carried out to familiarize the personnel with the imaging procedure (camera movement, handling of the zoom lens) and better coordinate the operating surgeons with the people responsible for the camera system control (Sarantopoulos and Themelis) and image acquisition. Standardized procedures were also developed in order to make camera handling and image acquisition easy and efficient also for non-specialized staff.

3.5.1 Intra-operative imaging for sentinel lymph node (SLN) detection (breast, cervix and vulva cancer)

Introduction

The patient's prognosis in almost all solid tumors cases depends on the presence or absence of lymph node metastases (Tinga, Bouma et al. 1992; Zivanovic, Khoury-Collado et al. 2009; McMahon, Rofsky et al. 2010), with positive LNs adding to an unfavorable prognosis (Tinga, Bouma et al. 1992; Horn, Hentschel et al. 2008). For this reason, surgical treatment most commonly combines the radical excision of the tumor with a full lymphadenectomy in the drainage area of the tumor. However, removal of lymph nodes is associated with increased morbidity due to infection, wound breakdown and lymphedema (Matsuura, Kawagoe et al. 2006; Beesley, Janda et al. 2007; Ayhan, Celik et al. 2008; Füller, Guderian et al. 2008). As an alternative, the sentinel lymph node (SLN) procedure was suggested several decades ago to detect the first draining lymph node from the tumor (Tanis, Nieweg et al. 2001). In case of lymphogenic dissemination, the SLN is the first lymph node that is affected (Fig. 3-7). Thus, if the SLN does not contain metastases, downstream lymph nodes will also be free from tumor metastases and do not need to be removed. The SLN procedure concept, over the last decades, has proven feasible and safe and is now part of the treatment for many tumor types, like breast cancer, early gastric cancer and melanoma [90-94], but also for cancer of the vulva and cervix (El-Ghobashy and Saidi 2009).

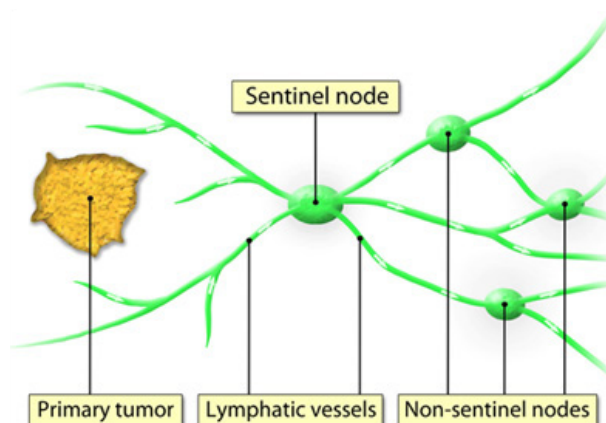


Figure 3-7. A schematic showing the sentinel lymph node (SLN) theory (Crane, Themelis et al. 2010). The SLN is the first draining lymph node from the tumor surrounding and therefore possible metastases will first appear there. In this way, excessive lymphadenectomy is reduced.

The current standard methodology for SLN detection is by a peritumoral injection of a ^{99m}Tc radio-colloid one day prior to surgery, and a dye of blue color appearance intra-operatively (Rasty 2009). Disadvantages of the procedure in cervix and vulva cancer are multiple injections in the genital area, leading to increased stress for the patient, and the use of radioactivity. As an alternative, we investigate the use of multispectral intra-operative fluorescence imaging for real-time identification of the SLN and for lymphatic drainage mapping in breast, cervix and vulva cancer patients. Our proposed approach eliminates the risks and adverse effects associated with the exposure to radioactivity, provides a real-time mapping of the lymphatic system as opposed to point measurements with a Geiger counter (radiotracer) and turns the SLN detection into a one-time procedure, reducing thus the patient stress and discomfort.

During all studies, indocyanine green (ICG) was used for the SLN detection, as it currently is the only near-infrared fluorophore with FDA approval for use in humans thanks to its a safe pharmaco-biological profile and inert nature. Imaging of fluorophores in the near-infrared area of the spectrum provides high contrast with the background tissue due to the reduced tissue auto-fluorescence and enables the acquisition of 'depth' information,

as near-infrared light penetrates 'deeper' inside tissues (several millimeters depending also on the tissue optical properties) compared with visible light.

All clinical pilot studies were approved by the Institutional Review Board of the University Medical Center Groningen and were performed in accordance with the ethical standards of the Helsinki Declaration of 1975. The total number of patients that were included in all studies (breast, cervix and vulva cancer) was 30, 10 for each. The coordination of the recruitment of all patients for intra-operative fluorescence imaging during the SLN detection was performed by the UMCG investigators (GVD, LC) by considering the patients' accordance to several criteria (Crane, Themelis et al. 2010; Crane 2010; Crane, Themelis et al. 2010 ; Crane, Themelis et al. 2011) and after documented informed consent.

Results

Representative images from the clinical trials are summarized in Fig. 3-8. The SLN detection of breast cancer patients was performed first, as it required a less tedious camera positioning and did not involve a lengthy lymph node excision procedure as in the case of gynecologic cancers. In all cases, the first LN with considerable fluorescence accumulation was denominated as the SLN. The SLN or—in the case of bilateral lymph flow— multiple SLNs were *in-vivo* identified, removed and the fluorescence signal was quantified *ex-vivo*. Next, the remaining LNs were dissected and evaluated for fluorescence and blue discoloration *ex-vivo*. In case no fluorescent SLN was found *in-vivo*, all LNs were dissected and evaluated *ex-vivo*. All LNs were sent to the pathologist for histopathological examination. In the case of a fluorescent hot spot in a cluster of LNs, the fluorescent node was excised and examined separately for tumor involvement. For some breast cancer patients, local massage of the axillary area was applied to aid the ICG propulsion, if no forward motion of the fluorophore was observed for more than 10 seconds. Fig. 3-8a-c depict one instant (frame) during the video recording of the ICG drainage towards the SLN.

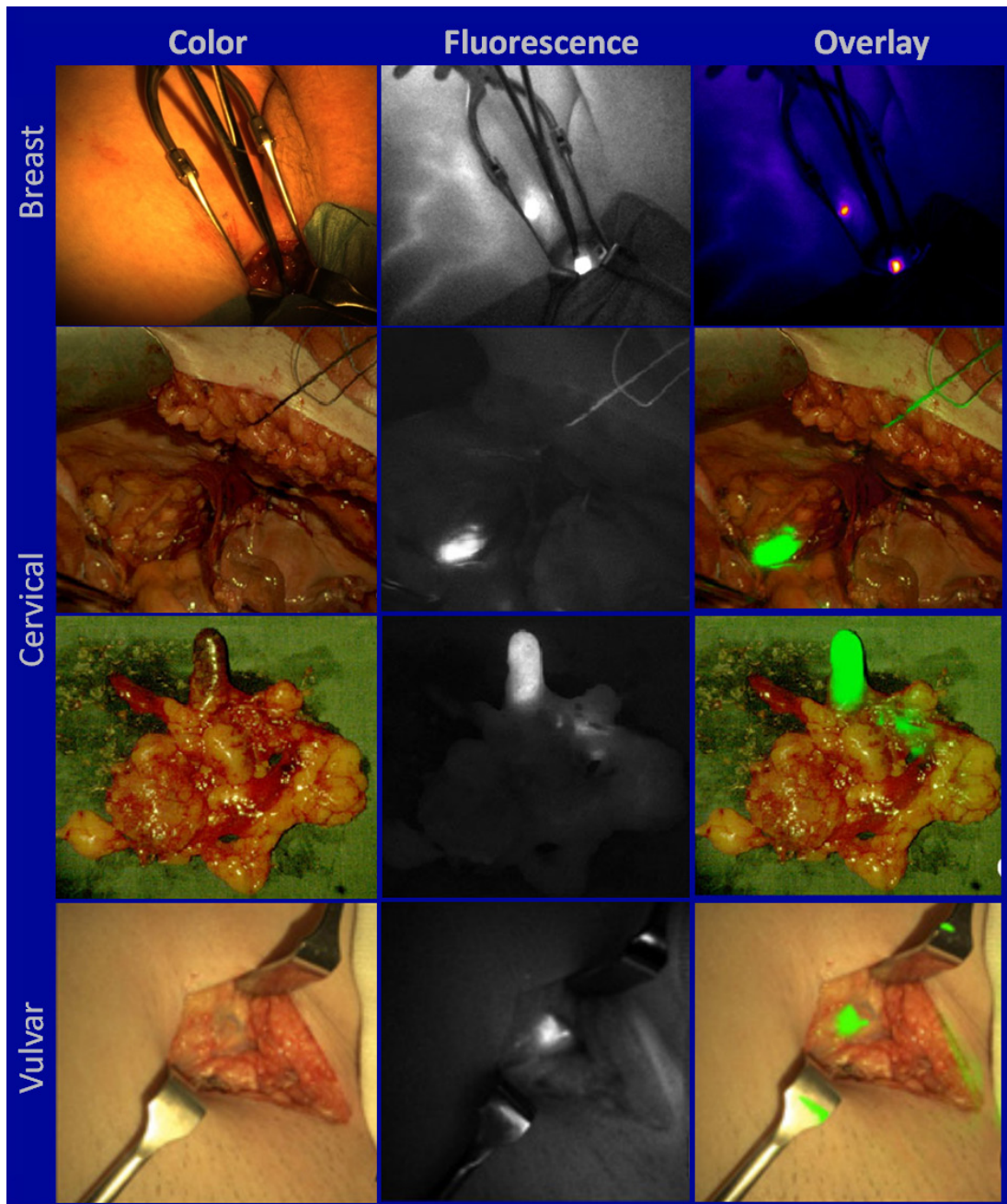


Figure 3-8. Color (left column), fluorescence (middle column) and false color fluorescence images (right column) during the SLN detection in breast, cervical and vulvar cancer patients. Ex vivo color, fluorescence and overlay imaging of a cluster of lymph nodes (third row from the top). Histopathological analysis showed that this fluorescent lymph node did not contain metastases.

Images of color, fluorescence and their overlay demonstrate the performance and potential of intra-operative fluorescence imaging. The SLN is clearly visible inside the surgical cavity, while at least two lymphatic channels can be identified in the surrounding area. In breast cancer patients, the injection of the ICG/patent blue mixture and its real-time forward movement through the lymphatic vessels towards the SLN was visible in most patients, probably due to the superficial location of the lymphatic system directly below the axillary skin. Unfortunately the second localized fluorescent signal shown in Fig. 3-8b is caused by the mistaken use of an intensely fluorescing surgical marker. The intensity of the signal in this case, however, did not interfere with the imaging procedure.

Fig. 3-8g-l demonstrate *in-vivo* and *ex-vivo* images from gynecologic oncology studies; cervix and vulva cancer respectively. Especially in the case of cervix cancer, the identification of SLNs can be complicated as they can be localized in the obturator fossa, the common and external iliac and on the junction of the right internal iliac and obturator fossa. Moreover bilateral SLNs are also possible in more than 59% of the patients (Darlin, Persson et al. 2010; Ogawa, Kobayashi et al. 2010), rendering the SLN identification and visualization even more demanding (Fig. 3-9). The fluorescent signal in the lymphatic vessels became visible typically within 30 seconds after the injection of ICG and patent blue, with the SLN generally appearing within 1–2 min. Lymphatic mapping was clearly discernible *in-vivo* in more than 50% of the cervix patients, while bilateral SLNs were detected in 3/10 patients. Overall, lymphatic mapping using fluorescence imaging was more straightforward in lean patients and somewhat more difficult in obese patients. Use of the intra-operative camera system in itself did not hinder the surgeon, and the surgical procedure was not extended with more than 30 min in the worst case due to imaging. More statistics for the individual patient categories are available at (Crane, Themelis et al. 2010; Crane, Themelis et al. 2011).

Overall, the results in all three cancer studies showcase that, compared with the

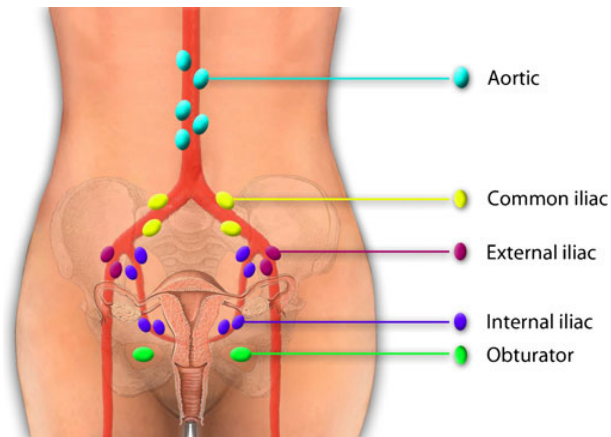


Figure 3-9. Lymph drainage of the cervix uteri is complex, bilateral, and can affect lymph nodes in several areas (Crane, Themelis et al. 2010). In our pilot study, nine SLNs were found. These were localized in the left obturator fossa (three), right obturator fossa (two), left external iliac (one), right external iliac (one), right common iliac (one), and on the junction of the right internal iliac and obturator fossa (one).

‘gold standard’ radiocolloid-gamma probe approach, the number of LNs identified *in-vivo* by fluorescence imaging are in the range from 60-90% (Crane, Themelis et al. 2010; Crane, Themelis et al. 2011). Importantly, none of the non-fluorescent LNs contained metastases. The lower detection rate compared with other studies (van de Lande, Torrenge et al. 2007; Ayhan, Celik et al. 2008; Frumovitz, Ramirez et al. 2008; Troyan, Kianzad et al. 2009; Yamashita, Katayama et al. 2009) in these pilot trials can be explained by a number of factors, i.e., patient characteristics and localization of lymph nodes, the learning curve concerned with the new technique and technical features of the camera system and the fluorescent agent.

The first reasons that could undeniably influence the successful LN detection rate are a) the learning curve involved with the intra-operative camera system and b) the correct injection of ICG. In one patient for example, a smaller abdominal incision prevented maximal exposure of all the LN basins during the imaging procedure, thus, hampering detection, while, in another case, a deep intra-cervical injection caused leakage of ICG into the pelvis that prevented the SLN detection. As the studies progressed and especially after gynecologic oncologists got more acquainted with the technique and the injection specifics,

the procedure was 'troubleshooted' and became more standardized. Furthermore, the limited range of movement of the camera head combined with small abdominal incisions caused difficulties in the detection of fluorescence in areas hidden inside the pelvis. A smaller, more flexible, preferably handheld camera system or even a laparoscopic system for intra-operative fluorescence imaging could overcome this problem. It should be noted that the clinical-grade imaging system was designed for generic intra-operative use and did not take into consideration the complex geometry of imaging and the lean/tilt angles of the camera head that are common in abdominal surgery. In any case, technical progress will undoubtedly lead to more ergonomic and clinically suited camera systems.

The most important limitation for the LN detection rate, however, appeared to be the tissue absorption of the excitation and emission light that prevented imaging of lymph nodes deeper than approximately 10 mm. This is sufficient for superficial LNs, but generally not enough to visualize lymph nodes covered by adipose tissue or masked by iliac vessels. For example, in one cervix cancer patient, intra-abdominal fat severely impeded the detection of fluorescence and only after the excision and upon *ex-vivo* dissection of the LN-tissue sample, could a blue and strongly fluorescent LN be discovered. Interestingly, this LN turned out to contain metastatic tumor tissue after histological examination.

Discussion

We conclude that SLN detection and mapping of the lymphatic system *in-vivo* in breast, cervix and vulva cancer patients using multispectral intra-operative fluorescence imaging are technically feasible without significant prolongation of the surgical procedure. Consistent with literature, we observed typical SLN detection rates in tumors smaller than 2 cm *ex-vivo* (Crane, Themelis et al. 2010). It is undeniable that more experience with the technique will lead to a higher detection rate of SLNs also *in-vivo*. The primary advantages of our multispectral fluorescence approach are the real-time tracing of lymph flow, the prevention of radioactivity and the one-step procedure that reduces patient distress.

Although these data are encouraging, however, the technique needs to be refined for full applicability in clinical practice in terms of sensitivity and specificity.

As hypothesized before the study, the SLN identification rate using fluorescence imaging was better than by using the discoloration approach alone and worse than by using the nuclear imaging approach, especially in the case of deep-seated lymph nodes that are covered by overlying muscle tissue or fat. Consequently, one important conclusion of these studies is that the SLN detection using near-infrared light will always be hampered by the physics of light distribution in tissue (absorption and scattering) and, therefore, it will be difficult for this approach of SLN identification to match or exceed the detection rates achieved with the radio-colloid method. Nuclear imaging has the advantage that high contrasts can be achieved even in deep-seated LNs as background levels are practically very close to zero, whereas background (auto)fluorescence will always be present and thus limit the overall contrast to no more than 5:1 or 10:1. Furthermore, real-time imaging imposes a high frame rate that further impedes the contrast build-up, since limited exposure time does not allow the captured light intensity to cover all the dynamic range of the imaging sensor. However, it can still be argued that future improvements (more sensitive imaging setups, stronger excitation light, fluorophores with higher quantum yield) could potentially allow intra-operative fluorescence detection of SLNs to replace the nuclear approach, at least in cases of superficial lymph nodes.

Nonetheless, the greatest significance of these studies lies in the identification of the major problems of the implementation of the multispectral technology in the clinical environment, in the experience gathered that will lead to next-generation more focused imaging systems dedicated to specific applications and in the step-up approach towards targeted imaging. Targeted fluorescent contrast agents may be fused with tumor-specific antibodies or substrates to be specifically directed at tumor cells. In this manner, intra-operative fluorescence imaging has great potential to radically alter the current practice of oncologic surgery.

3.5.2 Intra-operative imaging for tumor detection in ovarian cancer

Introduction

Of all gynaecologic malignancies, epithelial ovarian cancer (EOC) is the most frequent cause of death, both in the US (Jemal, Siegel et al. 2008) and in Europe (Gondos, Bray et al. 2009). The relative absence of a clear, distinctive clinical presentation/profile in early stages, combined with the lack of a reliable screening tool, often results in disease diagnosis at more advanced stages. The overall 5-year survival rate is 45% (Aletti, Gallenberg et al. 2007), and only 20-25% for stage III and IV (Winter, Maxwell et al. 2008; Ibeanu and Bristow 2010). Currently, cytoreductive surgery, followed by combination chemotherapy is regarded as the most effective treatment. The degree and efficacy of cytoreduction is one of the few prognostic factors that can be actively influenced by the surgeon. Improved staging and possibly survival could be achieved by better cytoreduction aided by an intra-operative, tumor-specific detection strategy that assists the surgeon by providing real-time feedback on residual malignant tissue. Radiologic approaches such as X-ray, CT, MRI or ultrasound have been considered for use in assisting the surgical procedure, but are, generally, not useful for intra-operative applications, as they do not provide tumor-specific contrast. By comparison, multispectral imaging combined with tumor-targeted fluorescent agents can enable the localization of lesions that are difficult or impossible to be detected by visual observation or palpation, and thus improve the efficacy of tumor tissue excision.

A promising target in EOC is the folate receptor alpha (FR- α), as several recent studies have indicated increased FR- α expression in 90-95% of patients with EOC (Kalli, Oberg et al. 2008; Markert, Lassmann et al. 2008). FR- α absence on healthy cells can lead to high tumor-to-background ratios and, for this reason, folate, as a ligand of FR- α , has already been conjugated to DTPA for SPECT/CT imaging (Mathias, Wang et al. 1998), to several PET tracers (Leamon, Parker et al. 2002) and to fluorescein for imaging in murine tumor models

(Kennedy, Jallad et al. 2003). In this study, we use folate conjugated to fluorescein isothiocyanate (folate-FITC). The resulting fluorescent probe has a peak excitation at 495 nm and a peak emission at 520 nm. The agent specifically targets the FR- α , after which it is internalized into the cytoplasm. We present results of the first-in-human use of intra-operative tumor-specific fluorescence imaging for real-time surgical visualization of tumor tissue in patients undergoing exploratory laparotomy for suspected ovarian cancer. Our hypothesis is that intra-operative imaging with tumor-targeted agents may improve staging and debulking efforts in cytoreductive surgery and thereby improve prognosis.

Results

Ten patients with a suspected ovarian malignancy, scheduled for a staging or debulking laparotomy, were included in this study, based on the following criteria: the ovarian mass, (and/or) the presence of ascites as diagnosed by ultrasound or CT scan, (and/or) the presence of an elevated CA-125 tumor marker. Among them, four patients were diagnosed with a malignant epithelial ovarian tumor and one patient with a borderline tumor, whereas five patients were diagnosed with a benign ovarian tumor (van Dam, Themelis et al. 2011). Additional immunohistochemical staining for FR- α revealed that out of the four patients diagnosed with a malignancy, two had a moderate FR- α expression, one had a strong FR- α expression, while no FR- α expression was observed in one patient. All patients completed the entire study, no serious adverse events (SAEs) were reported and although brief discomfort was reported in 4/10 cases, overall, the i.v. administration of folate-FITC was safe for the patients. Intra-operative imaging did not interfere with the standard surgical procedure, as its mean duration was 10 minutes (range: 4-36 minutes).

Multispectral imaging successfully detected fluorescence intra-operatively in all patients with a malignant tumor and FR- α expression, whereas in the patient with a malignant tumor but no FR- α expression and those with a benign or borderline tumor, fluorescence levels were comparable with the background tissues. Histological analysis

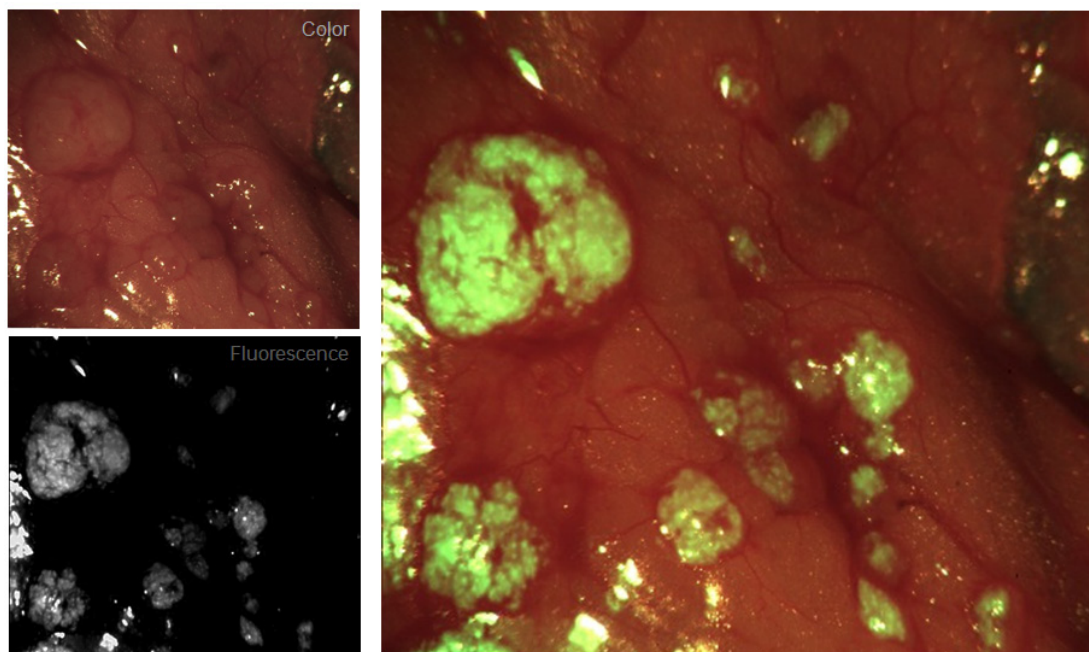


Figure 3-10. In-vivo detection of ovarian cancer with a targeted fluorescent probe (folate-FITC). Color, fluorescence and overlay images showcase the excellent tumor demarcation of the fluorescent probe and the high tumor-to-background ratio achieved. Overlay images provide helpful insights during image-guided surgery as small tumor deposits, that would otherwise be missed are now accurately detected.

confirmed that all highly fluorescent tissue samples contained tumor, whereas non- or low fluorescent tissue was free of tumor.

Fig. 3-10 depicts color, fluorescence and overlay images during *in-vivo* intra-operative fluorescence imaging. The zoomed-in images provide functional information of high resolution that would not be visible under visual inspection, especially for small tumor foci. A Supplemental Video shows a representative video recording during the image-guided surgical procedure for peritoneal sampling of fluorescent spots in a patient with stage III ovarian cancer using our developed intra-operative fluorescence imaging system. In this patient with high-grade serous carcinoma and strong FR- α expression, widespread tumor-specific fluorescence spots could be observed throughout the abdominal cavity. Furthermore, real-time image-guided excision of fluorescent tumor deposits with size smaller than 1 mm was feasible (Fig. 3-11). All fluorescent tissue was confirmed to be malignant by histopathology. Five surgeons, blinded for the surgical procedure and the final



Figure 3-11. *Ex-vivo* fluorescence imaging of an excised tumor spot from the peritoneal surface in color and fluorescence overlay from a patient with stage III ovarian cancer. Intra-operative imaging reveals the tumor borders with micron resolution. All fluorescent tumor spots were confirmed to be tumor-positive (H/E).

histopathological status of the removed tissue, were asked to identify tumor deposits based on the color and fluorescence images that are overlaid in Fig. 3-12. Interestingly, they detected four times more tumor deposits using the fluorescence image than by using the color photograph. Although the scoring was not accompanied by tactile information which is considered by many surgeons as an important feature in staging, this comparison is significant. The results suggest that at least the visual criteria of surgeons can be inadequate or restrictive and, thus, there is need for new supporting technologies. This comparison further demonstrated the potential of intra-operative imaging using targeted fluorophores.

In all cases, the *In-vivo* images were correlated with histopathological analysis and, overall, the fluorescent regions showed excellent correlation with histopathological findings. All excised samples were examined for FR- α expression and using the standard hematoxylin/eosin staining. Tissue slices were examined by conventional (Leica DM4000B,

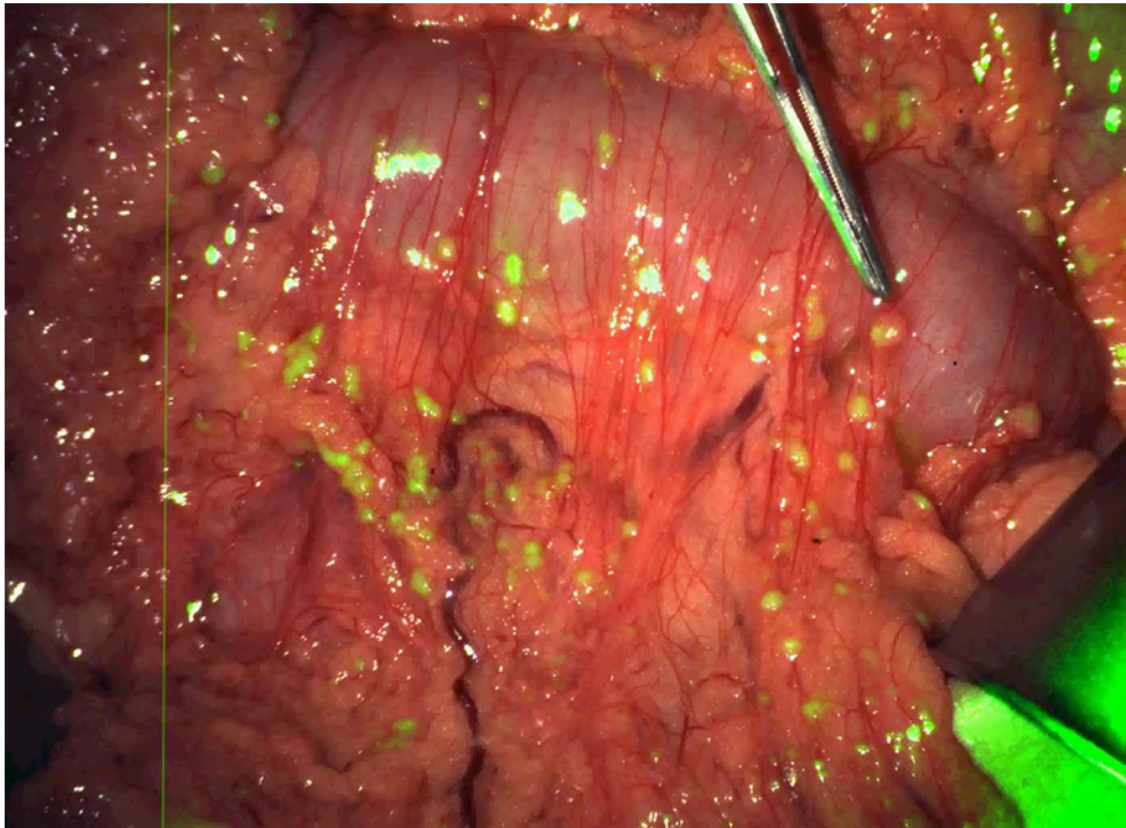


Figure 3-12.. In-vivo detection of ovarian cancer with a targeted fluorescent probe (folate-FITC). Macroscopic detection of peritoneal carcinomatosis. Single frame from a video recording shows an overlay image and showcases the In-vivo detection of ovarian cancer with a targeted fluorescent probe (folate-FITC). Color, fluorescence and overlay images showcase the excellent tumor demarcation of the fluorescent probe and the valuable information provided to the surgeon by the imaging modality.

Leica Microsystems BV, Rijswijk NL) and fluorescence microscopy (Zeiss Axioplan 2 with Axiocam camera system, Carl Zeiss BV, Sliedrecht NL). Representative examples of post-operative histopathological analyses are depicted in Fig. 3-13 for three different ovarian tumor stages. Fluorescence microscopy for folate-FITC showed a strong signal in all malignant tumors with FR- α expression and very low signal in FR- α negative (malignant or benign) lesions.

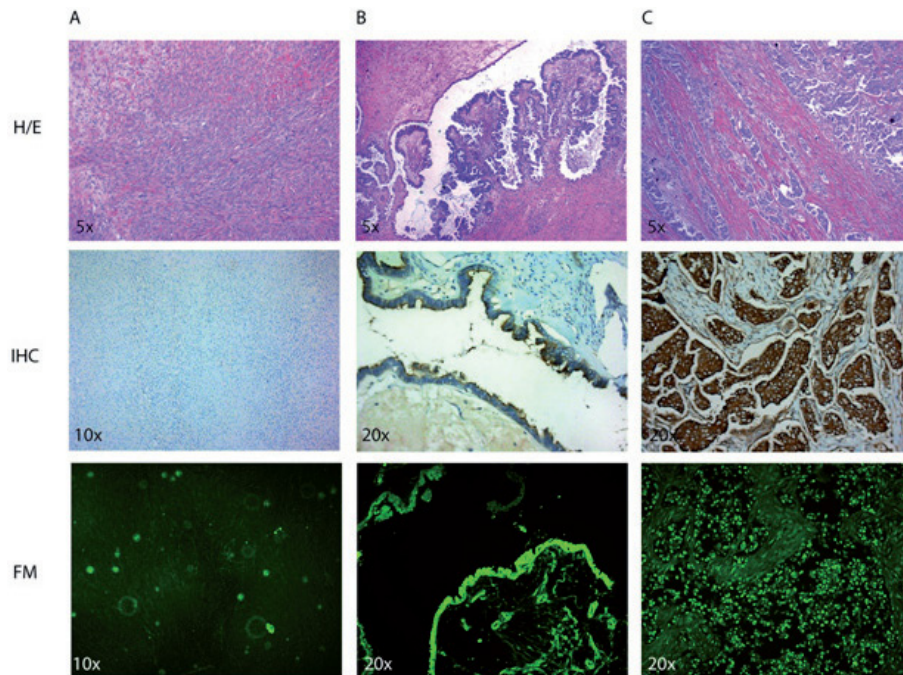


Figure 3-13. Microphotographs of 3 different ovarian tumors (fibrothecoma (A), borderline serous tumor (B) and high-grade serous carcinoma (C)). The upper row shows routine staining with hematoxylin/eosin. The middle row shows immunohistochemical staining for the folate receptor-alpha (FR- α). The lower row shows unstained slides, observed with fluorescent microscopy, to detect the intravenously administered folate-FITC. The fibrothecoma shows neither expression of FR- α nor binding of folate-FITC, which corresponds with the absence of fluorescence in the lesions visualized using the intra-operative imaging system. Both the borderline serous tumor and the high-grade serous tumor show epithelial expression of FR- α (with different levels) and binding of folate-FITC. (Image property of J Bart)

Discussion

In this first-in-human clinical trial, we demonstrated that intra-operative fluorescence imaging of a systemically administered FR- α targeted agent offers specific and sensitive *in-vivo* identification of tumor during the surgical procedure of patients with ovarian cancer and expression of FR- α . Our results illustrated that fluorescence imaging can discover and accurately visualize very small tumor deposits (<1mm) and showcased the potential applications of multispectral imaging in image-guided cytoreductive surgery. Furthermore, fluorescence-aided visual inspection of tissue provided up to four times better identification and localization of tumor spots than color-based visual examination in patients with strong FR- α expression.

However, the results presented here, demonstrated that it is of paramount importance to investigate the FR- α expression levels before including patients for imaging with folate-FITC, as only three out of the ten patients included in this study showed a significant FR- α expression. This patients' sample was statistically small, limited our ability to draw definitive conclusions and suggested that, the patient selection procedure needs to be more thorough and further refined. In order to identify patients suitable for FR- α targeted image-guided surgery, FR- α could be determined on either tumor cells in ascites or on tumor tissue excised during staging laparoscopy or primary surgery. A folate-targeted technetium scan could also be used pre-operatively to identify FR- α positive patients (Sega and Low 2008).

Furthermore, we were given the chance to get acquainted with clinical fluorescence imaging of contrast agents that emit light in the visible area of the spectrum and, for this reason, study more thoroughly the effect of the labeling fluorophore on the captured fluorescence image. Imaging and quantifying fluorescence activity in the visible is challenging as the optical properties of the tissues (absorption and scattering) have a considerable effect on the captured fluorescence intensity (a topic covered in detail in Chapters 6, 7 and 8). Underlying tissue characteristics could make the evaluation of clinical results troublesome as we later show, since it is possible for false positives and false negatives to arise during clinical fluorescence imaging. Although further development of fluorescent agents in the near-infrared will allow for identification of deep-seated tumors, based on the stronger penetration properties of near-infrared light, it is more important to develop methods that can accurately quantify and provide trusted measures of fluorophore concentration.

Overall, the major advantage of intra-operative tumor-specific fluorescence imaging above current standards is that it can guide the surgeon in debulking efforts, contributing, thus, to a more efficient cytoreduction. Since cytoreduction is a key aspect in the prognosis of many solid tumors with a peritoneal dissemination pattern, including ovarian cancer (Vergote, Van Gorp et al. 2008), a more complete debulking procedure may

have a beneficial effect on the patients' outcome and might ultimately improve overall survival rates; however this needs to be established by additional clinical studies.

3.6 Discussion and Conclusion

Since the original use of fluorescein for surgical imaging in 1947, different fluorescent dyes have been considered for human application, including porphyrins (Stummer, Götz et al. 1993; Stummer, Novotny et al. 2000), indocyanine green (Sevick-Muraca, Sharma et al. 2008) or fluorescein-albumin (Kremer, Wunder et al. 2000). Notable recent progress considers an emerging new generation of fluorochromes for clinical imaging. The clinical approval of hexylaminolaevulinate to stimulate the production of fluorescence PIX in bladder cancer (Ray, Chatterton et al. 2009) or its exploratory use with brain cancer surgery (Stummer, Stocker et al. 1998; Stummer, Reulen et al. 2003) points towards the use of molecularly specific biomarkers for disease identification during clinical procedures. Even wider potential exists by capitalizing on systemically administered engineered probes, such as labeled antibodies (Stangl, Gehrmann et al. 2011), peptides (Kuil, Velders et al. 2010), small-molecule peptidomimetics, and targeted nanoparticles (Vinegoni, Razansky et al. 2009) for *in-vivo* staining of disease related physiological and molecular states. Toward this direction, we have developed a clinical-grade real-time multispectral imaging system and demonstrated its clinical use for image-guided surgery in multiple first-in-human clinical studies for SLN identification and cancer detection. The imaging setup was easily introduced in the clinical practice, could image fluorophores of different emission spectra thanks to its flexible design and featured simple handling and time-efficient imaging procedures that did not demonstrate unwanted interference or prolong the surgical procedure. The image quality was very good and, more importantly, the *in-vivo* imaging results proved to have a good correlation with the 'gold standard' of *ex-vivo* histopathology. The system presented can work synergistically with other methods, such as intra-operative radiological or nuclear medicine methods to offer an integrated

solution of macroscopic non-invasive imaging combined with high resolution invasive imaging.

The prospective availability of more clinically approved fluorescent probes with enhanced *in-vivo* sensitivity and specificity to molecular disease markers makes fluorescence imaging a very appealing method for real-time intra-operative visualization of invasive tumor borders and local metastatic foci. Although at the time of the studies only fluorescein and indocyanine green were approved for clinical use in humans, the clinical approval of an additional near-infrared labeling fluorophore was announced during 2010 (<http://www.licor.com/bio/news/09.08.10.jsp>) and is expected to further facilitate the clinical translation of more near-infrared labeled bio-markers.

In summary, our data outline the development of a successful clinical multispectral imaging system and the application of intra-operative imaging in combination with non-specific and tumor-specific contrast agents. We presented, among others, the first in-human proof-of-principle study of a targeted contrast agent that could be used to improve palliative surgery in ovarian cancer patients. This study underlined the potential of intra-operative tumor-specific fluorescence imaging in staging and debulking surgery for ovarian cancer using systemically administered targeted fluorescent agents. The combination of optical imaging technologies with tumor-targeting strategies can shift the paradigm of surgical oncologic imaging, offering the unique opportunity to intra-operatively detect and quantify tumor growth and intra-abdominal spread. Of course, larger studies are needed to confirm our data and further elucidate the diagnostic (accuracy, sensitivity and specificity) and therapeutic value of the reported approach in larger series of ovarian cancer patients. In all, the successful implementation of our multispectral approach for quantitative real-time imaging and the continuous development of novel fluorescence correction strategies (Chapter 6, 7, 8) allow us to be optimistic that, in the near future, quantitative fluorescence imaging will become an important intra-operative technique for the enhancement of surgical vision.

Methods

Chapter 4: Theoretical background of photon propagation

Photon propagation in turbid media is a fundamental chapter of planar fluorescence imaging, since, ultimately, a recorded planar fluorescence image is nothing more than a “convolution” between the excitation and emission photons (light) with the local properties of tissue (absorption and scattering). Thorough understanding of the light-tissue interaction is therefore essential because, as we are going to show in Chapters 7 and 8, it is not atypical that disregarding the photon propagation theory can produce inaccurate distribution and erroneous quantification. In this Chapter we present a short introduction in the fundamentals of photon propagation and interaction with tissue and discuss how it can affect planar fluorescence measurements.

One approach for the estimation of photon propagation and distribution inside a volume of turbid medium is the use of analytical equations. The radiative transfer equation describes the interaction of photons as they propagate inside an absorbing and scattering medium (tissue) using the energy conservation law. The radiative transport equation (RTE) is mathematically formulated as follows (Arridge 1999):

$$\frac{1}{c} \frac{\partial L(\vec{r}, \hat{s}, t)}{\partial t} + \nabla \cdot L(\vec{r}, \hat{s}, t) \hat{s} = -(\mu_a + \mu_s) L(\vec{r}, \hat{s}, t) + \mu_s \iint_{4\pi} L(\vec{r}, \hat{s}', t) f(\hat{s} \cdot \hat{s}') d\hat{s}' + Q(\vec{r}, \hat{s}, t)$$

, where $L(\vec{r}, \hat{s}, t)$ is radiance [$\text{W}/\text{m}^2\text{sr}$] at position \vec{r} at time t propagating along the unit direction vector \hat{s} , μ_a and μ_s are the absorption and scattering coefficients of the medium and c is the speed of light inside the medium. The term $f(\hat{s} \cdot \hat{s}')$ presents the probability of change in photon propagation direction from \hat{s} to \hat{s}' due to scattering and $Q(\vec{r}, \hat{s}, t)$ is the photon power [$\text{W}/\text{m}^3\text{sr}$] introduced per unit volume at position \vec{r} in the direction \hat{s} . Simply put, according to (Knyazikhin and Myneni 2004), the RTE can be written as $dN = -\text{absorption} - \text{“outscattering”} + \text{“inscattering”} + \text{emission}$, where dN is the number of photons change, “outscattering” describes the elastic scattering directing a photon outside of the unit volume and “inscattering” describes the elastic scattering directing a photon inside the unit volume. After integration over all solid angles, the RTE can be written in a simpler form:

$$\frac{1}{c} \frac{\partial \varphi(\vec{r}, t)}{\partial t} + \nabla \cdot \vec{j}(\vec{r}, t) = -\mu_a \varphi(\vec{r}, t) + S(\vec{r}, t)$$

, where $\varphi(\vec{r}, t) = \iint_{4\pi} L(\vec{r}, \hat{s}, t) d\Omega$ is the photon fluence rate [W/cm^2], $\vec{j}(\vec{r}, t) = \iint_{4\pi} L(\vec{r}, \hat{s}, t) \hat{s} d\Omega$ is the photon flux [W/cm^2] and $S(\vec{r}, t) = \iint_{4\pi} Q(\vec{r}, \hat{s}, t) d\Omega$ is the source term [W/cm^3].

Mathematically, the use of the RTE equation for tissue measurements imposes limitations. Therefore, approximations have been developed to convert the transport equation to more convenient and efficient forms (P_N approximation, diffusion equation, etc.). Nevertheless, analytical solutions can still only be used for specific and very simple geometries.

An alternative method to describe photon propagation is to model the light-tissue interaction. Monte Carlo (MC) simulations are widely used as modeling tool in order to efficiently solve a variety of physical and engineering questions with different grades of complexity. The Monte Carlo method uses uniformly distributed random variables to sample generally non-uniformly distributed variables. As MC is statistical by nature, it requires large number of iterations to become accurate (also depending on the complexity of the problem).

Although the algorithm that was used in this work for the Monte Carlo simulation of photon propagation is not the only available, it combines computing efficiency and thorough modeling of the light-matter interaction and has been proven suitably accurate (Wang, Jacques et al. 1995). The MC method begins by launching a photon (packet) with a weight W and it follows its interaction with tissue until it is reflected or transmitted at the boundaries of the volume of interest, or until it is absorbed inside this volume. The size of the distance each photon travels inside the medium (tissue) before an interaction occurs is variable and its probability density function follows Beer's law (exponentially higher probability of shorter travel distances). If ξ is a uniformly distributed random variable, then the step size Δs is modeled as:

$$\Delta s = -\frac{\ln(\xi)}{\mu_t}$$

, where $\mu_t = \mu_a + \mu_s$ is the interaction coefficient. After the photon has travelled through the medium, it is absorbed and scattered. For the absorption, a fraction ΔW of the current photon weight W is appointed at the specific volume area: $\Delta W = \frac{\mu_a}{\mu_t} W$. For the scattering, two angles are modeled; the azimuthal angle ψ is uniformly distributed over $[0, 2\pi]$: $\psi = 2\pi\xi$, whereas the deflection angle θ is modeled as:

$$\cos(\theta) = \begin{cases} \frac{1}{2g} \left\{ 1 + g^2 - \left[\frac{1 - g^2}{1 - g + 2g\xi} \right] \right\}, & \text{if } g \neq 0 \\ 2\xi - 1, & \text{if } g = 0 \end{cases}$$

, where g is the anisotropy factor, with $g = 0$ denoting isotropic scattering. Until one of the above mentioned conditions (reflection or transmission at the volume borders or total internal absorption) is met, the photon travel through the medium is described repeatedly by these consecutive “steps”: travel distance, absorption and scattering.

The interaction between photons and tissue does not only determine the photon travel and diffusion inside tissue. Planar fluorescence imaging is also influenced, since the beam of photons, illuminated to excite a fluorophore, will interact with the medium it travels through and distribute depending on the local optical properties of tissue. In the same way, the emitted fluorescence photons will, once again, have to pass through the tissue volume before they can be captured by an imaging device. The same stands also for autofluorescence measurements. Although the sampling depth of planar fluorescence imaging is usually not more than a few millimeters in tissue, those effects can be significant (depending on the local tissue properties) and induce errors in the fluorophore quantification. Therefore, in tissues with inhomogeneous optical properties, the recorded fluorescence intensity does not exhibit a linear dependence on fluorophore concentration; it rather reflects a distorted relation between the fluorophore concentration and the local absorbers and scatterers concentration. Although not always feasible, we show that Monte Carlo modeling of a physical problem for fixed geometries can be beneficial (Chapter 7). Furthermore, even in the case of experimental algorithms (Chapter 8) the photon propagation theory still is an essential prerequisite to qualitatively understand light-matter interaction and develop methods to correct inaccurate fluorophore quantification.

Chapter 5: Monte Carlo simulation method for *ex-vivo* fluorescence imaging

5.1 Problem

Modalities that image fluorescence in block samples should ideally image only the surface of the exposed tissue. However they are by definition bound to be affected by out-of-plane signals. Usually these systems image the tissues under investigation multiple times for every millimeter. Our most commonly used imaging protocol for instance captures fluorescence images every 125 μm . For such imaging systems, thus, the excitation light penetrates multiple imaging planes and excites fluorophores and signals not only on the surface plane but also deeper inside the sample. As a result the fluorescence photon distribution that is in the end captured by the camera sensor is volumetric rather than two-dimensional. The use of light in the far-red and near-infrared area of the spectrum further

complicates the image acquisition since it well known that light with longer wavelengths penetrates deeper inside biological tissue (up to a few millimeters depending on the wavelength and tissue type) compared with light of shorter wavelength. Consequently out-of-plane photons have a considerable effect on image quality as they interfere with surface photons. In this way false signals can reach the surface of the imaged sample and be falsely interpreted as to their location inside the block sample volume. Additionally the sub-surface fluorophores can cause blurring both in the cross-sectional images and in the reconstructed 3D volumes. This “blurring” ultimately is the main limiting factor for the resolution achieved by such implementations especially on the z-axis (i.e. perpendicular to the exposed tissue surface).

To our knowledge this issue has raised until present only limited attention. A previous attempt to face this problem (Wilson, Roy et al. 2008) takes into account only the depth between consecutive imaging planes in order to decrease the out-of-plane photon contribution. However the photon distribution inside turbid tissue depends not only on the total path length that a photon travelled (between consecutive imaging planes) but also on the underlying optical properties of the tissues it went through. Our approach goes, thus, one step further and fully simulates the photon diffusion inside tissue by imposing different optical properties at every pixel of the acquired fluorescence image. In this way we take into consideration both total path length and the optical properties of the travelled tissue for out-of-plane photons.

For this purpose a Monte Carlo method, a well-established method for photon transport analysis in turbid media, is used to simulate how photons distribute inside the volume of interest. The Monte Carlo approach (Wang, Jacques et al. 1995) is based on macroscopic tissue optical properties and builds on the hypothesis that these also extend in small units of tissue volume. It simulates the transport of infinitely narrow photon beams perpendicularly to a multi-layered tissue sample. The most important parameters that need to be defined and mostly influence a Monte Carlo simulation are the tissue layer(s) thickness and its (their) optical properties, namely the absorption coefficient μ_a , the

scattering coefficient μ_s , and the anisotropy factor g . Being statistical in nature, the method requires multiple independent measurements of photon paths until it yields a meaningful result. The achieved precision and spatial resolution depend therefore on the number of individual photons (or photon packets) simulated and thus inevitably require significant computation time, especially for three-dimensional geometries.

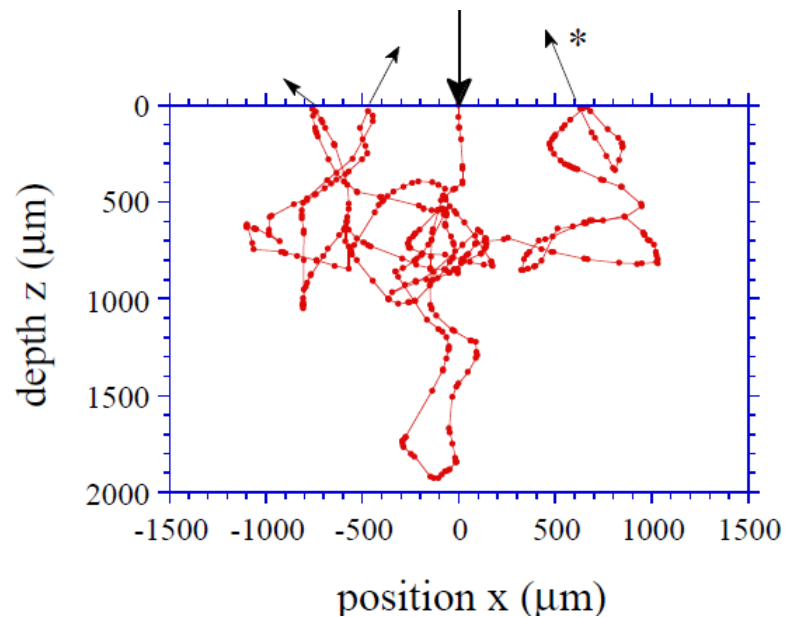


Fig. 5-1: Monte Carlo simulation of a travelled photon path. The thin red line shows a Monte Carlo simulated movement of one photon through a homogenous medium. In this case there is diffuse reflectance at the 3 sites where photons exit the medium but no diffuse transmittance. The internal photon absorption attributed to every photon-tissue interaction site (red knot) is the photon weight difference $\Delta W=W(i+1)-W(i)$ caused by local photon absorption. Image taken from (Wang, Jacques et al. 1995).

After all photon packets have been simulated, the Monte Carlo method provides statistical measures for diffuse reflectance, transmittance and internal photon absorption for the simulated tissue volume.

5.2 Method description

In order to correct for out-of-plane fluorescent contributions, a nearest-neighbor image algorithm (Sarder and Nehorai 2008) is used that can be formulated as follows:

$$I_{i_corrected} = I_i - a \cdot MC_{processed}(I_{i+1})$$

, where I_i is the fluorescence image at a certain imaging plane we wish to correct, I_{i+1} is the next fluorescence image at a plane deeper inside the tissue (typically 100–200 μm deeper, depending on the imaging protocol used), $MC_{processed}(I_{i+1})$ is an image calculated by assuming the photon propagation of image I_{i+1} through the tissue, using the Monte Carlo simulation method, and a is an attenuation factor. The correction is performed after the whole mouse has been sectioned and after all sets of images have been acquired. It uses thus the *a posteriori* information of fluorescence distribution inside the whole tissue volume and is best illustrated with Fig. 19. Let I_i be the fluorescence image at the i -th plane to be corrected. Then, the image at the $(i + 1)$ -th plane (highlighted with brown) represents all signals from sub-surface planes that are excited during the acquisition of the i -th image. The fluorescence intensity values per pixel of the $(i + 1)$ -th image are

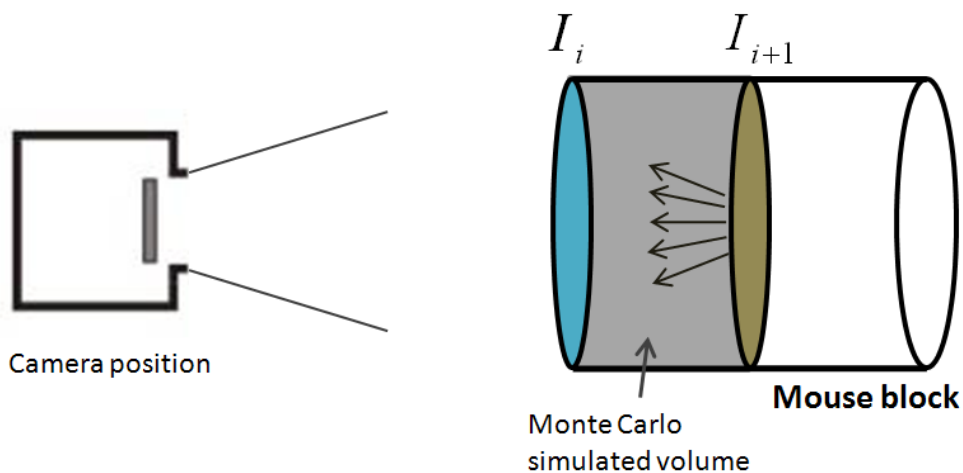


Figure 5-2. Schematic of the out-of-plane fluorescence contributions. Due to the ‘deep’ penetration of the near-infrared excitation light, sub-surface tissues are also excited. The fluorescence photons travel reach the sample surface and provide

deteriorate the system's accuracy. The Monte Carlo method simulates the photon diffusion of the $(i + 1)$ -th fluorescent image in order to correct for out-of-plane photons captured at the i -th fluorescence image.

subsequently fed to the Monte Carlo simulation that models the photon pathways through the tissue volume between the two imaged surfaces (gray shaded area). The optical properties for every pixel are defined as follows. We assume a homogeneous medium, whose absorption coefficients at every pixel of the volume of interest are derived from the reflectance image at the excitation wavelength (termed "intrinsic"). The scattering coefficients are either considered constant (typically $\mu_s=10 \text{ cm}^{-1}$) or can be retrospectively assigned using segmentations of different organs/structures and appropriate bibliography (Cheong, Prahl et al. 1990; Alexandrakis, Rannou et al. 2005). The anisotropy factor is kept constant at $g=0.9$, which is generally considered close to reality for biological tissues. Once the Monte Carlo simulation is complete the resulting diffuse transmittance represents how the out-of-plane photon distribution has been projected onto the i -th plane. It is termed $MC_{processed}(I_{i+1})$ in Equation 1.1. Finally, the sub-surface contribution is scaled and subtracted from the original I_i fluorescence image. In order to account for both out-of-plane signal suppression and preserved dynamic range in the corrected image, α was experimentally chosen at 0.45. The typical number of simulated photon packets is $n=100,000$. Examples for the application of the Monte Carlo out-of-plane fluorescence correction are presented in Chapter 7.

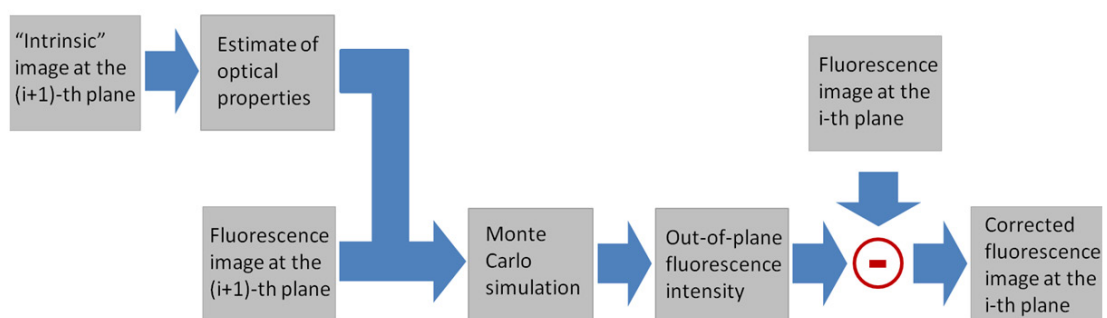


Figure 5-3. Schematic/flowchart of the Monte Carlo correction algorithm.

The Monte Carlo simulations for multi-layered tissues are referenced in detail by Wang and Jacques (Wang, Jacques et al. 1995) and the method described has been written in Standard C. However a freely available version of the same algorithm was found online (<http://www.mathworks.com/matlabcentral/fileexchange/8754-monte-carlo-simulation-for-photon-migration-inside-biological-tissue>) in MatLab and was used. It was consequently altered in order to suit this application, namely to accept user-defined or image-derived optical properties. The flowchart of the algorithm is presented in Fig. 20.

Chapter 6: Fluorescence absorption and scattering enhanced decomposition

6.1 Problem

Clinical decision making is most commonly corroborated by visual inspection of tissue in many diagnostic and/or therapeutic procedures, in particular in the various endoscopic and surgical procedures performed daily in medical environments. Typically, human vision based detection relies on discolorations and anatomical changes from the common appearance of healthy tissues. Enhancing contrast using extrinsically administered or tissue-intrinsic fluorescent moieties is a potent strategy for advancing the clinical paradigm by improving the observation outcome and interventional procedures. Indeed, fluorescence imaging of humans has been considered for more than half a century using fluorescein for tumor identification during surgery (Moore 1947). In particular, the extrinsic administration of novel fluorescent agents with the ability to identify specific molecular entities associated with tissue structure, function or disease can enable the visualization of a wealth of biological processes otherwise invisible to the naked eye.

Planar epi-illumination fluorescence imaging is an ideal modality for enhancing surgical and endoscopic imaging as it directly relates to the physician's vision. An ideal fluorescence clinical imaging strategy would provide high contrast between healthy and diseased tissue. Furthermore the fluorescence intensity would be proportional to the targeted lesion/feature concentration or mass. Thereby, the intensity of the fluorescence signal would be indicative of the presence and possibly severity of disease, providing for example cancer demarcation and staging or grading.

Planar epi-illumination (photographic) fluorescence imaging (EFI) refers to expanding a light beam onto the tissue surface, using light of spectral content that optimally matches the absorption spectral band of the fluorochrome of interest. Fluorescence photons from the volume illuminated are then detected by a charge-coupled device (CCD) camera. The difference of EFI with conventional photography is that the light incident on the tissue surface establishes a photon distribution within a few millimeters within tissue, which in turn excites the fluorochromes present. Therefore, EFI collects volumetric and not purely surface photons as it is the case in conventional photography. Since focusing cannot be achieved within tissue, the images are nevertheless obtained by focusing the camera on the tissue surface, even if scattered sub-surface photons are also detected. The collection of scattered fluorescence photons leads to the slightly lower resolution appearance of the fluorescence images captured, compared to color images of the same field of view of tissue, that make use mainly of back-reflected photons.

Even though EFI appears straightforward to interpret, preclinical and clinical studies have shown fundamental limitations, which compromise accurate fluorescence quantification when planar epi-illumination imaging methods are employed (Steinkamp and Stewart 1986; Bogaards 2006; Bradley and Thorniley 2006). Perhaps the most important is that the fluorescence images captured do not reflect the true fluorochrome bio-distribution. Instead, they represent a mixed contribution of fluorochrome bio-distribution and tissue optical properties, i.e. absorption and scattering. In this way, variations of tissue optical properties for example will modify the captured fluorescence image, even if the

fluorochrome concentration remains unaltered. Tissue absorption variations typically relate to oxygenated and deoxygenated haemoglobin (HbO₂ and Hb) concentration differences between tissues or lesions whereas tissue scattering variations relate to cellular density and morphology diversity among them.

As a result, epi-illumination fluorescence imaging of tissues can be compromised by the spatial variation of the tissue optical properties. For example, a bright lesion on an EFI image could be the result of increased fluorescence concentration or lack of haemoglobin in that structure. Similarly a dark lesion could be interpreted as a lesion of low fluorescence accumulation or a highly vascular lesion whereby fluorescence photons are internally absorbed by the highly concentrated haemoglobin molecules. Therefore, highly absorbing lesions, such as highly and densely vascularized tumors, may appear darker than surrounding less-absorbing tissue, even if these tumors contain larger amounts of fluorochrome compared to their surroundings. Scattering also modifies signals further, whereas contributions from intrinsic tissue fluorochromes and signals emanating from different depths further complicate the ability to quantify extrinsically administered fluorescence activity from epi-illumination fluorescence images.

Therefore clinical decision making based on EFI can be inaccurate, challenged by false negatives and false positives, since EFI does not uniquely identify and measure the underlying fluorescence bio-distribution. The non-uniqueness is easily understood theoretically, by reviewing the mechanisms of fluorescence generation and photon propagation in tissue. In the Data analysis section we experimentally demonstrate that false negatives and false positives are evident on animal and human imaging studies using fluorescent agents. These findings demonstrate that, despite the simplicity of application, the utilization of EFI in clinical environments can have potentially serious implications as efficacy limitations could potentially endanger the corresponding regulatory approvals of the technology due to inaccurate performance.

Correspondingly we introduce a novel approach termed “Fluorescence Absorption and Scattering Enhanced Decomposition” or “FASSED”, which has been developed to account for the effects of optical properties and restore accuracy on fluorescence images, without compromising the attractive operational characteristics of EFI, namely portability, small form factor and real-time operation/feedback. The method reduces the uncertainty of EFI images and retrieves true fluorochrome bio-distribution.

6.2 Literature Review

The inaccuracy in true fluorophore concentration quantification has been well known in the field of optical and fluorescence spectroscopy at least since the late 1980s (Steinkamp and Stewart 1986). Depending on the fluorophore used –extrinsic or intrinsic– and the area of the spectrum of the application different methods have been applied to account either for tissue auto-fluorescence (from intrinsic tissue fluorophores such as collagen or NADH) or for tissue absorption and scattering. Hence, there are potentially several methods to measure absorption and scattering spectroscopically including the use of time-resolved or frequency domain techniques. Still, time or frequency-domain methods come with varying degrees of accuracy depending on the implementation and generally lead to complex and expensive instrumentation. In contrast, in planar imaging applications, correction methods have not yet been fully explored and only relatively few approaches have been developed in order to resolve true fluorescence concentration; among them even fewer are suitable for real-time (clinical) imaging applications. Of particular interest is the review of correction techniques by (Bradley and Thorniley 2006) and the detailed comparison of correction methods for imaging applications by (Bogaards 2006).

Usually the most common approaches suitable for real-time imaging have been single (or more rarely double) ratiometric and can be roughly divided in two categories. In the first, the corrected measures are derived from single (or double) ratios between two (or

four) fluorescence images. These are captured either by exciting the fluorophore of interest at multiple wavelengths or by imaging the fluorescence emission at multiple wavelengths or both. In the second category are methods that derive ratios between fluorescence and reflectance images at the excitation and/or emission wavelengths (Ntziachristos, Turner et al. 2005; Bogaards 2006).

The main disadvantage of multiple fluorophore excitation is that this procedure is *de facto* time-consuming and leads to “time-sharing” implementations. This term suggests that corrected values are only available after multiple fluorescence measurements have been processed. Therefore an ever increasing number of measurements results in an ever decreasing frame rate or alternatively an ever increasing noise level (if we consider constant frame rates). On the other hand, multiple ratios at the emission spectrum of the fluorophore usually take into account also parts of the spectrum with very low or none fluorescence emission. Such measurements, in turn, require generally higher exposure times, leading thus once more to reduced frame rate. Fluorescence frame repetition rate is of utmost importance in surgical environment as it a) allows more natural feedback to the surgeon, b) captures more easily transient phenomena like bolus fluorophore injections and c) provides trustable, clear images free of motion artifacts.

On the contrary, in the fluorescence-reflectance methods the surplus of images required for the correction is parallel and independently captured, inducing thus no time penalties on the highest possible frame rate or the dynamic range of the captured images. Still, in the case of fluorescence-reflectance ratios, the most significant limitation arises from the limited amount of reflectance information that is captured as most of the methods utilize only one (or more rarely two) reflectance image. In this perspective FASED can be thought of as a generalization and improvement of fluorescence-reflectance methods as it utilizes and independently analyses multiple reflectance images in order to derive corrected fluorescence metrics/images.

Another perspective for the categorization of correction techniques is their suitability to specific applications. It is evident that fluorescence ratiometric techniques can potentially distinguish and correct for tissue optical properties or for intrinsic fluorophores, whereas fluorescence-reflectance approaches deal only with rectifying tissue absorption and/or scattering. Hence FASED is also not suited for applications where the most challenging effect on the fluorescence image is caused by tissue-intrinsic fluorophores. In the clinical studies presented in this work, though, imaging was performed mainly in the near-infrared range of the spectrum, where tissue auto-fluorescence is minimal. Additionally the clinical imaging system was designed (filters and lasers selection) so that tissues are not (or minimally) exposed to ultraviolet (UV) light that is known to excite tissue auto-fluorescence.

6.3 Method description

The FASED correction method aims to decompose the two major tissue properties that mostly affect a planar epi-illumination fluorescence image, namely tissue absorption (caused by blood and in particular haemoglobin) and scattering (caused by different tissue types and morphologies). The idea behind the FASED decomposition is that human color vision can discriminate well and with specificity between structures/areas of biological tissue with different color appearance. For instance it is straightforward to argue that the human eye can accurately differentiate between areas of high vascularization and red color appearance, areas of high scattering and white color appearance and a series of different hues and color tones in between. In other words spectral reflectance imaging can be a promising approach in distinguishing between the different tissue constituents based on their spectral signature. Tissue absorption and scattering, also depending on their prevalence and intensity/concentration, contribute differently to the captured fluorescence intensity. This decomposition allows us, thus, to study every component independently and calculate its particular effect on the captured fluorescence (EFI) image.

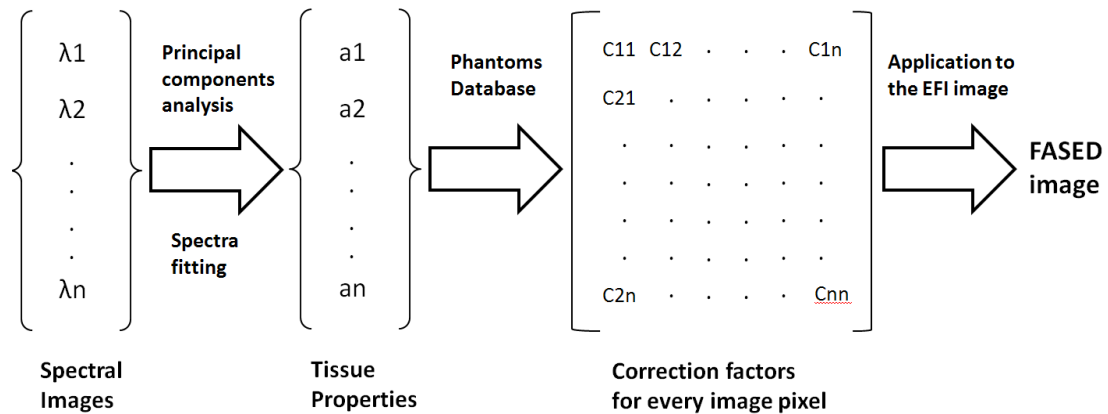


Figure 6-1: Schematic/flowchart of the FASED image processing algorithm. Multiple spectral reflectance measurements are used to derive tissue-specific properties (absorption and scattering). Thereafter, the effect of every tissue constituent based on previous phantom experiments is calculated and a correction factor is determined for every image pixel.

The FASED correction method requires multiple spectral reflectance measurements and compares them with known spectra and experimental phantom measurements to create a per-pixel corrected image. The initial processing step is implementing principal components analysis in order to decompose the acquired spectral reflectance images $\lambda_1, \lambda_2, \dots, \lambda_n$ into components that yield meaningful and significant physical properties of tissue (haemoglobin, fat, etc). This step transforms our measured reflectance spectra from the $\lambda_1, \lambda_2, \dots, \lambda_n$ space to a different one with less dimensions, not necessarily the space of the traditional pca (the one of orthogonal components wherein the data have the highest variation), but rather to a space of more meaningful physical dimensions (haemoglobin reflectance spectrum, scatterer reflectance spectrum, etc). Using experimental reflectance and fluorescence measurements from a series of deterministic phantoms with various optical properties as reference (a subset is shown in Chapter 8, Fig.8-1) we calculate the effect of every tissue component to the acquired EFI image based on its occurrence and magnitude. The use of simple deterministic phantoms is of major importance as they allow us to study the effect of tissue optical properties in different cases, i.e. using different absorption and scattering concentrations and with fluorophores that emit in different areas of the visible and near-infrared spectrum. Finally a matrix with correction factors for every image pixel is created and applied to the recorded fluorescence

intensity image (EFI) in order to produce the FASED image. In the images shown here three reflectance images at the visible range were used to build the fluorescence correction matrix, but the FASED method can obviously be generalized using more spectral measurements and therefore a “more” over-determined system for increased accuracy.

The method can be applied both to scanning and real-time multispectral fluorescence imaging systems. In the former case, spectral reflectance measurements can be acquired by scanning a sample with multiple narrow band pass filters. However, since the studies presented herein were performed on a real-time multispectral system, our approach was somewhat different. In this case, the spectral analysis was based on the RGB properties of the color images collected by the clinical-grade imaging system (described in detail in Chapter 3) employed in a series of pre-clinical and clinical studies. This approach cannot characterize absolute tissue optical properties, as it is the case in time or frequency domain methods, but suffices for decomposing their contributions, as required by FASED.

Examples for the application of the FASED correction method in phantoms, ex-vivo and in-vivo animal experiments as well as in clinical imaging of humans are presented in Chapter 8.

Data Analysis

Chapter 7: Application in *ex-vivo* fluorescence images

This Chapter presents various cases of application of the previously described algorithms of Chapter 4 and 5 in *ex-vivo* planar fluorescence imaging examples. First, in Chapter 6.1 Monte Carlo method examples for out-of-plane fluorescent contributions correction are demonstrated in multispectral cryoslicing images, while afterwards, in Chapter 6.2, planar fluorescence images of phantoms and cryoslicing images showcase the performance of the FASED algorithm.

7.1: Application examples of Monte Carlo based out-of-plane fluorescence correction

To demonstrate the performance of the correction algorithm employed, a cross-sectional image of a healthy IntegriSense injected mouse was chosen as it featured a strong and well-defined out-of-plane fluorescent signal in the lung. By visual inspection of the full 3D stack of cryoslicing images, it was deduced that the actual fluorescing cavity was

situated 250 μm deeper inside the tissue than the actual section displayed in Fig. 7-1. Although the origin of the signal is ambiguous, it can be probably attributed to local leaky microvasculature or a small injury during animal handling that induced this accumulation, as the imaged animal was healthy and the area shown in remote distance from structures that were defined as IntegriSense accumulation sites. Color, fluorescence and corrected images show both the original CCD camera field of view and a “zoomed-in” detail view illustrated by the gray outline.

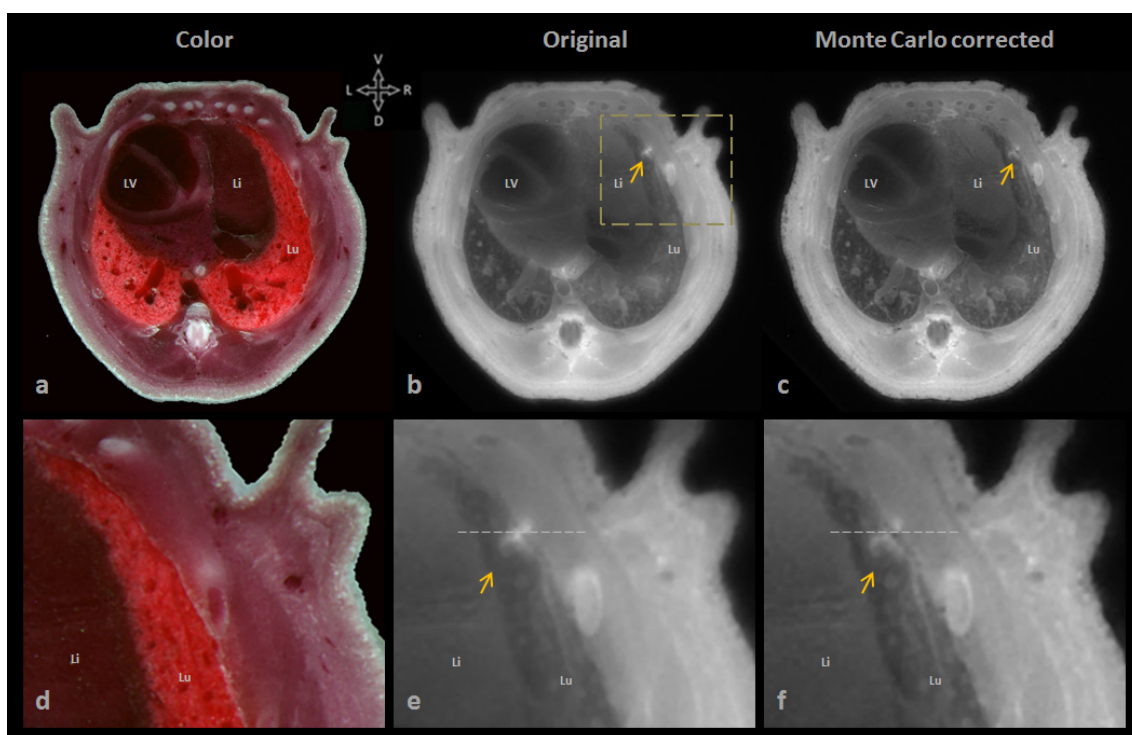


Figure 7-1. Out-of-plane fluorescence correction example. Color (a) and fluorescence (b) images of a cross-section in an IntegriSense-injected healthy mouse. The area under examination which is highlighted in b has been magnified before (c) and after the correction (d) for clarity. L left, R right, D dorsal, V ventral, Lu lung, Li liver, LV left ventricle of the heart.

It is notable in Fig. 7-1 that after the application of the correction algorithm, the localized diffuse signal is greatly suppressed, while the rest of the image remains virtually unchanged. Due to the nearest-neighbor approach we employed, *a posteriori* information about the sub-surface fluorescent signal is used in order to resolve its location and amplitude. Additionally local optical properties allow the Monte Carlo method to accurately

simulate the propagation of the sub-surface signals through tissue. The purpose of this processing algorithm is not to completely eradicate the entire out-of-plane signal as this would result in a fluorescence image of poor dynamic range but rather to keep the initial contrast of the picture and selectively restrain the major unwanted out-of-plane signals. Simultaneously, one can observe that apart from the sub-surface signal suppression, the corrected fluorescence image appears crisper, its structures are more clearly outlined and the apparent image resolution is higher. Especially the fluorescence coming from the spinal cord and from inside the lung can be a lot better delineated at the corrected image, while local fluorescence “hot-spots” (arrow) are noticeably easier to be distinguished. Once again it was diffuse fluorescence signal excited from inside the sample that contributed to this image “blurring”, as scattered out-of-plane photons reached the surface of the sample. The Monte Carlo method takes them also into account and thus produces a corrected image that reveals the true fluorescence levels of the imaged surface.

In Fig. 6-2 the fluorescence intensity along a common line in the original and the corrected image is plotted. The original fluorescence counts have been arbitrarily normalized with their highest value, while the corrected plot has been scaled to fit the original for comparison purpose. The selected line passes directly through the out-of-plane signal location and is drawn in Fig. 6-1. Clearly, the real fluorescence bio-distribution along this imaging plane is rectified and it is now minimally affected by sub-surface contributions. Furthermore, the fluorescence signal intensities from the cavity surroundings (rest of the lung, muscle tissue) are obviously not at all influenced by the correction procedure and therefore have a similar pattern as in the original fluorescence image. Thus it is demonstrated that our method manages to keep the contrast of the initial image, while selectively restraining out-of-plane signals.

The effect of image blurring due to diffuse sub-surface photons can be easily detected also in the reconstructed sagittal (and generally non-vertical) planes.

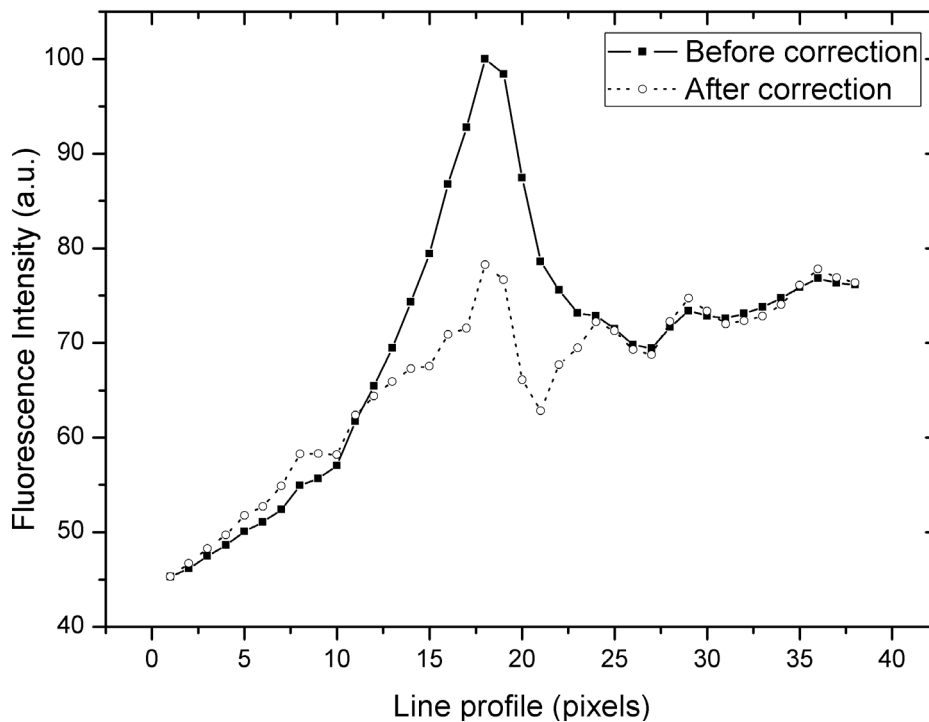


Figure 7-2. An intensity plot through the line that is indicated in Fig. 6-1 (arrow is plotted here before (solid line) and after the Monte Carlo correction (dashed line). The graphs showcase the algorithm’s ability to selectively suppress out-of-plane signals and to preserve the local image contrast.

In Fig. 6-3 we show a “virtual” slice of a subcutaneous tumor bearing mouse. Although bigger structures look similar in both the original and the corrected image, the bigger differences between them lie in the details. Indeed the smaller a structure of interest becomes, the more blurry it appears in the original slice. Especially small blood vessels in the liver or small structures inside the tumor (arrows) are difficult to be accurately delineated due to the low local contrast. It is evident that in the corrected image the vertical resolution is now limited only by the distance between acquired images and not any more by the out-of-plane signals. This example showcases that the Monte Carlo correction method is also beneficial for the full 3D bio-distribution volume renderings, as it retrieves contrast between tissues that was previously masked through scattered sub-surface photons. Indeed the difference is stronger for small structures with fine outlines and becomes

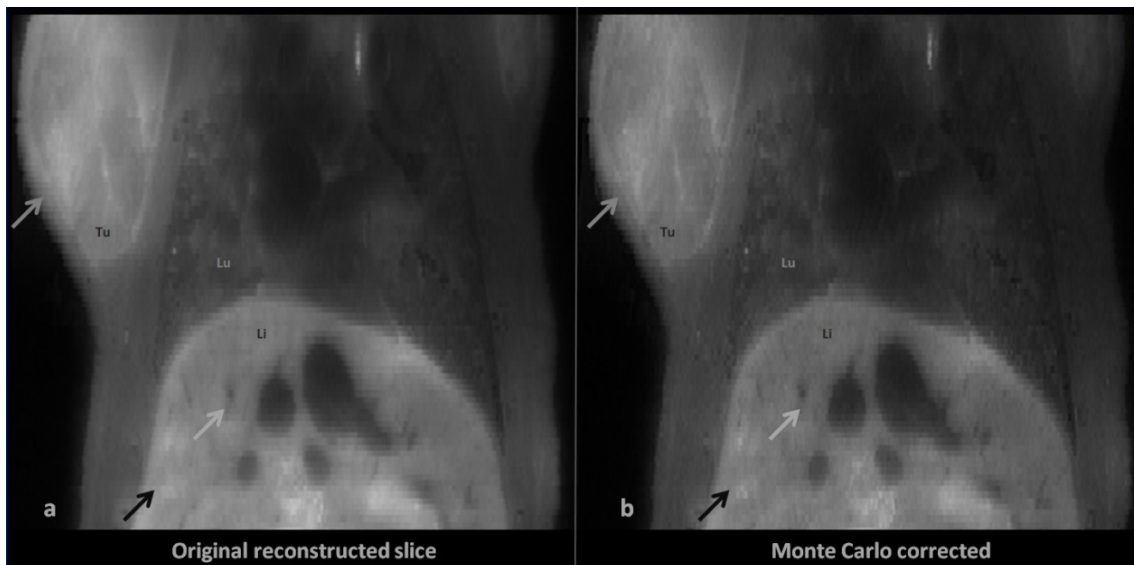


Figure 7-3. The effect of the Monte Carlo method before (a) and after (b) correction in a reconstructed sagittal slice of a tumor bearing xenograft mouse model. The method effectively eliminates ‘blurring’ that is occasionally identified (arrows) in the pre-processed image and successfully restores the z-axis resolution of the method.

prominent for smaller distances (thinner sectioning) between successive fluorescence block face images.

7.2: Application examples of the FASED fluorescence correction algorithm in *ex-vivo* images

In this Chapter we initially showcase that the modification of epi-illumination fluorescence images caused by different concentrations of tissue absorbers and scatterers may be prominent and lead to quantification errors and ultimately to false positives and false negatives. Next, we successfully demonstrate examples of the developed FASED algorithm with phantom data and animal measurements that reveal its ability to truly retrieve the underlying fluorescence bio-distribution devoid of tissue optical properties effects. Further cases that support its performance are demonstrated on *in-vivo* animal images and clinical data in Chapter 7.

Phantoms

To study the effect of background tissue optical properties on the measured fluorescence intensity image, phantoms were created to simulate the different concentrations of absorbers and scatterers typically found in tissue, organs or structures. The main constituents of the constructed liquid phantoms were mouse blood (to simulate the light absorption effect of haemoglobin), Intralipid (acting as a light scatterer) and a fluorophore. The fluorophore's concentration was kept constant throughout the different experiments for reference purposes while the concentrations of blood and Intralipid were varied to cover a wide range of tissue appearance. During all the experiments we used heparin as an anti-clotting agent for the mouse blood. Two fluorophores were studied at constant concentrations for different background optical properties. For the near-infrared area of the spectrum AngioSense 750 (Perkin Elmer, Waltham, MA) was the chosen fluorophore, while fluorescein isothiocyanate (FITC) (reference) was used to examine the effects of tissue absorption and scattering in the visible spectrum. A black plastic container was used to confine the liquid phantom (with total volume of 3ml). The container's depth was selected at around 1cm in order to minimally interfere and not cause any artifacts on the excitation and/or fluorescence photons distributions. Furthermore, all liquid phantoms were prepared and imaged inside the same container so as to minimize random errors.

For the imaging procedure the in-house developed custom clinical-grade imaging setup (described in Chapter 3) was used. Thus for the near-infrared fluorophore, color and EFI images were obtained from all the phantoms after identical illumination with a 750-nm diode laser (BWF2, B&W TEK, Newark, DE) and detection with a sensitive CCD camera (DU-888, Andor Technology, Belfast, UK), while for the visible a filtered white light source was used for FITC excitation.

In the beginning, to decouple and study the effects of tissue absorption and scattering on the captured fluorescence intensity image individually, we arranged two series of phantom experiments. In the first, scattering, induced by using Intralipid, was kept

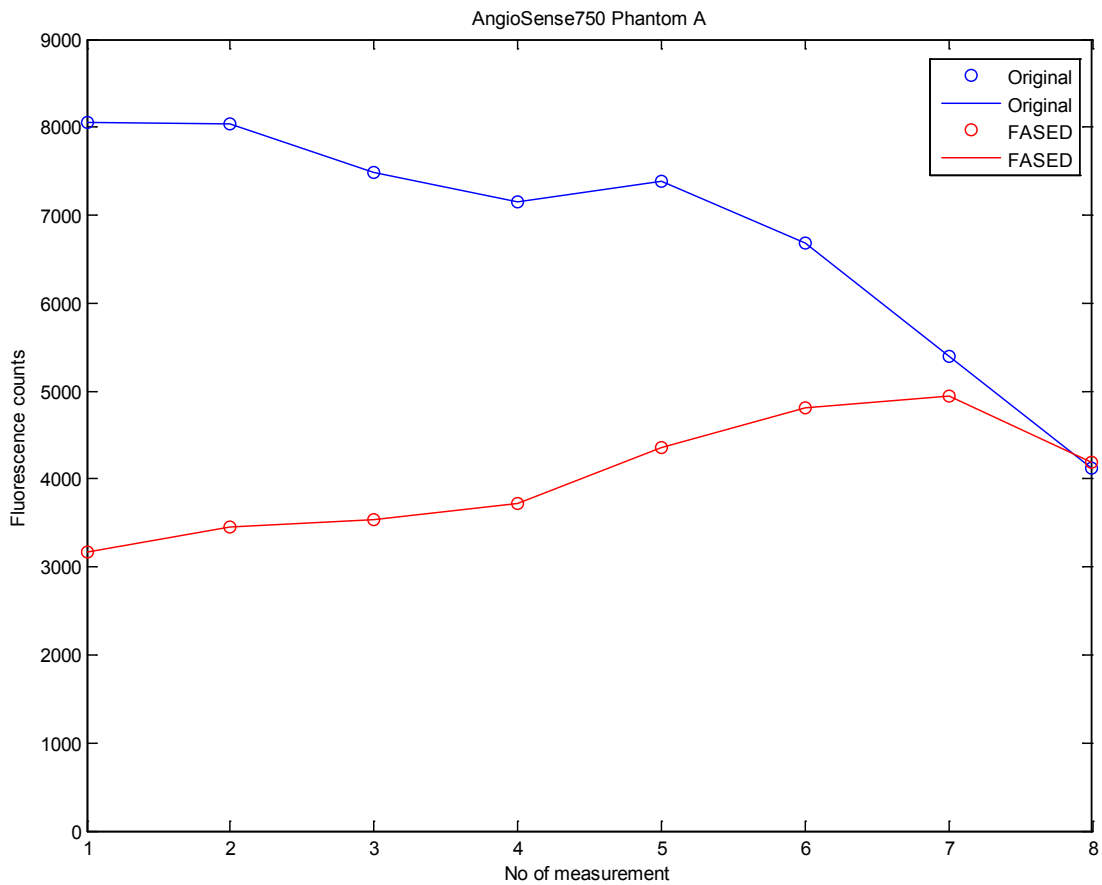


Figure 7-4. Series of phantoms, where the blood concentration (absorber) increases along the x-axis. The mean fluorescence intensity at the center of the phantom is calculated for every absorption/scattering combination before (blue line) and after the FASSED correction (red line). Evidently, the fluctuation of the fluorescence intensity attributed to altering tissue parameters is reduced after the application of the algorithm. AngoSense750 was the fluorophore of choice for the near-infrared.

at a constant concentration, while the blood concentration was changing; in the second series vice versa. These sets of phantom measurements are referred in the images as Phantom A and B respectively. Using these simple deterministic phantoms Fig. 6-4 and 6-5 demonstrate the EFI limitations as a function of the concentration of one tissue optical property, either absorption (Fig. 6-4) or scattering (Fig. 6-5). They display graphs with mean values of the captured fluorescence counts that are averaged over the phantom area for different absorption-scattering combinations. For Fig. 6-4 the scatterer concentration is constant at 1% Intralipid, while the blood concentration increases exponentially from 0%

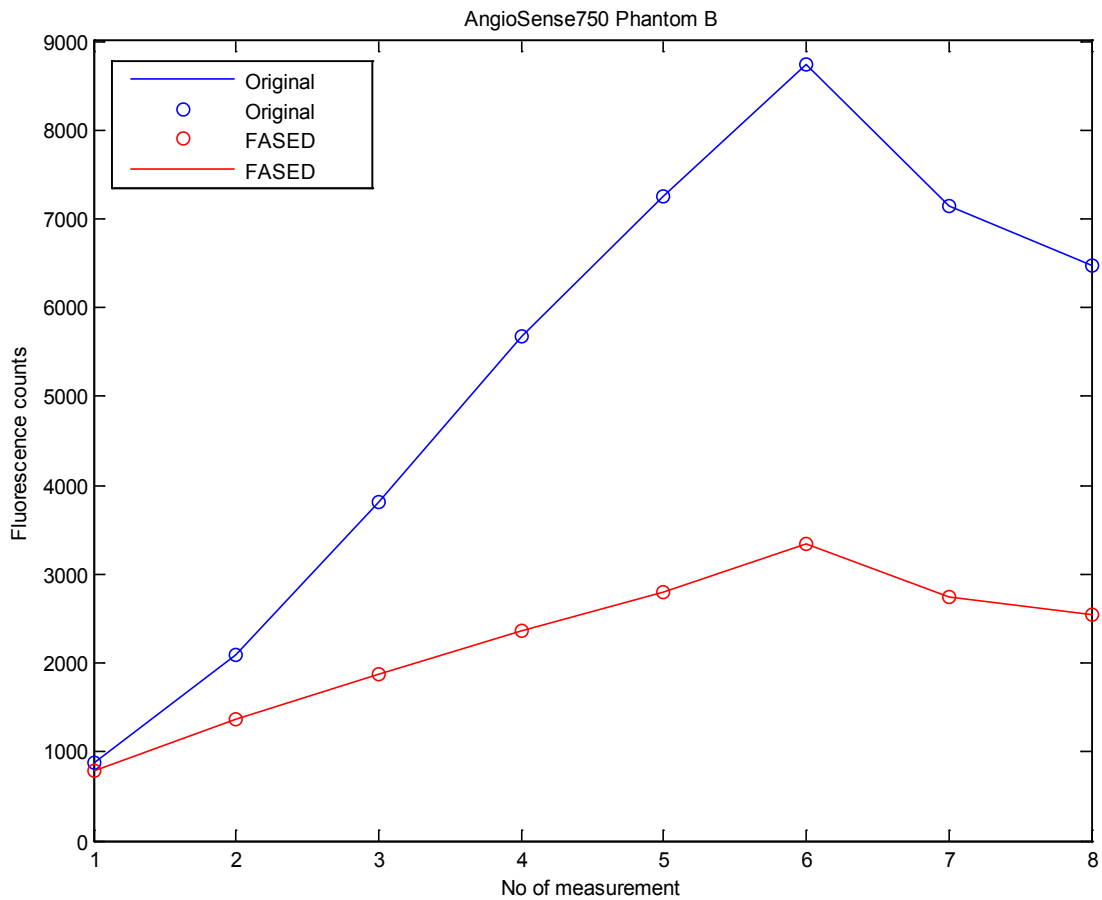


Figure 7-5. Series of phantoms, where the IntraLipid concentration (scatterer) increases along the x-axis. The mean fluorescence intensity at the center of the phantom is calculated for every absorption/scattering combination before (blue line) and after the FASED correction (red line). Evidently, the fluctuation of the fluorescence intensity attributed to altering tissue parameters is reduced after the application of the algorithm.

to 10% of the whole phantom volume (0%, 0.1%, 0.25%, 0.5%, 1%, 2%, 5%, and 10%). In contrast, in Fig. 6-5 the absorber (blood) concentration is 0.25% for all phantoms and the scatterer ranges from 0% to 10%.

It is notable how strong fluorescence intensities vary with background optical properties, especially when scattering is varied. Indeed the intensity of the captured fluorescence signal varies more than 700% between the lowest and highest values. Absorption by contrast has a distinct but weaker effect on EFI images in the near-infrared; the values drop down to 50% with increasing blood concentration. However this should be

still considered as a source of ambiguity in general and false negatives in particular since clinical examples have demonstrated cases (presented in Chapter 8) with significant variations of blood concentrations between cancerous lesions and surrounding tissues. By comparison to EFI, FASED values show markedly lower fluctuations in both phantom cases. Their values remain more stable and less affected by changing background optical properties. Therefore they represent a more consistent measure of true fluorophore concentration than traditional EFI.

Interestingly, the same set of phantom experiments gave a considerably different result when another fluorophore was used, namely FITC. It is well known that the molar extinction coefficient of haemoglobin is significantly (more than one order of magnitude) higher in the visible and that it therefore absorbs noticeably more photons than in the near-infrared, strongly affecting thus the recorded EFI image. Additionally since the effect of tissue scattering changes slightly from 400-800nm, it continues to be a considerable source of ambiguity also in this wavelength range. Indeed, our experiments demonstrated that haemoglobin has probably the most severe effect on EFI images in the visible range, while changing scattering concentrations also create big variations in fluorescence intensities.

Our experiments are summarized in Fig. 6-6 and 6-7. As in the case of AngioSense750, EFI images in Fig. 6-7 show a distinct peak of fluorescence amplitude with increasing scattering concentration. This distinctive effect is attributed to the fact that tissue scattering probably reaches a plateau after which it no longer “enhances” fluorescence photons by back-scattering them towards the surface of the sample; it rather “rejects” excitation light photons from reaching “deep” inside the sample, reducing thus the overall excited sample volume and accordingly the total captured fluorescence intensity. In contrast to the near-infrared fluorophore case, increasing haemoglobin concentrations now lead to a particularly steep, monotonous decay of fluorescence intensity. Indeed, the recorded signal amplitude of the phantom with 10% blood concentration is now only 8% of the initial 0%-blood phantom. Once again the FASED

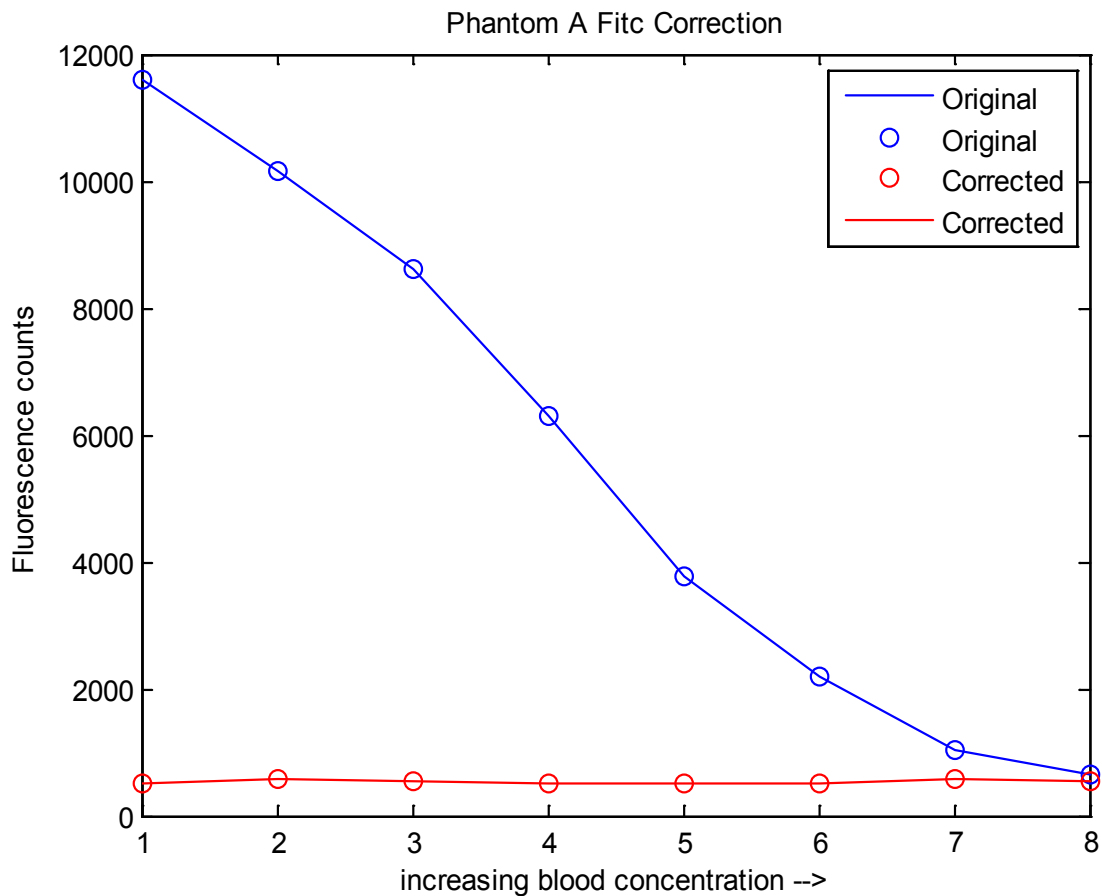


Figure 7-6. The same series of phantoms as in Fig. 6-4, where the blood concentration (absorber) increases along the x-axis. The mean fluorescence intensity at the center of the phantom is calculated for every absorption/scattering combination before (blue line) and after the FASED correction (red line). Evidently, the fluctuation of the fluorescence intensity attributed to altering tissue parameters is reduced after the application of the algorithm. FITC was the fluorophore of choice for the visible.

images show very stable values throughout the whole range of background optical properties, especially in the variable blood concentrations' phantom and only slightly vary for higher scatterer concentrations.

The final phantom experiments intended to demonstrate the case of arbitrarily varying tissue absorption and scattering in order to study their combined effect on the acquired images. This would be the most stringent test for the FASED algorithm and would represent more realistically the actual clinical situation. The top row in Fig. 6-8 shows color

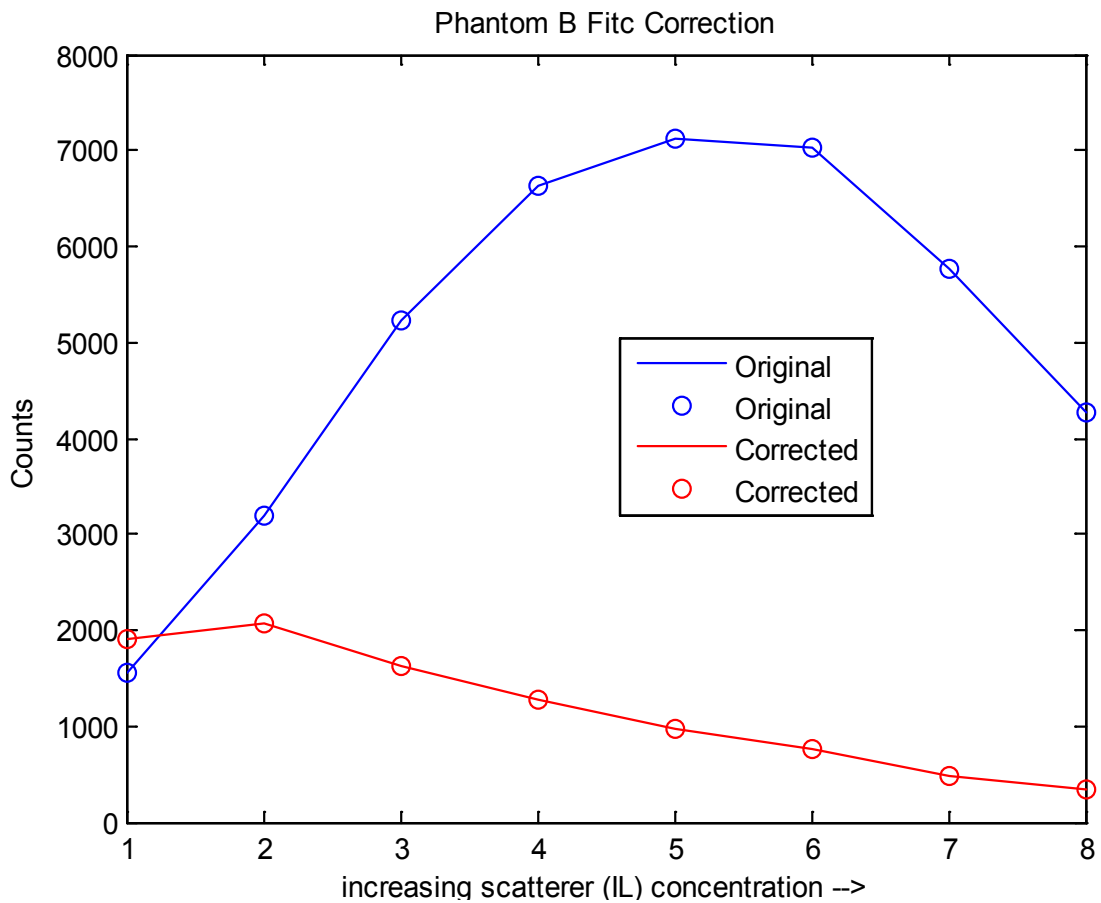


Figure 7-7. The same series of phantoms as in Fig. 6-5, where the Intralipid concentration (scatterer) increases along the x-axis. The mean fluorescence intensity at the center of the phantom is calculated for every absorption/scattering combination before (blue line) and after the FASED correction (red line). Evidently, the fluctuation of the fluorescence intensity attributed to altering tissue parameters is reduced after the application of the algorithm. FITC was the fluorophore of choice for the visible.

photographs of 7 diffusive media consisting of the same concentration of the AngioSense750 fluorochrome (1nmol), but randomly varying amounts of blood and scattering. The bottom row shows the corresponding EFI images obtained from the phantoms. The images clearly illustrate once again the fundamental EFI shortcoming: even if the fluorophore concentration does not vary in the phantoms, the recorded intensities change significantly as a result of a change in the background optical properties. The measurements in Fig.6-8 also demonstrate that the relation of fluorescence intensity to the background optical properties is a complex one.

For example even if the intensity on Fig.6-8D, Fig. 6-8E and Fig.6-8G is similar, the composition of background optical properties is markedly different as shown under each column and moreover in Table 6-1. Conversely, a doubling in the scattering of the medium does not have the same effect as a doubling in absorption, as evidenced by observing phantoms B and C and D and E respectively. Importantly however, Fig.6-8 illustrates a large variation of recorded fluorescence intensities, in phantoms that all have exactly the same fluorescent concentration. In this case, if phantom A was perceived as being of high fluorochrome concentration (positive) then all remaining phantoms could be falsely interpreted as negatives, leading to 7 false negative readings and vice versa, assuming that each of the phantoms represents a different lesion in the field of view.

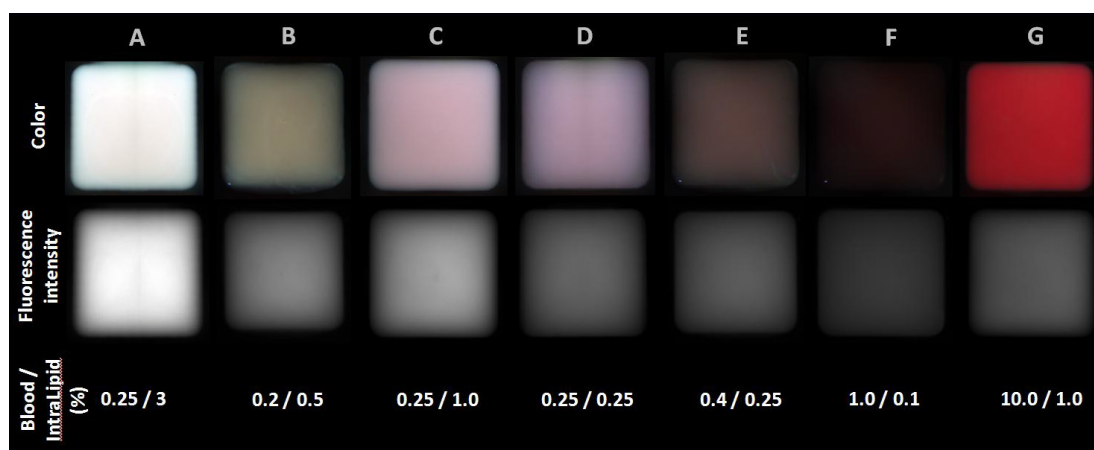


Figure 7-8: Color (upper row) and fluorescence (lowermiddle row) images of tissue-mimicking phantoms together with the equivalent absorber and scatterer concentration (bottom row). All phantoms contain the same concentration in fluorescent agent (AngioSense750) but different concentrations of blood and intralipid, as described in Table 1. Fluorescence signals show a significant variation between the samples with maximum deviation of 73% (between sample (A) and (F)). This variation in measured signals is due to the differences in the optical properties. Interestingly, even samples which in color image seem to have similar color appearance, i.e. (C) and (D) they have a significant relative difference in fluorescence signal, i.e. 0.74 and 0.44 respectively. From this example it is clear that the variation in tissue optical properties can easily introduce significant measurement errors which consequently might lead to false positive or negative diagnostic assessment.

The FASED method, when applied to the phantom measurements of Fig. 6-8 significantly minimized the variation of fluorescence intensities in the corrected images, as summarized in the right-most column of Table 6-1. Thus it was further demonstrated that,

as analysis from the previous phantom studies outlined, the FASED method minimized the variation of fluorescence intensities for changing tissue absorption and scattering and that it provided a more trusted measure of true fluorophore concentration in tissue.

Phantom	Blood (%)	Intralipid (%)	Fluorophore (%)	Fluorescence intensity (n.u.)	FASED Intensity (n.u.)
A	0.25	3.00	1.67	1.00	0.92
B	0.20	0.50	1.67	0.59	0.80
C	0.25	1.00	1.67	0.74	0.84
D	0.25	0.25	1.67	0.44	0.52
E	0.40	0.25	1.67	0.41	0.72
F	1.00	0.10	1.67	0.27	0.59
G	10	1.0	1.67	0.53	1.00

Table 7-1: Compositional properties of the samples shown in Fig. 6-8 and average fluorescence intensity of each sample before and after the FASED correction.

Animal imaging

In summary phantom studies showed that discrepancies between measured and real fluorescence intensity can be easily found in epi-illumination fluorescence imaging and that therefore correction approaches should be implemented. They also demonstrated that *in-vivo* performance could be similarly affected provided that optical property variations of the magnitude seen on Fig.6-4 until 6-8 were present in the tissues imaged. Diseased tissue, for example inflamed or cancerous tissue, has several compositional changes compared to healthy tissues, resulting in changes in color as well. Angiogenesis and inflammation for example are processes known to change the tissue color due to the increased blood concentration. Tissue hypoxia also could further change the color appearance of a tissue

since deoxygenated hemoglobin has a markedly different absorption spectrum compared to oxygenated hemoglobin. In addition, cancerous tissue is also known to modify its scattering due to the abnormal and higher density of cells.

To study if tissue discolorations could affect fluorescent intensity images we analyzed cryoslicing fluorescence measurements from xenograft animal models. Animal studies were carried out in compliance with the Guide for the Care and Use of Laboratory Animal Resources (1996), and were approved by the local Animal Care and Use Committee. We used immunodeficient female NU/NU nude mice (Charles River Research Laboratories, Margate, UK) and two different cell lines (4T1 cells that develop mammary carcinoma and CT26 cells that induce colorectal carcinoma) with similar kinetics. Due to their different proliferation characteristics, these cell lines are known to develop tumors with different vascular network and color appearance. Xenografts with 4T1 cells serve as models for stage IV breast cancer and grow rapidly to develop solid and dense tumors with white-ish appearance, while CT26 cells develop highly vascularized tumors that yield a reddish color appearance. Having animals with one highly absorbing and one highly scattering tumor allowed to test our hypothesis and demonstrate that fluorescence intensity images in animal models are indeed highly dependent from the underlying tissue properties and therefore can potentially lead to false positives and false negatives.

The mice were implanted with 0.4 million 4T1 cells and 1.0 million CT26 cells at opposite sites at the mammary fat pad. Under daily monitoring they were allowed to grow for 8-10 days until they reached a size of around 8mm in diameter. At this point the animals were intravenously injected (via the tail vein) with a specific (“activatable”) fluorescent probe (ProSense, Perkin Elmer, Waltham, MA) that targets a choice of different cathepsins. 24h later the mice were anaesthetized and *in-vivo* imaged both intact and with their tumors surgically exposed with our custom epi-fluorescence imaging system simulating the surgical procedure followed in the operating room (results presented in Chapter 8). Afterwards the animals were euthanized, frozen and imaged again with the in-house developed multispectral cryoslicing imager described previously in Chapter 2. During this procedure

and after every block face imaging course of action, 18 μ m-thin sections were collected on microscope slides. At a later stage they were in turn imaged for fluorescence once again. These fluorescence images of the slices were captured in order to create a 'gold standard' dataset, with which every cryoslicing image could be directly compared. As a result, each mouse cross-section was imaged by EFI before and after slicing so that the same cross-section was acquired while being part of the mouse body and after slicing placed on a microscope slide. This process has the benefit that it can accurately examine the influence of optical properties on EFI. This is because images obtained before slicing are influenced by the underlying properties of the mouse tissue. Conversely, the 18 micron thickness slices serve in this case as the gold standard, since thin sectioning removes the effects of tissue absorption and scattering from the image, thus allowing for a direct visualization of true fluorescence distribution. The use of thin slices to avoid tissue absorption and scattering is a common practice in histology for example, which customarily uses 5-20 micron thin tissue sections for imaging.

Fig.6-9a-d show color, fluorescence and FASED cross-sectional images from the upper thorax of an entire mouse, whereby Fig. e-l depict magnified pictures obtained from the left (4T1) and right (CT26) tumor, from the area indicated on Fig.6-9a with a red and green rectangular outline. Also the fluorescence image of the equivalent 18 μ m slice is shown for comparison. A first observation between EFI and FASED cross-sectional images of the mouse body is again the resolution improvement as evident in Fig.6-9b vs. Fig.6-9d respectively. However of interest in the analysis herein is the different appearance of fluorescence between the two images. Fig.6-9b (EFI) shows a rather homogenous fluorophore distribution inside both tumors. Their fluorescence intensities are comparable to each other and seem considerably higher than the surrounding tissue. Furthermore a highly vascularized tumor area displayed in Fig. 6-9i (red arrow) shows an apparently lower fluorescence accumulation (Fig. 6-9j). In contrast Fig.6-9c, which serves as the gold standard, shows a significantly different appearance with fluorescence having a markedly different pattern and amplitude. In this case, the true fluorescence signals are originating

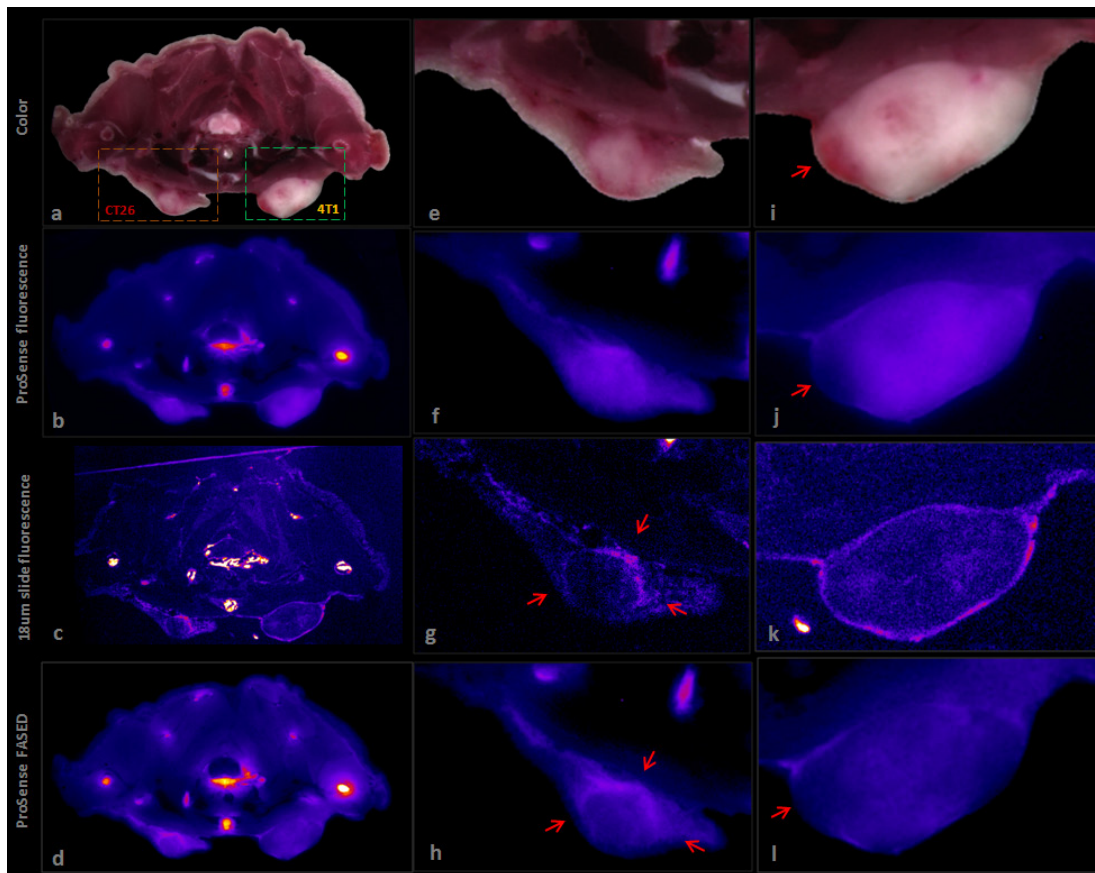


Figure 7-9: Color (a, e), fluorescence intensity (b, f) and FASED images (d, h) at a cross-section of a mouse bearing different xenograft tumors (4T1 and CT26). 18um-thin slices (c, g) were collected during the sectioning procedure and are used as the gold standard for validation. FASED images correct for tumor heterogeneity in optical properties and reveal the true fluorescence distribution inside the animal. FASED images tumor-to-background ratio (3b-3d) and fluorophore accumulation patterns (3f-3h) show superior correlation to the 18um slices when compared with conventional fluorescence photography (b, f).

from the periphery of the tumors rather than inside of them and, moreover, their overall contrast with the surrounding muscle tissue is fairly low.

Correspondingly the FASED images shown on Fig.6-9 demonstrate a far more accurate correlation with the gold-standard (Fig. 6-9c) as regards to the molecular contrast between the tumors and the surrounding structures (tumor-to-background ratio). Furthermore, closer examination (Fig. 6-9g-h) reveals that the corrected FASED image (h) shows precise delineation of the agent's real delivery at the periphery of the tumor. Due to

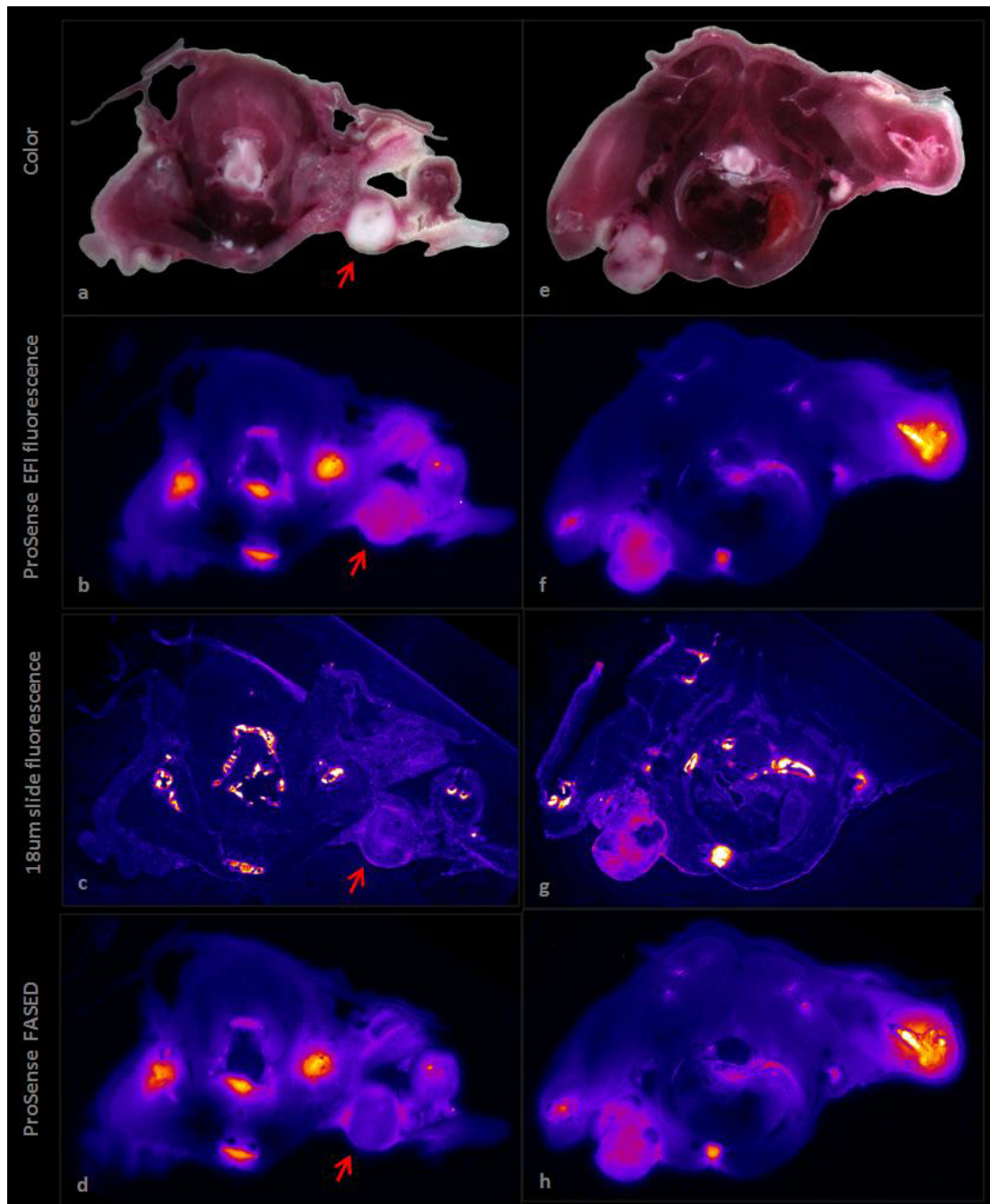


Figure 7-10: Color (a, e), fluorescence intensity (b, f) and FASED images (d, h) at two cross-sectional cryoslicing images. 18um-thin slices (c, g) were collected during the sectioning procedure and are used as the gold standard for validation. Striking false positive fluorescent signal in the left mouse tumor (red arrows) underlines EFI limitations and inconsistency and supports FASED ability to reflect fluorescence concentration information.

tumor heterogeneity and varying optical properties the corresponding fluorescence image (f) fails to identify the real fluorophore distribution and leads to the false assumption that it is uniformly distributed inside the tumor. Altogether FASED corrected images seem to retrieve an extensive part of the real fluorophore distribution. Both tumors look now inhomogenous with their patterns closely matching those on the 18 μ m slices, as indicated at the concentrated fluorescence distribution at the right tumor rim (Fig. 6-9g and 6-9h, red arrows). In addition, the overall tumors' signal levels are markedly lower than on the original EFI images. With these animal experiments, it becomes particularly clear that EFI imaging can have obvious limitations also for animal imaging and can fail to clearly identify the sites of fluorophore accumulation and their correct levels due to the underlying tissue optical properties. At the same time a highly vascularized area of dark red appearance reveals how highly absorbing regions can lead to significant quantification errors and false assumptions based on EFI images.

Further discrepancies between EFI and "gold standard" images are shown at Fig. 6-10. Cross-sectional images at two different regions of the same mouse thorax depict color, EFI, 18 μ m sections and FASED images at each plane. In this case, of interest is the quantification comparison of EFI and FASED. In particular, the evident false positive fluorescence signal of conventional epi-illumination imaging at the highly scattering 4T1 tumor (left side of the mammary fat pad) is in this case rather striking. Interestingly, EFI images show relatively strong fluorescence signals inside both tumors (Fig. 6-10b and f). In the thin sections' images, though, the fluorescence signal in the 4T1 tumor is almost totally absent (Fig. 6-10c red arrow) while the CT26 tumor shows a considerable accumulation compared to background muscle tissue (Fig. 6-10g). FASED processed images display a very similar bio-distribution for the CT26 tumor (Fig. 6-10h) compared with the EFI and 18 μ m-thin images. However on the other side of the mammary fat pad the discrepancy between EFI and the FASED images is considerable. The fluorescence activity inside the 4T1 tumor is massively reduced in the FASED image (Fig. 6-10d) showing a close match with the gold

standard images and thus a more trusted measure of the real fluorescence inside the tumors.

Altogether *ex-vivo* imaging results demonstrated that shortcomings of conventional epi-illumination fluorescence imaging can indeed be observed and can have a significant effect on the captured image. Phantoms images and more importantly animal images presented further support for the argument that EFI imaging can greatly vary in cases of inhomogeneous tissue characteristics since EFI-captured fluorescence bio-distributions are a complex combination of true fluorophore concentration and local tissue properties. Thus, inaccurate fluorescence measurements can potentially result in poor performance evaluation and misjudgment of an agent's true targeting efficiency due to inhomogeneities between tissues of different optical properties. Accurate quantification, which is of utmost importance especially in the case of clinical imaging, is therefore limited.

Chapter 8: Application in *in-vivo* fluorescence images

In this Chapter we demonstrate the performance of the FASED algorithm for tissue optical properties correction in *in-vivo* animal images and human clinical data. We present two animal studies with subcutaneous tumours to corroborate the limitations of conventional epi-illumination imaging (EFI) and support the argument that our suggested correction method, FASED, succeeds in providing more trusted fluorescence images. Additionally, based on clinical data obtained from intra-operative imaging of ovarian cancer patients administered with a FITC-labeled folate targeting probe, we showcase that the modification of fluorescence images by tissue optical properties may be prominent and lead to false negatives and discuss/emphasize on the potential implications of the EFI technology in human clinical applications.

Animal imaging

The camera system employed in both studies has been previously described in Chapter 3. In brief, the camera system consists of a charge-coupled digital (EM-CCD) camera for sensitive fluorescence detection and two separate cameras for the detection of

intrinsic and color images. The system attains a variable field of view (FOV) of 15cm x 15cm to 3cm x 3cm, with a corresponding resolution varying from 150–30 microns. Data are acquired in parallel by all cameras so that color and fluorescence images are simultaneously collected. For the clinical measurements attention has been given to the selection of a filter set that allows multi-spectral collection of color and fluorescence images in the visible light spectrum, as appropriate for creating FASED images of FITC fluorescence.

We present herein the two animal *in-vivo* studies in the order on which they were performed. Thus we firstly exhibit preliminary results of the FASED method for neck tumor bearing mice and afterwards demonstrate the *in-vivo* results of the dual-tumor animal imaging study partly described also in Chapter 6.2. BALB/c mice were implanted with 1 million CT26 mouse colon adenocarcinoma cells subcutaneously in the neck area. Tumor growth was daily monitored for around 10 days until they reached a size of approximately 5-8mm. At this time the animals were intravenously injected (via the tail vein) with a tumor specific (heat shock protein targeting) CmHsp70.1 monoclonal antibody (Stangl, Gehrmann et al. 2011), which was allowed to circulate for 12h. The mice were then anaesthetized and *in-vivo* imaged with our custom multispectral clinical imaging system, after their tumors were surgically exposed.

Figures 7-1 and 7-2 show color, conventional EFI fluorescence and FASED images of two different mice, one with a relatively large and one with a relatively small tumor. In Fig. 7-1 a strong fluorescence EFI signal can be observed not only inside the tumor, but also on the mouse skin flap (red arrow). However, previous experience with this specific mouse model and publications (Stangl, Gehrmann et al. 2011; Stangl, Gehrmann et al. 2011) oppose that this antibody is selectively accumulated inside the tumor and not in its surroundings. Furthermore, visual inspection of the color image suggests distinct variations in the optical properties among different tissues. Indeed, the mouse skin as a highly scattering tissue type has a typical white color appearance, while both the tumor and the muscle underneath look highly vascularized and absorbing and have a dark red appearance.

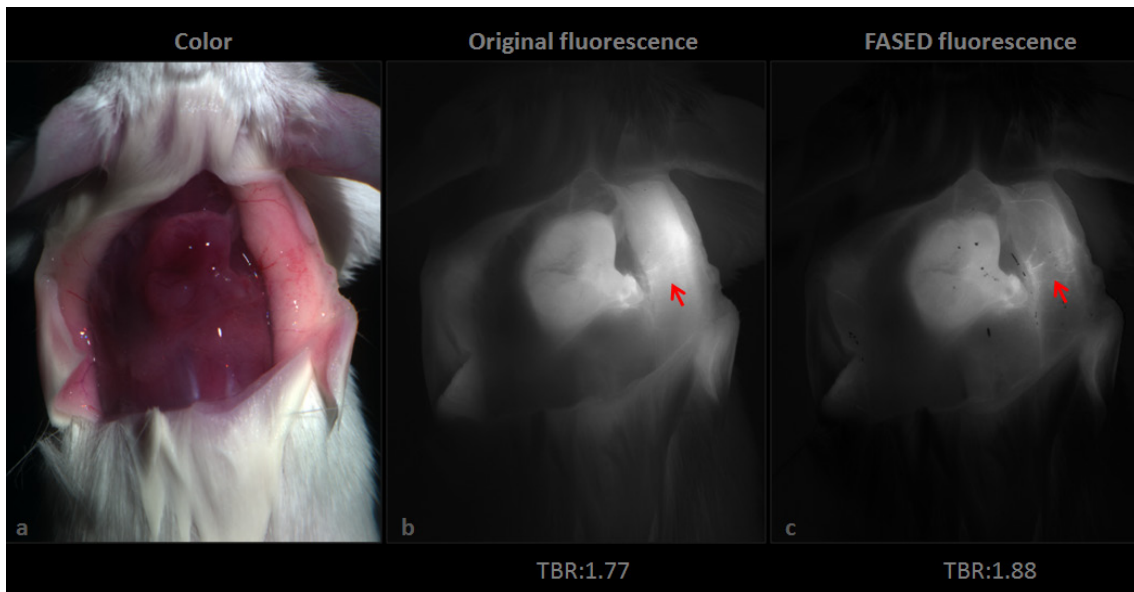


Figure 8-1: In-vivo color (a), fluorescence intensity (b, d) and FASED images (c, e) of a colon cancer bearing xenograft mouse on the neck area. A strong fluorescence signal is captured by the EFI image (b) in a skin flap on the right mouse side. The effect of optical properties is decomposed and corrected in the FASED image that reveals the true fluorescence signal.

Based on previous phantoms and animal imaging data one can argue that these variations in tissue optical properties are significant and can influence EFI imaging. By comparison, FASED images show a practically identical distribution of fluorescence inside the tumor while the signal emanating from the before mentioned skin flap is significantly lower. Moreover, small blood vessels that were previously masked by the skin signal in EFI are now a lot clearer and more discernible from the neighboring structures.

Although in Fig. 7-2, the fluorescence intensity coming from the mouse skin is not as high, as the skin flap now does not have such a dramatically different color appearance from the underlying muscle as before, other distinctive differences between EFI and FASED are noticeable. Firstly, the FASED image displays a much clearer tumor outline when compared to the EFI fluorescence. For example the tumor border marked with a blue arrow has a considerably greater contrast in FASED than in the conventional fluorescence image. Additionally the white-ish non-cancerous structure situated on top of the tumor is a lot easier to distinguish in the FASED image. Accurate tumor and tumor border identification is

of utmost importance in clinical intra-operative imaging and our results suggest that FASED images could be of particular interest for intra-operative guidance and feedback during the surgical tumor resection procedure. Indeed comparisons of the intensities between the tumor and neighboring tissue (tumor-to-background ratio, TBR) show that in both cases of Fig. 7-1 and 7-2 the TBR in the FASED image is higher than in the pre-processed EFI. Especially in Fig. 7-2, the difference between TBRs can reach up to 25%.

Another noteworthy finding is noted with green circles in Fig. 7-2. Interestingly, two areas of the neck musculature with different optical properties and distinct borders can be clearly identified in the color image; namely one is slightly more absorbing than the other. The equivalent EFI image seems to follow this variation in optical properties and therefore displays one of them as slightly brighter than the other. However visual investigation of all captured images including Fig. 7-1 suggests that the tumor surroundings on the neck region have a generally homogenous fluorescence distribution with only small blood vessels being occasionally brighter. The difference is not great but substantial to suggest that accurate quantification in epi-fluorescence imaging (EFI) can be hampered due to inhomogeneities in optical properties and that correction methods should be applied.

Although these preliminary results clearly demonstrated the limitations of EFI *in vivo* as well as the performance of the FASED algorithm, their disadvantage was that, unfortunately, no trusted, 'gold standard' data were available in order to compare and confirm our hypotheses other than previous experience on the animal model and a series of logical assumptions. Therefore we designed a more thorough and detailed study to monitor the effect of tissue optical properties on fluorescence images using nude mice implanted with two different cell lines, where 18 μ m mouse sections acquired *post mortem* would be used for the confirmation of the results. Cryoslicing images further helped us establish a direct comparison between planar EFI and FASED images (the details of this study have been presented in Chapter 6.2).

The top row of Fig.7-3 demonstrates measurements obtained from anaesthetized

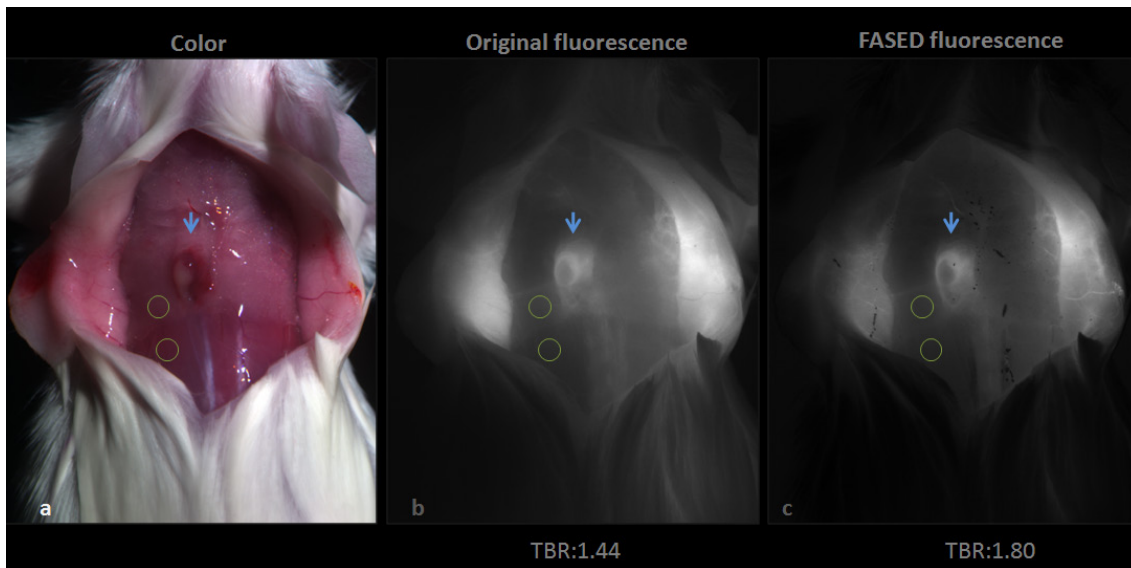


Figure 8-2: In-vivo color (a), fluorescence intensity (b, d) and FASED images (c, e) of a colon cancer bearing xenograft mouse on the neck area. FASED more clearly identifies the tumor border (TBR) (blue arrow) and corrects the fluorescence signal for the intensity fluctuations due to the underlying tissue properties (green circles).

intact mice *in-vivo* 24h after the administration of a tumor specific protease-activated molecular probe (ProSense). Additionally Fig. 7-3d and 7-3e show *in-vivo* pictures of the same animal after surgical exposure of the upper thorax. In this way we visualized both 4T1 (mammary carcinoma) and CT26 (colorectal carcinoma) subcutaneous tumors during different instances of the intra-operative surgical procedure. Interestingly, the FASED image of the intact mouse in Fig. 7-3 shows a more accurate tumor delineation compared with the EFI image as observed previously in the case of the neck tumor animals. Especially the CT26 tumor provided a significantly clearer contrast compared to its direct surroundings. Additionally, Fig. 7-3 shows a considerable difference between FASED and EFI images with regards to the quantification of fluorescence intensity in the 4T1 tumor on the left mouse side. Both the intact mouse (Fig. 7-3c) and the exposed tumor (Fig. 7-3e) FASED images demonstrate markedly lower tumor intensity when compared to Fig. 7-3b and 7-3d, while the intensities in the CT26 tumor are comparable. Regions of interest (ROI) defined on and around the 4T1 tumor, at an area next to it (areas A/B at Fig. 7-3d and C/D at Fig. 7-3e),

showed an almost 35% difference in tumor-to-background ratio (TBR) between the EFI (TBR: 2.26) and FASED (1.68) image. This finding indicating that FASED can lead to more

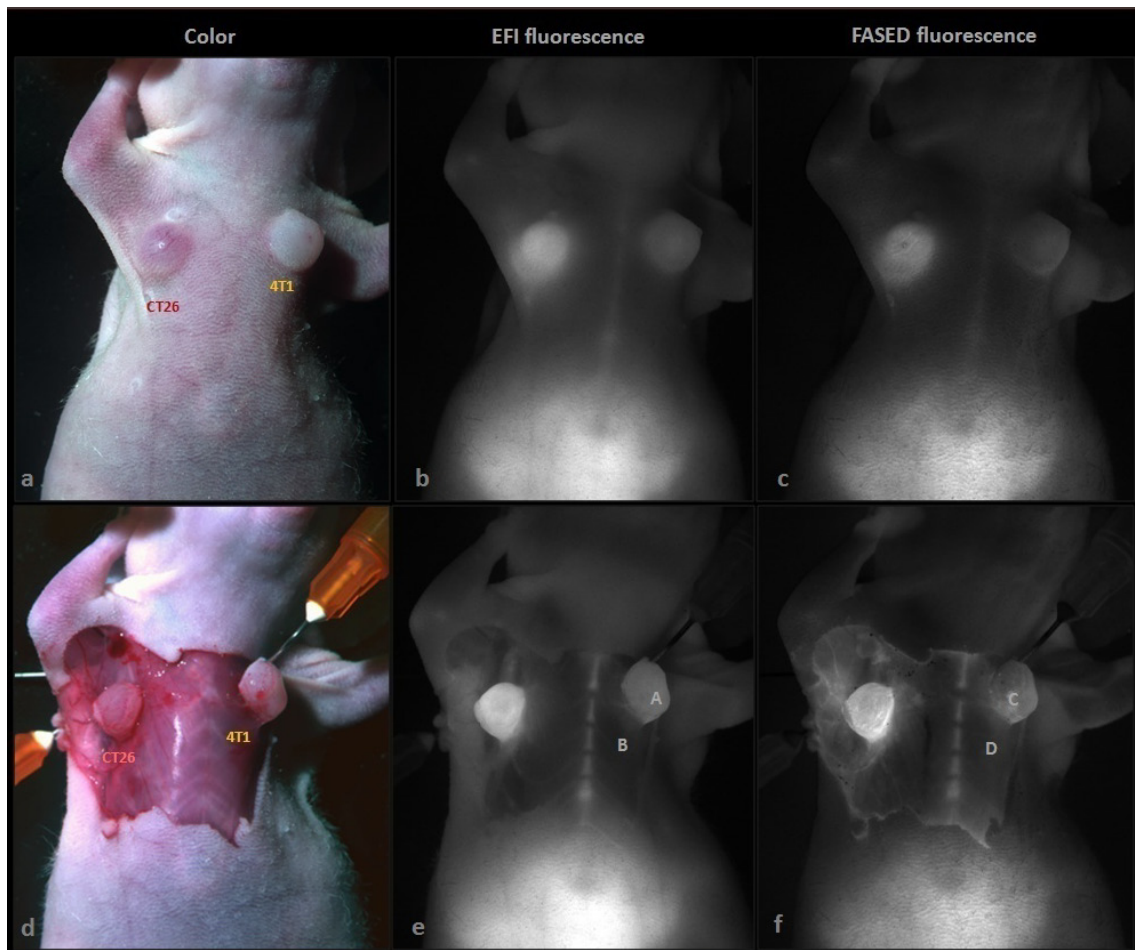


Figure 8-3: In-vivo color (a), fluorescence intensity (b, d) and FASED images (c, e) of a mouse implanted with two different xenograft tumors on the mammary fat pad. FASED displays a 30% less contrast for the 4T1 tumor and therefore reflects better the 'gold standard' results.

trusted fluorophore distributions is further supported with various samples/cases from the 'gold standard' dataset (with Fig. 6-10 being indicative), since the fluorescence images of the 18 μ m-thin sections repeatedly showed a high agent concentration for the CT26 tumor while the 4T1 tumor had a mostly background comparable intensity.

In-vivo animal imaging demonstrated that inhomogeneities in tissue optical properties are evident in planar fluorescence imaging of tumor bearing mice and can influence the performance of EFI technology. To correct for the effects of optical properties on EFI and develop a method that yields accurate imaging we have developed FASED, a multi-spectral imaging method appropriate for real-time video rate) imaging. Our method retrieves sharpness in fluorescence images, provides better contrast between cancerous lesions and their surroundings and successfully recovers trusted fluorescence bio-distribution measures.

Clinical imaging

Fluorescence is an ideal modality for enhancing surgical imaging in particular as it directly relates to clinical optical imaging procedures and the physician's vision. Multispectral methods have been considered many times in order to increase contrast in fluorescence images by differentiating fluorophores of interest from tissue auto-fluorescence, for instance in microscopy and preclinical studies (Zimmermann, Rietdorf et al. 2003; Levenson and Mansfield 2006) to name a few examples. In contrast, the FASED correction method follows a different approach as it utilizes reflectance measurements at different spectral bands to more fundamentally bring accuracy in EFI images and to reduce the false negative and false positive rate, by minimizing the tissue optical properties effects on the EFI. The implementation of the method requires a system that obtains independent spectral measurements of background tissue and utilizes an analysis in components, as described in Chapter 5, in order to effectively characterize the tissue absorption and scattering contribution and subsequently correct the raw EFI, on a pixel per pixel basis based on experimental measurements. The result is a FASED fluorescence image that is per pixel normalized to reflect true fluorescence bio-distribution independent of the absorption and scattering variation particulars of the tissue imaged. By using fast graphics card processors (GPU), FASED images can be obtained from EFI and multiple reflectance images

also in the operating theater, since the operations utilized herein can be performed in less than 20ms for every frame, allowing thus for video rate operation without delays despite the computations required in real-time.

The FASED ability to reflect true fluorescent bio-distribution would be important for accurate observations and gaining clinical approval in emerging clinical fluorescence imaging studies. For this reason we examined the performance of the method with data obtained from the clinical study with ovarian cancer patients (van Dam, Themelis et al. 2011) described in Chapter 3.5.2. The study was approved by the Investigational Review Board (IRB) of the University Medical Center Groningen, the Central Committee on Research involving Human Subjects (CCMO NL26980.042.09; www.ccmo.nl), and registered at the European Clinical Trials Database (EudraCT 2009-010559-29; <http://eudract.emea.europa.eu>) prior to inclusion. After documented informed consent, patients were intravenously injected with Folate hapten (vitamin B9), conjugated with fluorescein isothiocyanate (FITC) at a dose of 0.3 mg/kg. The injected folate-FITC was produced according to GMP conditions by Endocyte Inc. (West Lafayette IN, USA), after approval of the IMPD documentation according to FDA/EMEA regulations by the local IRB and Hospital Pharmacy at the University Medical Center Groningen. Folate-FITC has an excitation spectrum with a peak at 495 nm and an emission spectrum with a peak at 520 nm. The agent specifically targets the FR- α receptor, after which it is internalized into the cytoplasm.

This first-in-human study using targeted fluorescent agents, aimed at accurately identifying tumor deposits and post-excision margins during palliative surgery, demonstrated false negatives when observing EFI images. Interestingly, some cancerous lesions were highly vascular and appeared dark red on the color images, as shown on Fig.7-4b, whereas surrounding tissue showed a varying color appearance ranging from white to red (Fig. 7-4a). Correspondingly, the uncorrected fluorescence image (EFI) demonstrates absence of fluorescence from the tumor area compared to the fluorescence signals

obtained from the surrounding healthy tissue. In contrast, FASED images demonstrate increased fluorescence from the tumor, as compared to suppressed background

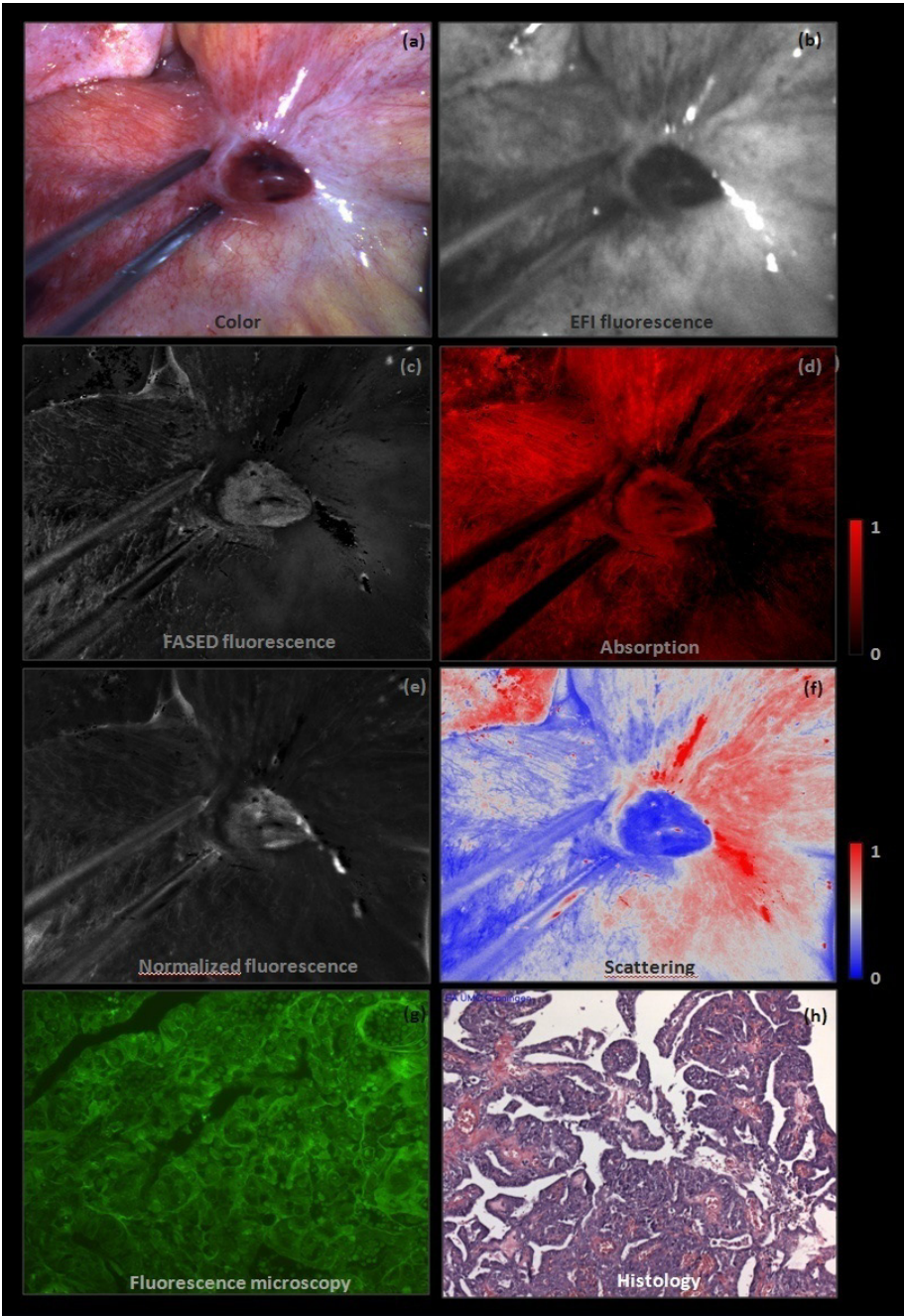


Figure 8-4: Clinical color (a) and fluorescence (b) imaging of a tumor specific folate-FITC molecular probe. A cancerous lesion in a patient suffering ovarian carcinoma appears dark on the color and fluorescence intensity images, due to increased light

absorption of the densely vascularized lesion. Normalized fluorescence (e) and FASED (d) images correct for tissue optical properties and reveal the true fluorescence distribution. Absorption (c) and scattering (f) maps showcase FASED aptitude in distinguishing between fundamental tissue characteristics. Fluorescence microscopy (g) and histology (h) show tumor presence and significant amounts of fluorescence accumulation.

fluorescence. Subsequently the tumor was excised and sent to pathology, which revealed both tumor presence (Fig. 7-4h) and significant amounts of fluorescence in the tumor over surrounding tissues (Fig. 7-4g). Normalized fluorescence (NF) (Ntziachristos, Turner et al. 2005) a method that compensates for absorbers' variations, was also used for comparison, since tissue absorption (haemoglobin) was the main source of intensity variations in these EFI images. Although the NF image also demonstrates fluorescence activity inside the tumor, it does not clearly distinguish its borders in comparison with FASED. Additionally Fig. 7-4d and Fig. 7-4f show how the FASED algorithm analyses the reflectance images into tissue specific constituents, namely haemoglobin (absorption) and scattering in order to decompose the effects of each one on the EFI image and ultimately produce a per pixel corrected FASED image.

Discussion

We demonstrated in this Chapter that EFI images can be significantly influenced by tissue optical properties and they do not accurately resolve tissue fluorescence but instead a mixed contribution of fluorescence, absorption and scattering. We also observed that such effects can be measurable in animal and clinical measurements and can possibly lead to false positives and false negatives. These findings are important when considering them in the context of the emerging translation of novel classes of targeted fluorescent agents for improving surgical and endoscopic imaging, for example agents that target cancer cellular receptors (Vinegoni, Razansky et al. 2009), protease sensitive probes (Kossodo, Pickarski et al. 2010; Mieog, Vahrmeijer et al. 2010), fluorescent nano-particles (Kircher, Mahmood et al. 2003) or viral replications (Adusumilli, Stiles et al. 2006; Chen, Zhang et al. 2009) that can allow tumor margin delineation (Stummer, Novotny et al. 2000; Kircher,

Mahmood et al. 2003). Exemplified by the use of folated-FITC (van Dam, Themelis et al. 2011), the systemic injection of targeted fluorescent agents can shift the paradigm of clinical decision making in cases where the physician's vision is employed as the primary detection method. In this case the availability of accurate fluorescence imaging, operating at video rates is important for clinical propagation and acceptance of the technique.

The ambiguity of interpretation of EFI images is a significant finding as it demonstrates that the variation of optical properties in clinical imaging can have a significant impact on the fluorescence images. While not all of the images obtained required correction, it is unclear which fluorescence imaging is accurate and which is affected by optical properties when observing conventional EFI images. In this manner, Fig. 7-4 demonstrates that at the absence of monitoring and correction for optical property variation, EFI can lead to false negatives. This finding also showcases the heterogeneity between tumors of same classification and reveals that independent spectral measurements are required from each individual examination in order to offer accurate results. The statistically small human sample does not allow for generalizations on the prevalence of false negatives such as the one shown in Fig. 7-4b. It attests however to the presence of a heterogeneous optical property variation in tissues that can have noticeable effects on the EFI and the benefits gained by the FASED method which can extend the application of EFI to clinical imaging independently of the particulars of the background optical properties.

To ensure accurate and reliable EFI performance in a clinical environment we show herein that it is important to decompose the effect of optical properties on the fluorescence images. Correspondingly, we developed FASED, a decomposition method based on multiple spectral measurements, which independently determines absorption and scattering contributions. There are potentially several methods to measure absorption and scattering including the use of time-resolved or frequency domain techniques. Instead, we considered herein spectral analysis based on the RGB properties of the color images collected by the imaging system employed in the pre-clinical and clinical studies. This

approach cannot characterize absolute optical properties, as it is the case in time or frequency domain methods, but suffices for decomposing their contributions, as required by FASED. While only three spectral bands were utilized herein, the method can benefit from the availability of multiple spectral bands. The development of a system for real time simultaneous capture of multi-spectral color and fluorescence images is currently considered and can enable information that can further improve FASED operation.

Chapter 9: Conclusion and future outlook

This Chapter presents an overview of the present work and discusses possible future improvements for the developed technologies.

First of all, we developed a novel *ex-vivo* imaging modality able to capture multispectral 3D high-resolution fluorescence bio-distribution volumes in small animals in a standardized and systematic way. We carried out novel studies that showcase the limitations of the currently used planar fluorescence imaging approach for exploratory bio-distribution studies and illustrated the advantages of our technology. In particular, non-targeted and target-specific fluorescent contrast agents were studied for their distribution patterns in healthy animals, xenograft and genetically engineered mouse models, providing an insight into the targeting characteristics of every probe and the performance and potential applications of the cryoslicing technology in preclinical and clinical research. However, continuous progress in the field of multispectral cameras, methods, and

algorithms could be integrated in the flexible imaging system. Future improvements in the approach could include the development and application of more advanced spectral unmixing algorithms (principal or independent component analysis) that would allow discriminating between multiple structures of different (reflectance or fluorescence) spectrally overlapping signatures or identifying low signals from surrounding/background fluorescence activity, i.e., tissue auto-fluorescence removal. Furthermore, real-time multispectral (Themelis, Yoo et al. 2008) or spatial scanning hyperspectral (Zavattini, Vecchi et al. 2006) systems could be used to enhance the ability to image multiple spectral bands with improved speed and resolution. Finally, serving as a modality for the validation of non-invasive methods, multispectral cryoslicing imaging can offer substantial benefits during the development and evaluation of novel tomographic techniques and/or advanced algorithms. Providing accurate fluorophore quantification and imaging under the same coordinate system as the non-invasive modality, cryoslicing can provide a straightforward and direct comparison between the real fluorescence distribution in tissues and the tomography reconstructions acting, in this case, as the 'gold standard'.

In addition, an algorithm based on the Monte Carlo simulation for photon propagation method was introduced to correct for sub-surface fluorescence contributions in surface imaging of block face samples. Our algorithm successfully suppressed the out-of-plane signals, increased the optical resolution of the setup and revealed the true fluorescence intensity on the imaged surface. However there is still space for improvements. Most notably, the Monte Carlo simulation method could be combined with the FASED algorithm and use multiple reflectance measurements that would provide a more accurate calculation of the tissue optical properties (μ_a and μ_s). This could be implemented by using the already captured red, green, blue and intrinsic information and provide, thus, four reflectance measurements for the estimation of μ_a and μ_s rather than one. Another idea could be to simulate the volume between the two captured block face images as a multi-layered tissue rather than a single-layer one (for instance linearly changing). In addition, the effect of sub-surface signals could be studied in thinner

sectioning and denser imaging procedures, as the typical distance between two imaging planes was almost for all the cases presented set at 125 μ m. A thinner sectioning procedure could help further visualize the correcting properties of the algorithm.

Next, we radically improved an existing real-time multispectral imaging setup and developed a new clinical-grade fluorescence imaging modality for intra-operative use. Novel studies were carried out, including the first ever in-human imaging study of a targeted fluorophore in ovarian cancer patients. Our modality introduced and showcased the advantages of clinical imaging with extrinsically administered fluorescent agents and pushed the clinical paradigm of quantitative intra-operative fluorescence imaging in combination with novel tumor-specific bio-markers. However, we only provided preliminary results in proof-of-principle clinical trials that could not have a statistical importance and, therefore, we could not accurately measure the effect that intra-operative fluorescence imaging could actually have in what matters ultimately the most in medical research; quality of life and overall survival. For this reason, larger (in number of patients) and longer (in terms of duration) studies are needed in order to identify the real and long-term impact of this novel technology in clinical practice. Furthermore, future developments should and definitely will also provide more application specific imaging systems that will facilitate imaging in anatomically challenging areas. We identified, for example, the need for more flexible positioning systems for intra-operative imaging of the abdominal cavity since short midline incisions could hamper image-guided surgery. Generally, the second generation systems should have a smaller weight and be more adjustable/adaptable in order to facilitate their integration into the surgical environment. Even more important though is the development of novel endoscopic and laparoscopic modalities for image-guided surgical procedures. In these cases, the additional diagnostic information of fluorescence imaging will be beneficial for a larger pool of patients and the feedback will be even more effective in enhancing the surgeon's vision, since, due to the shortage of tactile information for tissue elasticity or density, all the available diagnostic information is limited in the perceived visual contrast. Finally, as novel and more advanced disease-specific

contrast agents will become increasingly available, the variety of applications for intra-operative fluorescence imaging will dramatically expand and more application-oriented devices will emerge.

Besides, we realized the most major shortcomings that obscure accurate quantification in planar fluorescence imaging and successfully developed a novel image processing technique (FASSED) to account for them. A principal components analysis based approach to decompose the effects of tissue absorption and scattering in the captured fluorescence intensity images was introduced and successfully implemented in pre-clinical and clinical examples. In fact, this was one of the very few times that the significant effect of tissue optical properties on fluorescence intensity was so thoroughly studied. Phantom experiments, animal imaging and human clinical data *in-vivo* and *ex-vivo* were used in order to showcase this elusive problem. It was important to demonstrate and prove with specific examples that the underlying tissue optical properties can indeed lead to false positives and negatives, as such shortcomings could potentially threaten the regulatory approvals of the intra-operative fluorescence imaging technology. Future developments of the algorithm could include the preparation and population of a more detailed database with decades of images of blood phantoms that could be used to calibrate the algorithm for a wider range of absorption and scattering combinations. Furthermore, additional comparisons with 'gold standard' 18 μ m-thin slices could also identify potential problems and further refine the method for animal and clinical imaging studies. New, real-time multispectral imaging systems that can capture multiple reflectance images could further enhance the FASSED approach as the method could capitalize on more refined and narrow band spectral measurements. The additional reflectance images could help decompose not only absorption and scattering but also melanin, other intrinsic chromophores or disease-specific discolorations and, thus, boost the correction performance of the algorithm. Overall, the developed correction method and the results presented in this work allow us to believe that quantitative fluorescence imaging will become increasingly popular as a modality for image-guided surgery in the near future, as it can dramatically enhance the

surgeon's vision and provide helpful diagnostic information that can facilitate the surgical procedure and the improve the overall surgery efficiency.

References

- Adusumilli, P. S., B. M. Stiles, et al. (2006). "Real-time diagnostic imaging of tumors and metastases by use of a replication-competent herpes vector to facilitate minimally invasive oncological surgery." The FASEB Journal.
- Agarwal, B., A. M. Correa, et al. (2008). "Survival in pancreatic carcinoma based on tumor size." Pancreas **36**: 15-20.
- Ale, A., R. B. Schulz, et al. (2010). "Imaging performance of a hybrid x-ray computed tomography-fluorescence molecular tomography system using priors." Med Phys **37**(5): 1976-1986.
- Aletti, G. D., M. M. Gallenberg, et al. (2007). "Current Management Strategies for Ovarian Cancer." Mayo Clinic Proceedings **82**(6): 751-770.
- Alexandrakis, G., F. R. Rannou, et al. (2005). "Tomographic bioluminescence imaging by use of a combined optical-PET (OPET) system: a computer simulation feasibility study." Physics in Medicine and Biology **50**(17): 4225-4241.
- Arridge, S. R. (1999). "Optical tomography in medical imaging." Inverse Problems **15**(2): R41.
- Auler, H. and G. Banzer (1942). "Untersuchungen über die Rolle der Porphyrine bei geschwulstkranken Menschen und Tieren." Journal of Cancer Research and Clinical Oncology **53**(2): 65-68.
- Ayhan, A., H. Celik, et al. (2008). "Lymphatic mapping and sentinel node biopsy in gynecological cancers: a critical review of the literature." World J Surg Oncol **6**(53).
- Bardeesy, N., A. J. Aguirre, et al. (2006). "Both p16Ink4a and the p19Arf-p53 pathway constrain progression of pancreatic adenocarcinoma in the mouse." Proceedings of the National Academy of Sciences **103**(15): 5947-5952.
- Beer, A. and M. Schwaiger (2008). "Imaging of integrin $\alpha\beta 3$ expression." Cancer and Metastasis Reviews **27**(4): 631-644.
- Beesley, V., M. Janda, et al. (2007). "Lymphedema after gynecological cancer treatment." Cancer **109**(12): 2607-2614.
- Bogaards, A. (2006). In Vivo Optical Imaging of Fluorescent Markers for Detection and Guided Resection of Cancer. **PhD thesis**.

- Bogaards, A., H. J. C. M. Sterenborg, et al. (2007). "In vivo quantification of fluorescent molecular markers in real-time by ratio imaging for diagnostic screening and image-guided surgery." Lasers in Surgery and Medicine **39**(7): 605-613.
- Bradley, R. S. and M. S. Thorniley (2006). "A review of attenuation correction techniques for tissue fluorescence." Journal of The Royal Society Interface **3**(6): 1-13.
- Bugaj, J. E., S. Achilefu, et al. (2001). "Novel fluorescent contrast agents for optical imaging of in vivo tumors based on a receptor-targeted dye-peptide conjugate platform." J Biomed Opt **6**: 122-133.
- Cannestra, A. F., E. M. Santori, et al. (1997). "A three-dimensional multimodality brain map of the nemestrina monkey." Brain Res Bull. **43**(2): 141-148.
- Cartwright, T., D. A. Richards, et al. (2008). "Cancer of the pancreas: are we making progress? A review of studies in the US Oncology Research Network." Cancer Control **15**(4): 308-313.
- Carver, B. S. and P. P. Pandolfi (2006). "Mouse modeling in oncologic preclinical and translational research." Clin Cancer Res **12**(18): 5305-5311.
- Céspedes, M., I. Casanova, et al. (2006). "Mouse models in oncogenesis and cancer therapy." Clinical and Translational Oncology **8**(5): 318-329.
- Chen, N., Q. Zhang, et al. (2009). "A novel recombinant vaccinia virus expressing the human norepinephrine transporter retains oncolytic potential and facilitates deep-tissue imaging." Mol Med **15**(5-6): 144-151.
- Cheong, W. F., S. A. Pahl, et al. (1990). "A review of the optical properties of biological tissues." IEEE J Quantum Elect **26**(12): 2166 - 2185.
- Condeelis, J. and R. Weissleder (2010). "In Vivo Imaging in Cancer." Cold Spring Harbor Perspectives in Biology **2**(12).
- Crane, L., G. Themelis, et al. (2010). "Intraoperative Multispectral Fluorescence Imaging for the Detection of the Sentinel Lymph Node in Cervical Cancer: A Novel Concept." Molecular Imaging and Biology: 1-7.
- Crane, L. M., G. Themelis, et al. (2010). "Multispectral real-time fluorescence imaging for intraoperative detection of the sentinel lymph node in gynecologic oncology." J Vis Exp **44**.
- Crane, L. M. A. (2010). Intra-operative fluorescence imaging in cancer. **PhD thesis**.

- Crane, L. M. A., G. Themelis, et al. (2011). "Intraoperative near-infrared fluorescence imaging for sentinel lymph node detection in vulvar cancer: First clinical results." Gynecologic Oncology **120**(2): 291-295.
- Darlin, L., J. Persson, et al. (2010). "The sentinel node concept in early cervical cancer performs well in tumors smaller than 2 cm." Gynecologic Oncology **117**(2): 266-269.
- Deguchi, J.-o., M. Aikawa, et al. (2006). "Inflammation in Atherosclerosis." Circulation **114**(1): 55-62.
- Desgrosellier, J. S. and D. A. Cheresh (2010). "Integrins in cancer: biological implications and therapeutic opportunities." Nat Rev Cancer **10**(1): 9-22.
- Dogdas, B., D. Stout, et al. (2007). "Digimouse: a 3D whole body mouse atlas from CT and cryosection data." Physics in Medicine and Biology **52**(3): 577.
- Eisenberg, D. P., P. S. Adusumilli, et al. (2006). "Real-Time Intraoperative Detection of Breast Cancer Axillary Lymph Node Metastases Using a Green Fluorescent Protein-Expressing Herpes Virus." Annals of Surgery **243**(6): 824-832.
- El-Ghobashy, A. E. and S. A. Saidi (2009). "Sentinel lymph node sampling in gynaecological cancers: Techniques and clinical applications." European Journal of Surgical Oncology (EJSO) **35**(7): 675-685.
- Eser, S., M. Messer, et al. (2011). "In vivo diagnosis of murine pancreatic intraepithelial neoplasia and early-stage pancreatic cancer by molecular imaging." Proceedings of the National Academy of Sciences **108**(24): 9945-9950.
- Ewald, A. J., H. McBride, et al. (2002). "Surface imaging microscopy, an automated method for visualizing whole embryo samples in three dimensions at high resolution." Developmental Dynamics **225**(3): 369-375.
- Frumovitz, M., P. T. Ramirez, et al. (2008). "Lymphatic mapping and sentinel lymph node detection in women with cervical cancer." Gynecologic Oncology **110**(3, Supplement 2): S17-S20.
- Füller, J., D. Guderian, et al. (2008). "Lymph Edema of the Lower Extremities after Lymphadenectomy and Radiotherapy for Cervical Cancer." Strahlentherapie und Onkologie **184**(4): 206-211.
- Gao, X., Y. Cui, et al. (2004). "In vivo cancer targeting and imaging with semiconductor quantum dots." Nat Biotech **22**(8): 969-976.

- Gondos, A., F. Bray, et al. (2009). "Trends in cancer survival in 11 European populations from 1990 to 2009: a model-based analysis." Annals of Oncology **20**(3): 564-573.
- Hausner, S. H., C. K. Abbey, et al. (2009). "Targeted In vivo Imaging of Integrin $\alpha\beta 6$ with an Improved Radiotracer and Its Relevance in a Pancreatic Tumor Model." Cancer Research **69**(14): 5843-5850.
- Hillman, E. M. C. and S. A. Burgess (2009). "Sub-millimeter resolution 3D optical imaging of living tissue using laminar optical tomography." Laser & Photonics Reviews **3**(1-2): 159-179.
- Hillman, E. M. C. and A. Moore (2007). "All-optical anatomical co-registration for molecular imaging of small animals using dynamic contrast." Nat Photon **1**(9): 526-530.
- Hingorani, S. R., E. F. Petricoin, et al. (2003). "Preinvasive and invasive ductal pancreatic cancer and its early detection in the mouse." Cancer cell **4**(6): 437-450.
- Hingorani, S. R., L. Wang, et al. (2005). "Trp53R172H and KrasG12D cooperate to promote chromosomal instability and widely metastatic pancreatic ductal adenocarcinoma in mice." Cancer cell **7**(5): 469-483.
- Hood, J. D. and D. A. Cheresh (2002). "Role of integrins in cell invasion and migration." Nat Rev Cancer **2**(2): 91-100.
- Horn, L.-C., B. Hentschel, et al. (2008). "Detection of micrometastases in pelvic lymph nodes in patients with carcinoma of the cervix uteri using step sectioning: Frequency, topographic distribution and prognostic impact." Gynecologic Oncology **111**(2): 276-281.
- Hosotani, R., M. Kawaguchi, et al. (2002). "Expression of Integrin $[\alpha]V[\beta]3$ in Pancreatic Carcinoma: Relation to MMP-2 Activation and Lymph Node Metastasis." Pancreas **25**(2): e30-e35.
- <http://www.invitrogen.com/site/us/en/home/support/Research-Tools/Fluorescence-SpectraViewer.html?fileId1=EGFPpH7>.
- <http://www.licor.com/bio/news/09.08.10.jsp>.
- Ibeanu, O. A. and R. E. Bristow (2010). "Predicting the Outcome of Cytoreductive Surgery for Advanced Ovarian Cancer: A Review." International Journal of Gynecological Cancer **20**(10): S1-S11
- Jaffer, F. A., P. Libby, et al. (2007). "Molecular Imaging of Cardiovascular Disease." Circulation **116**(9): 1052-1061.

Jaffer, F. A. and R. Weissleder (2005). "Molecular Imaging in the Clinical Arena." JAMA: The Journal of the American Medical Association **293**(7): 855-862.

Jemal, A., R. Siegel, et al. (2008). "Cancer Statistics, 2008." CA: A Cancer Journal for Clinicians **58**(2): 71-96.

Kalli, K. R., A. L. Oberg, et al. (2008). "Folate receptor alpha as a tumor target in epithelial ovarian cancer." Gynecologic Oncology **108**(3): 619-626.

Kaushal, S., M. McElroy, et al. (2008). "Fluorophore-conjugated anti-CEA Antibody for the Intraoperative Imaging of Pancreatic and Colorectal Cancer." Journal of Gastrointestinal Surgery **12**(11): 1938-1950.

Kelland, L. R. (2004). "'Of mice and men': values and liabilities of the athymic nude mouse model in anticancer drug development." European journal of cancer (Oxford, England : 1990) **40**(6): 827-836.

Kennedy, M. D., K. N. Jallad, et al. (2003). "Optical imaging of metastatic tumors using a folate-targeted fluorescent probe." J Biomed Opt **8**(4): 636-641.

Kircher, M. F., U. Mahmood, et al. (2003). "A Multimodal Nanoparticle for Preoperative Magnetic Resonance Imaging and Intraoperative Optical Brain Tumor Delineation." Cancer Research **63**(23): 8122-8125.

Knyazikhin, Y. and R. B. Myneni (2004) The Radiation Field and the Radiative Transfer Equation. <http://cliveg.bu.edu/courses/gg645fall04/chap01/chap01.pdf>

Kossodo, S., M. Pickarski, et al. (2010). "Dual In Vivo Quantification of Integrin-targeted and Protease-activated Agents in Cancer Using Fluorescence Molecular Tomography (FMT)." Molecular Imaging and Biology **12**(5): 488-499.

Kremer, P., A. Wunder, et al. (2000). "Laser-induced fluorescence detection of malignant gliomas using fluorescein-labeled serum albumin: experimental and preliminary clinical results." Neurol Res **22**(5): 481-489.

Kuil, J., A. H. Velders, et al. (2010). "Multimodal Tumor-Targeting Peptides Functionalized with Both a Radio- and a Fluorescent Label." Bioconjugate Chemistry **21**(10): 1709-1719.

Leamon, C. P., M. A. Parker, et al. (2002). "Synthesis and Biological Evaluation of EC20: A New Folate-Derived, 99mTc-Based Radiopharmaceutical." Bioconjugate Chemistry **13**(6): 1200-1210.

null

- Levenson, R. M. and J. R. Mansfield (2006). "Multispectral imaging in biology and medicine: Slices of life." Cytometry Part A **69A**(8): 748-758.
- Li, M. L., J. T. Oh, et al. (2008). "Simultaneous molecular and hypoxia imaging of brain tumors in vivo using spectroscopic photoacoustic tomography." Proc IEEE **96**(3): 481-489.
- Lin, J. L., J. S. Barthel, et al. (2011). "Negative Predictive Value of Positron Emission Tomography/Computed Tomography in Patients With a Clinical Suspicion of Pancreatic Cancer." Pancreas.
- Markert, S., S. Lassmann, et al. (2008). "Alpha-folate Receptor Expression in Epithelial Ovarian Carcinoma and Non-neoplastic Ovarian Tissue." Anticancer Research **28**(6A): 3567-3572.
- Mathias, C. J., S. Wang, et al. (1998). "Indium-111-DTPA-Folate as a Potential Folate Receptor-Targeted Radiopharmaceutical." Journal of Nuclear Medicine **39**(9): 1579-1585.
- Matsuura, Y., T. Kawagoe, et al. (2006). "Long-standing complications after treatment for cancer of the uterine cervix—clinical significance of medical examination at 5 years after treatment." International Journal of Gynecological Cancer **16**(1): 294-297.
- McElroy, M., S. Kaushal, et al. (2008). "Imaging of Primary and Metastatic Pancreatic Cancer Using a Fluorophore-Conjugated Anti-CA19-9 Antibody for Surgical Navigation." World Journal of Surgery **32**(6): 1057-1066.
- McMahon, C. J., N. M. Rofsky, et al. (2010). "Lymphatic Metastases from Pelvic Tumors: Anatomic Classification, Characterization, and Staging1." Radiology **254**(1): 31-46.
- Mieog, J. S., A. L. Vahrmeijer, et al. (2010). "Novel intraoperative near-infrared fluorescence camera system for optical image-guided cancer surgery." Mol Imaging **9**(4): 223-231.
- Montet, X., J.-L. Figueiredo, et al. (2007). "Tomographic Fluorescence Imaging of Tumor Vascular Volume in Mice1." Radiology **242**(3): 751-758.
- Moore, G. E. (1947). "Fluorescein as an Agent in the Differentiation of Normal and Malignant Tissues." Science **106**(2745): 130-131.
- Neves, A. and K. Brindle (2006). "Assesing responses to cancer therapy using molecular imaging."
- Nguyen, Q. T., E. S. Olson, et al. (2010). "Surgery with molecular fluorescence imaging using activatable cell-penetrating peptides decreases residual cancer and improves survival." Proceedings of the National Academy of Sciences **107**(9): 4317-4322.

- Ntziachristos, V., J. Ripoll, et al. (2005). "Looking and listening to light: the evolution of whole-body photonic imaging." Nat Biotech **23**(3): 313-320.
- Ntziachristos, V., C.-H. Tung, et al. (2002). "Fluorescence molecular tomography resolves protease activity in vivo." Nat Med **8**(7): 757-761.
- Ntziachristos, V., G. Turner, et al. (2005). "Planar fluorescence imaging using normalized data." J Biomed Opt **10**(6): 064007.
- Ogawa, S., H. Kobayashi, et al. (2010). "Sentinel node detection with (99m)Tc phytate alone is satisfactory for cervical cancer patients undergoing radical hysterectomy and pelvic lymphadenectomy." International Journal of Clinical Oncology **15**(1): 52-58.
- Olive, K. P., M. A. Jacobetz, et al. (2009). "Inhibition of Hedgehog Signaling Enhances Delivery of Chemotherapy in a Mouse Model of Pancreatic Cancer." Science **324**(5933): 1457-1461.
- Olson, E. S., T. Jiang, et al. (2010). "Activatable cell penetrating peptides linked to nanoparticles as dual probes for in vivo fluorescence and MR imaging of proteases." Proceedings of the National Academy of Sciences **107**(9): 4311-4316.
- Partecke, I., A. Kaeding, et al. (2011). "In vivo imaging of pancreatic tumours and liver metastases using 7 Tesla MRI in a murine orthotopic pancreatic cancer model and a liver metastases model." BMC Cancer **11**(1): 40.
- Pic, E., T. Pons, et al. (2010). "Fluorescence Imaging and Whole-Body Biodistribution of Near-Infrared-Emitting Quantum Dots after Subcutaneous Injection for Regional Lymph Node Mapping in Mice." Molecular Imaging and Biology **12**(4): 394-405.
- Pleijhuis, R. G., G. C. Langhout, et al. (2011). "Near-infrared fluorescence (NIRF) imaging in breast-conserving surgery: assessing intraoperative techniques in tissue-simulating breast phantoms." Eur J Surg Oncol **37**(1): 32-39.
- Policard, A. (1924). "Étude sur les aspects offerts par des tumeurs expérimentales examinées à la lumière de Wood." C. R. Séances Soc. Biol. Fil **91**: 1423-1424.
- Rasty, G. (2009). "Sentinel lymph node examination for cancer of the uterine cervix." Journal of Clinical Pathology.
- Ray, E. R., K. Chatterton, et al. (2009). "Hexylaminolaevulinate 'blue light' fluorescence cystoscopy in the investigation of clinically unconfirmed positive urine cytology." BJU International **103**(10): 1363-1367.

- Razansky, D., M. Distel, et al. (2009). "Multispectral opto-acoustic tomography of deep-seated fluorescent proteins in vivo." Nat Photon **3**(7): 412-417.
- Razansky, D., C. Vinegoni, et al. (2007). "Multispectral photoacoustic imaging of fluorochromes in small animals." Opt. Lett. **32**(19): 2891-2893.
- Rosenthal, J., V. Mangal, et al. (2004). "Rapid high resolution three dimensional reconstruction of embryos with episodic fluorescence image capture." Birth Defects Research Part C: Embryo Today: Reviews **72**(3): 213-223.
- Sarantopoulos, A., G. Themelis, et al. (2010). "Imaging the Bio-Distribution of Fluorescent Probes Using Multispectral Epi-Illumination Cryoslicing Imaging." Molecular Imaging and Biology: 1-12.
- Sarder, P. and A. Nehorai (2008). "Estimating locations of quantum-dot-encoded microparticles from ultra-high density 3-D microarrays." IEEE Trans Nanobioscience **7**(4): 284-297.
- Schulz, R. B., A. Ale, et al. (2010). "Hybrid system for simultaneous fluorescence and x-ray computed tomography." IEEE Trans Med Imaging **29**(2): 465-473.
- Sega, E. and P. Low (2008). "Tumor detection using folate receptor-targeted imaging agents." Cancer and Metastasis Reviews **27**(4): 655-664.
- Sevick-Muraca, E. M., R. Sharma, et al. (2008). "Imaging of Lymph Flow in Breast Cancer Patients after Microdose Administration of a Near-Infrared Fluorophore: Feasibility Study1." Radiology **246**(3): 734-741.
- Shami, V. M., A. Mahajan, et al. (2011). "Comparison between endoscopic ultrasound and magnetic resonance imaging for the staging of pancreatic cancer." Pancreas **40**(4): 567-570.
- Sharpe, J., U. Ahlgren, et al. (2002). "Optical projection tomography as a tool for 3D microscopy and gene expression studies." Science **296**(5567): 541-545.
- Shimada, K., Y. Sakamoto, et al. (2006). "Reappraisal of the clinical significance of tumor size in patients with pancreatic ductal carcinoma." Pancreas **33**: 233–239.
- Shu, X., A. Royant, et al. (2009). "Mammalian Expression of Infrared Fluorescent Proteins Engineered from a Bacterial Phytochrome." Science **324**(5928): 804-807.
- Singh, M. and L. Johnson (2006). "Using Genetically Engineered Mouse Models of Cancer to Aid Drug Development: An Industry Perspective." Clinical Cancer Research **12**(18): 5312-5328.

- Singh, M., A. Lima, et al. (2010). "Assessing therapeutic responses in Kras mutant cancers using genetically engineered mouse models." Nat Biotech **28**(6): 585-593.
- Siveke, J. T., H. Einwächter, et al. (2007). "Concomitant Pancreatic Activation of KrasG12D and Tgfa Results in Cystic Papillary Neoplasms Reminiscent of Human IPMN." Cancer cell **12**(3): 266-279.
- Snyder, C., S. Kaushal, et al. (2009). "Complementarity of ultrasound and fluorescence imaging in an orthotopic mouse model of pancreatic cancer." BMC Cancer **9**(1): 106.
- Stangl, S., M. Gehrman, et al. (2011). "In vivo imaging of CT26 mouse tumours by using cmHsp70.1 monoclonal antibody." Journal of Cellular and Molecular Medicine **15**(4): 874-887.
- Stangl, S., M. Gehrman, et al. (2011). "Targeting membrane heat-shock protein 70 (Hsp70) on tumors by cmHsp70.1 antibody." Proceedings of the National Academy of Sciences **108**(2): 733-738.
- Steinkamp, J. A. and C. C. Stewart (1986). "Dual-laser, differential fluorescence correction method for reducing cellular background autofluorescence." Cytometry **7**(6): 566-574.
- Steyer, G. J., D. Roy, et al. (2009). "Cryo-imaging of fluorescently labeled single cells in a mouse." Proc. SPIE **7262**(1): 72620W.
- Stummer, W., C. Götz, et al. (1993). "Kinetics of Photofrin II in Perifocal Brain Edema." Neurosurgery **33**(6): 1075-1082.
- Stummer, W., A. Novotny, et al. (2000). "Fluorescence-guided resection of glioblastoma multiforme utilizing 5-ALA-induced porphyrins: a prospective study in 52 consecutive patients." Journal of Neurosurgery **93**(6): 1003-1013.
- Stummer, W., H. J. Reulen, et al. (2003). "Fluorescence-guided resections of malignant gliomas--an overview." Acta Neurochir Suppl **88**: 9-12.
- Stummer, W., S. Stocker, et al. (1998). "Intraoperative Detection of Malignant Gliomas by 5-Aminolevulinic Acid-induced Porphyrin Fluorescence." Neurosurgery **42**(3): 518-526.
- Tanaka, E., H. Choi, et al. (2006). "Image-Guided Oncologic Surgery Using Invisible Light: Completed Pre-Clinical Development for Sentinel Lymph Node Mapping." Annals of Surgical Oncology **13**(12): 1671-1681.
- Tanis, P., O. Nieweg, et al. (2001). "History of sentinel node and validation of the technique." Breast Cancer Res **3**(2): 109 - 112.

- Taruttis, A., E. Herzog, et al. (2010). "Real-time imaging of cardiovascular dynamics and circulating gold nanorods with multispectral optoacoustic tomography." Opt. Express **18**(19): 19592-19602.
- Tempero, M., W. Plunkett, et al. (2003). "Randomized phase II comparison of dose-intense gemcitabine: thirty-minute infusion and fixed dose rate infusion in patients with pancreatic adenocarcinoma." **21**(18).
- Themelis, G., N. Harlaar, et al. (2011). "Enhancing Surgical Vision by Using Real-Time Imaging of $\alpha\beta 3$ -Integrin Targeted Near-Infrared Fluorescent Agent." Annals of Surgical Oncology: 1-8.
- Themelis, G., J. S. Yoo, et al. (2008). "Multispectral imaging using multiple-bandpass filters." Opt. Lett. **33**(9): 1023-1025.
- Themelis, G., J. S. Yoo, et al. (2009). "Real-time intraoperative fluorescence imaging system using light-absorption correction." J Biomed Optics **14**(6): 064012.
- Tinga, D. J., J. Bouma, et al. (1992). "Patients with squamous cell versus adeno(squamous) carcinoma of the cervix, what factors determine the prognosis?" International Journal of Gynecological Cancer **2**(2): 83-91.
- Troyan, S., V. Kianzad, et al. (2009). "The FLARE Intraoperative Near-Infrared Fluorescence Imaging System: A First-in-Human Clinical Trial in Breast Cancer Sentinel Lymph Node Mapping." Annals of Surgical Oncology **16**(10): 2943-2952.
- van Dam, G. M., G. Themelis, et al. (2011). "Intraoperative Tumor-Specific Fluorescent Imaging in Ovarian Cancer by Folate Receptor- α Targeting: First In-Human Results. ." Nat Med [accepted].
- van de Lande, J., B. Torrenge, et al. (2007). "Sentinel lymph node detection in early stage uterine cervix carcinoma: A systematic review." Gynecologic Oncology **106**(3): 604-613.
- Vergote, I., T. Van Gorp, et al. (2008). "Timing of debulking surgery in advanced ovarian cancer." International Journal of Gynecological Cancer **18**: 11-19.
- Vinegoni, C., D. Razansky, et al. (2009). "Transillumination fluorescence imaging in mice using biocompatible upconverting nanoparticles." Opt. Lett. **34**(17): 2566-2568.
- Wagner, M., F. R. Greten, et al. (2001). "A murine tumor progression model for pancreatic cancer recapitulating the genetic alterations of the human disease." Genes & Development **15**(3): 286-293.

- Wang, L., S. L. Jacques, et al. (1995). "MCML--Monte Carlo modeling of light transport in multi-layered tissues." Computer Methods and Programs in Biomedicine **47**(2): 131-146.
- Weissleder, R. and V. Ntziachristos (2003). "Shedding light onto live molecular targets." Nat Med **9**(1): 123-128.
- Weissleder, R. and M. J. Pittet (2008). "Imaging in the era of molecular oncology." Nature **452**(7187): 580-589.
- Weissleder, R., C.-H. Tung, et al. (1999). "In vivo imaging of tumors with protease-activated near-infrared fluorescent probes." Nat Biotech **17**(4): 375-378.
- Welch, S. A. and M. J. Moore (2007). "Combination chemotherapy in advanced pancreatic cancer: time to raise the white flag?" J Clin Oncol **25**(16): 2159-2161.
- Weninger, W. J. and T. Mohun (2002). "Phenotyping transgenic embryos: a rapid 3-D screening method based on episcopic fluorescence image capturing." Nat Genet **30**(1): 59-65.
- Wilson, D., D. Roy, et al. (2008). "Whole mouse cryo-imaging." Proc. SPIE **6916**(1): 691611.
- Winter, W. E., G. L. Maxwell, et al. (2008). "Tumor Residual After Surgical Cytoreduction in Prediction of Clinical Outcome in Stage IV Epithelial Ovarian Cancer: A Gynecologic Oncology Group Study." Journal of Clinical Oncology **26**(1): 83-89.
- Yamashita, T., H. Katayama, et al. (2009). "Management of Pelvic Lymph Nodes by Sentinel Node Navigation Surgery in the Treatment of Invasive Cervical Cancer." International Journal of Gynecological Cancer **19**(6): 1113-1118.
- Yang, M., E. Baranov, et al. (2000). "Whole-body optical imaging of green fluorescent protein-expressing tumors and metastases." Proceedings of the National Academy of Sciences **97**(3): 1206-1211.
- Zavattini, G., S. Vecchi, et al. (2006). "A hyperspectral fluorescence system for 3D in vivo optical imaging." Physics in Medicine and Biology **51**(8): 2029-2043.
- Zimmermann, T., J. Rietdorf, et al. (2003). "Spectral imaging and its applications in live cell microscopy." FEBS letters **546**(1): 87-92.
- Zivanovic, O., F. Khoury-Collado, et al. (2009). "Sentinel Lymph Node Biopsy in the Management of Vulvar Carcinoma, Cervical Cancer, and Endometrial Cancer." The Oncologist **14**(7): 695-705.

Zong, H., J. S. Espinosa, et al. (2005). "Mosaic Analysis with Double Markers in Mice." Cell **121**(3): 479-492.

List of publications

- 1. Sarantopoulos, A., G. Themelis, V. Ntziachristos.** (2010) Imaging the Bio-Distribution of Fluorescent Probes Using Multispectral Epillumination Cryoslicing Imaging. *Mol Imaging Biol*: 1-12, doi: 10.1007/s11307-010-0416-8.
- 2. Sarantopoulos, A., N. Beziere, V. Ntziachristos.** (2012) Optical and optoacoustic interventional imaging. *Ann Biomed Eng.* 40(2):346-66.
- 3. Sarantopoulos, A., M. Trajkovic-Arsic, G. Themelis, E. Kalideris, A. Beer, R. Braren, R. M. Schmid, V. Ntziachristos, J. T. Sivecke.** Molecular imaging of integrin $\alpha V\beta 3$ for in vivo detection of precursor lesions and pancreatic cancer, submitted.
- 4. van Dam, G. M., G. Themelis, L. M. A. Crane, N. J. Harlaar, R. G. Pleijhuis, W. Kelder, A. Sarantopoulos, J. S. de Jong, H. J. G. Arts, A. G. J. van der Zee, J. Bart, P. S. Low, V. Ntziachristos.** (2011) Intraoperative tumor-specific fluorescence imaging in ovarian cancer by folate receptor- α targeting: first in-human results. *Nat Med*, doi:10.1038/nm.2472.
- 5. Crane, L. M. A., G. Themelis, R. G. Pleijhuis, N. J. Harlaar, A. Sarantopoulos, H. J. G. Arts, A. G. J. van der Zee, V. Ntziachristos, G. M. van Dam.** (2010) Intraoperative Multispectral Fluorescence Imaging for the Detection of the Sentinel Lymph Node in Cervical Cancer: A Novel Concept. *Mol Imaging Biol*: 1-7, doi:10.1007/s11307-010-0425-7.
- 6. Crane, L.M., G. Themelis, T. Buddingh, N. J. Harlaar, R. G. Pleijhuis, A. Sarantopoulos, A. G. van der Zee, V. Ntziachristos, G. M. van Dam.** (2010) Multispectral real-time fluorescence imaging for intraoperative detection of the sentinel lymph node in gynecologic oncology. *J Vis Exp*, Oct 20;(44), doi: 10.3791/2225.
- 7. Pleijhuis, R. G., G. C. Langhout, W. Helfrich, G. Themelis, A. Sarantopoulos, L. M. Crane, N. J. Harlaar, J. S. de Jong, V. Ntziachristos, G. M. van Dam.** (2011) Nearinfrared fluorescence (NIRF) imaging in breast-conserving surgery: Assessing intraoperative techniques in tissue-simulating breast phantoms. *Eur J Surg Oncol*, 37(1):32-9.
- 8. Themelis, G., N. J. Harlaar, W. Kelder, J. Bart, A. Sarantopoulos, G. M. van Dam, V. Ntziachristos.** (2011) Enhancing Surgical Vision by Using Real Time Imaging of $\alpha(v)\beta(3)$ -Integrin Targeted Near-Infrared Fluorescent Agent. *Ann Surg Oncol*, doi: 10.1245/s10434-011-1664-9.

- 9. Stangl, S., G. Themelis, L. Friedrich, V. Ntziachristos, A. Sarantopoulos, M. Molls, A. Skerra, G. Multhoff.** (2011) Detection of irradiation-induced, membrane heat shock protein 70 (Hsp70) in mouse tumors using Hsp70 Fab fragment. *Radiother Oncol*, 99(3):313-6.
- 10. Ale, A., R. B. Schulz, A. Sarantopoulos, V. Ntziachristos.** (2010) Imaging performance of a hybrid x-ray computed tomography-fluorescence molecular tomography system using priors, *Med Phys*, 37(5):1976-86.
- 11. Schulz, R. B., A. Ale, A. Sarantopoulos, M. Freyer, E. Soehngen, M. Zientkowska, V. Ntziachristos.** (2010) Hybrid System for Simultaneous Fluorescence and-x-ray Computed Tomography. *IEEE Trans Med Imaging*, 29(2):365-73.